UAB
Universitat Autònoma de Barcelona

Wearable Platform for Real-Time Monitoring of Biomarkers in Sweat

Meritxell Rovira Fernández

Universitat Autònoma de Barcelona

Wearable Platform for Real-Time Monitoring of Biomarkers in Sweat

Meritxell Rovira Fernández

DOCTORAL THESIS

Ph. D. in Chemistry

Supervisors

Dr. Cecilia Jiménez Jorquera

Dr. César Fernández Sánchez

Institut de Microelectrònica de Barcelona (IMB-CNM)-CSIC

Departament de Química – Facultat de Ciències

2023

Dr. Cecilia Jiménez Jorquera and Dr. César Fernández Sánchez research scientists at the Institute of Microelectronics of Barcelona (IMB-CNM, CSIC),

DECLARE

That this PhD thesis in chemistry entitled:

Wearable Platform for Real-Time Monitoring of Biomarkers in Sweat

has been performed by Meritxell Rovira Fernández in the Chemical Transducers Group laboratory (GTQ) at the Institute of Microelectronics of Barcelona under our supervision.

Dr. Cecilia Jiménez Jorquera *Dr. César Fernández-Sánchez*

Institute of Microelectronics of Barcelona (IMB-CNM, CSIC)
C/ dels Til·lers. Campus Universitat Autònoma de Barcelona (UAB)
08193 Cerdanyola del Vallès (Bellaterra)
Barcelona, Spain

This work has been developed under the mentoring of Dr. Maria del Mar Puyol Bosch, Associated Professor at the Analytical Chemistry Department at the Autonomous University of Barcelona.

LIST OF ACRONYMS AND ABBREVIATIONS

α	Significance level
a	Ion activity
BSA	Bovine serum albumin
CE	Counter electrode
CI	Confidence interval
CMOS	Complementary metal-oxide semiconductor
CV	Cyclic voltammetry
DI	Deionized (water)
DMPA	2,2'-dimethoxy-2-phenyl acetophenone
DOS	Bis(2-ethylhexyl)sebacate
EDTA	Ethylenediaminetetraacetic acid
EIS	Electrochemical impedance spectroscopy,
EG	Ethylene glycol
EGDMA	Ethylene glycol dimethacrylate
FcMeOH	Ferrocene methanol
FIM	Fixed interference method
G_M	Transconductance
HDDA	1,6-hexanediol diacrylate
HEMA	2-hydroxyethyl methacrylate
HPLC	High Performance Liquid Chromatography
IC	Ion chromatography
I_{DS}	Current between drain and source
I_{off}	Leakage current
ISE	Ion-selective electrode

ISFET	Ion-sensitive field-effect transistor
K_{ij}^{pot}	Potentiometric selectivity coefficient
KTpClPB	Potassium tetrakis(4-chlorophenyl)borate
LOD	Limit of detection
MOSFET	Metal-oxide-semiconductor field-effect transistor
OCP	Open-circuit potential
PBS	Phosphate buffered saline
PCB	Printed circuit board
PDMS	Polydimethylsiloxane
PE	Polyethylene
PMMA	Poly(methyl methacrylate)
PI	Polyimide
PP	Polypropylene
PSA	Pressure-sensitive adhesive
PVB	Polyvinyl butyral
R^2	Coefficient of determination
RE	Reference electrode
REFET	Reference field-effect transistor
RMSE	Root-mean-square error
SAP	Superabsorbent sodium polyacrylate
SD	Standard deviation
SOI	Silicon on insulator
t_{calc} / t_{crit}	T-statistic value and the correspondent critical value
TDMACl	Tridodecylmethylammonium chloride
TE	Tris-EDTA
TESUD	11-(triethoxysilyl)undecanal
THF	Tetrahydrofuran
TRIS	Tris(hydroxymethyl)aminomethane
UV	Ultraviolet
V_{DS}	Potential between drain and source
V_{GS}	Potential between gate and source

V_{TH}	Threshold voltage
WE	Working electrode
w/	With
w/o	Without
ZIF	Zero insertion force

RESUM

El camp de la medicina esportiva exigeix tecnologies avançades per a monitorar paràmetres fisiològics i prevenir lesions, deshidratació, enrampades i hiponatrèmia entre els atletes. Recentment s'ha prestat especial atenció a la detecció de biomarcadores mitjançant mètodes analítics no invasius, sent la suor un fluid biològic molt adequat per la seva fàcil accessibilitat i el seu ric contingut en biomarcadores. L'ús de plataformes analítiques portàtils que integren sensors electroquímics i components fluídics basats en capil·laritat permet el monitoratge continu i en temps real de la composició de la suor, amb diversos electròlits com Na^+, Cl^- i K^+, metabòlits com a glucosa i lactat, i hormones com el cortisol com a objectiu principal. S'ha demostrat que el contingut de la suor està relacionat amb la deshidratació, l'estrès, la intensitat de l'exercici i la fatiga.

No obstant això, en el desenvolupament de dispositius portàtils persisteixen problemes com la les adsorcions no específiques i problemes de brutícia a causa de la mostra, la sensibilitat, la flexibilitat, l'estabilitat i la recollida de mostra. Factors com l'evaporació de la suor, la contaminació de la pell i la variabilitat en la composició compliquen encara més la precisió de les anàlisis.

En aquest context, aquesta tesi se centra en el desenvolupament d'una plataforma portàtil flexible per al monitoratge continu de diversos biomarcadores de la suor. Inclou el desenvolupament i la caracterització exhaustiva de sensors potenciomètricos basats en transistors d'efecte de camp sensibles a ions (ISFET) per a la mesura de pH, Na^+, K^+ i Cl^-. A més, es produeix un elèctrode de referència d'estat sòlid, clau per a la integració d'aquests

sensors en la plataforma portàtil, en un xip que conté un elèctrode de platí de pel·lícula prima. S'avalua la integració del sensor i l'elèctrode de referència juntament amb un sensor de temperatura i components fluídics en una petita plataforma flexible. S'exploren diferents arquitectures fluídiques per a permetre el monitoratge de mostres en temps real i a baixa velocitat de flux, avaluant diferents materials i dissenys geomètrics en condicions que s'assemblen a l'ús pràctic.

Finalment, el prototip de sensor portàtil s'avalua en estudis clínics realitzats amb subjectes que realitzen sessions de ciclisme d'alta intensitat en un entorn controlat de l'Hospital Universitari de Lausana. El rendiment els sensors basats en ISFET en el cos es compara amb el d'elèctrodes selectius d'ions (ISE) comercials utilitzant mostres discretes recollides periòdicament durant les sessions de ciclisme. S'eluciden algunes tendències que poden correlacionar-se amb les condicions de l'atleta i que evidencien l'aplicació pràctica de la plataforma presentada per al monitoratge de biomarcadors en el cos.

RESUMEN

El campo de la medicina deportiva exige tecnologías avanzadas para monitorizar parámetros fisiológicos y prevenir lesiones, deshidratación, calambres e hiponatremia entre los atletas. Recientemente se ha prestado especial atención a la detección de biomarcadores mediante métodos analíticos no invasivos, siendo el sudor un fluido biológico muy adecuado por su fácil accesibilidad y su rico contenido en biomarcadores. El uso de plataformas analíticas portátiles que integran sensores electroquímicos y componentes fluídicos basados en capilaridad permite la monitorización continua y en tiempo real de la composición del sudor, con varios electrolitos como Na^+, Cl^- y K^+, metabolitos como glucosa y lactato, y hormonas como el cortisol como objetivo principal. Se ha demostrado que el contenido del sudor está relacionado con la deshidratación, el estrés, la intensidad del ejercicio y la fatiga.

Sin embargo, en el desarrollo de dispositivos portátiles persisten problemas como las adsorciones no específicas y problemas de ensuciamiento debido a la muestra, la sensibilidad, la flexibilidad, la estabilidad y la recogida de muestra. Factores como la evaporación del sudor, la contaminación de la piel y la variabilidad en la composición complican aún más la precisión de los análisis.

En este contexto, esta tesis se centra en el desarrollo de una plataforma portátil flexible para la monitorización continua de varios biomarcadores del sudor. Incluye el desarrollo y la caracterización exhaustiva de sensores potenciométricos basados en transistores de efecto de campo sensibles a iones (ISFET) para la medida de pH, Na^+, K^+ y Cl^-. Además, se produce un electrodo de referencia de estado sólido, clave para la integración de estos sensores en la

plataforma portátil, en un chip que contiene un electrodo de platino de película delgada. Se evalúa la integración del sensor y el electrodo de referencia junto con un sensor de temperatura y componentes fluídicos en una pequeña plataforma flexible. Se exploran diferentes arquitecturas fluídicas para permitir la monitorización de muestras en tiempo real y a baja velocidad de flujo, evaluando diferentes materiales y diseños geométricos en condiciones que se asemejan al uso práctico.

Por último, el prototipo de sensor portátil se evalúa en estudios clínicos realizados con sujetos que realizan sesiones de ciclismo de alta intensidad en un entorno controlado del Hospital Universitario de Lausana. El rendimiento los sensores basados en ISFET en el cuerpo se compara con el de electrodos selectivos de iones (ISE) comerciales utilizando muestras discretas recogidas periódicamente durante las sesiones de ciclismo. Se elucidan algunas tendencias que pueden correlacionarse con las condiciones del atleta y que evidencian la aplicación práctica de la plataforma presentada para la monitorización de biomarcadores en el cuerpo.

SUMMARY

The field of sports medicine demands advanced technologies to monitor physiological parameters, prevent injuries, dehydration, cramping, and hyponatremia among athletes. Recent focus has been put on the detection of biomarker using non-invasive analytical approaches, with sweat being a highly suitable biological fluid due to its easy accessibility and rich biomarker content. The use of wearable analytical platforms integrating electrochemical sensors and capillary-driven fluidic components enables continuous, real-time monitoring of sweat composition, with several electrolytes such as Na^+, Cl^-, and K^+, metabolites such as glucose, lactate, and hormones such as cortisol being primarily targeted. Their sweat content has been show to related to dehydration, stress, exercise intensity, and fatigue events.

However, challenges like biofouling, sensitivity, flexibility, stability, and sample collection persist in wearable device development. Factors such as sweat evaporation, skin contamination, and variability in composition further complicate accurate analysis.

In this context, this thesis focuses on the development of a flexible wearable platform for continuous monitoring of various sweat biomarkers. It involves the development and comprehensive characterization of Ion-Sensitive Field-Effect Transistors (ISFETs) potentiometric sensors for pH, Na^+, K^+ and Cl^- concentrations. Additionally, a solid-state reference electrode, key for the integration of such sensors onto the wearable platform, is successfully fabricated onto a thin-film platinum electrode chip. The sensor and reference electrode integration along with a temperature sensor and capillary-driven

fluidic components into a small flexible platform, is assessed. Different fluidic architectures are explored to enable real-time, low-flow-rate sample monitoring, evaluating different materials and geometric designs under conditions resembling practical use.

Finally, the wearable sensing prototype is evaluated on-body in clinical studies carried out with subjects performing high-intensity cycling sessions in a controlled environment in Lausanne University Hospital. The ISFET sensor on-body performance is compared to that of commercial Ion Selective Electrodes (ISEs) using with discrete samples periodically collected during the cycling sessions. Some trends are elucidated that can be correlated with the athlete's conditions and that evidence the practical application of the presented platform for on-body monitoring of biomarkers.

Table of Contents

1 INTRODUCTION

1.1. SPORTS MEDICINE

The field of sports medicine is on the rise due to the increasing emphasis on physical exercise for a healthy lifestyle. Additionally, the high performance demanded from athletes, supported by new technologies, necessitates continuous monitoring of their vital signs during exercise. Sports scientists consistently pursue innovative technologies, data platforms, and therapies to assist athletes in achieving peak performance while mitigating injury risks throughout a demanding season.[1] Currently, the majority of wearables used in this field focus on monitoring physical or physiological parameters such as body temperature, heart rate, steps, or flow rate. However, these parameters don't give information about the biochemical profile of an athlete in order to prevent soft-tissue injuries, dehydration or cramping. Adequate hydration is critical since an insufficient water intake may result in hypohydration, while excessive intake may lead to hyponatremia, characterized by low serum Na^+ concentration, and with potentially life-threatening consequences [2].

Clinicians frequently rely on blood tests to evaluate patients' health status, considered the gold standard for biochemical analyses. However, this method has inherent limitations. Blood tests are invasive, necessitate trained personnel, and offer a singular snapshot of the patient's condition at the time

of extraction. An alternative analysis gaining significant interest involves utilizing sweat as the sample for analysis [3].

Most of the techniques for blood collection rely on phlebotomy, considered the gold standard method. However, this approach is often associated with discomfort, pain, infection risks, and constraints on the frequency of sampling intervals. Alternatively, saliva, tears and sweat are regarded as attractive non-invasive sources of biomarkers. Compared to other biological fluids, it is steadily gaining interest because its analytes are considered prospective rich indicators of major physiological conditions in a wide range of disciplines.

1.2. ECCRINE SWEAT GLANDS AND THERMOREGULATORY SWEATING

During physical exertion, the muscles generate heat as they work, a result of metabolic processes. This increases body heat, combined with higher environmental temperatures than the skin's temperature, causes heat to transfer from the air to the body. As a consequence, the body's core temperature rises, and this information is relayed to the preoptic hypothalamic region in the brain, which triggers the process of sweating and the widening of blood vessels in the skin (cutaneous vasodilation) to help disperse the excess heat. [4–6] Sweat evaporation stands as the principal mode of heat dissipation during physical exertion. As the body sweats, heat transfers from the body to the sweat on the skin's surface. As this sweat absorbs enough heat, it transitions into water vapor, effectively extracting heat from the body. [7,8]

The eccrine sweat gland is composed of a secretory coil and duct formed by a simple tubular epithelium. Upon stimulation, the clear cells within the secretory coil secrete primary sweat, an ultrafiltrate of plasma. This primary sweat closely resembles the isotonic composition of blood plasma, containing

approximately 135–145 mmol L^{-1} Na^+, approximately 95–110 mmol L^{-1} Cl^-, and approximately 4–5 mmol L^{-1} K^+ [9–13]. During its passage through the duct, Na^+ undergoes passive reabsorption via epithelial Na^+ channels on the luminal membrane and active reabsorption through Na^+/K^+-ATPase transporters primarily located on the basolateral membrane [14]. Similarly, Cl^- is passively reabsorbed via the cystic fibrosis transmembrane conductance regulator present on both luminal and basolateral ductal cell membranes [15]. Consequently, the final sweat excreted onto the skin surface becomes hypotonic concerning Na^+ and Cl^- concentrations [9]. Moreover, the reabsorption rate of Na^+ and Cl^- depends on sweat rate, being the last correlated with the final concentrations of Na^+ and Cl^- in sweat [9].

As sweat rate increases, the secretion rate of Na^+ and Cl^- in precursor sweat tends to rise proportionally more than the reabsorption rate of Na+ and Cl- along the duct. Consequently, this leads to higher final concentrations of Na^+ and Cl^- in sweat [9,16]. The loss rate of potassium K^+ in sweat has been suggested to have an indirect relationship with sweat flow rate, although the underlying mechanism remains unclear [9]. Nevertheless, the final concentration of K^+ in sweat typically mirrors that of blood plasma, with a slightly wider range (e.g. approximately 2–8 mmol/L) [17–19].

1.3. SWEAT ANALYSIS TECHNIQUES

Human eccrine sweat has emerged as a promising biofluid for non-invasive analysis owing to its biomarker-rich content and its accessibility through wearable patches, making it a prime candidate for continuous and real-time monitoring of its composition when integrated with electrochemical sensors within a wearable microfluidic system [20].

Among the multitude of sweat analytes, Na^+ and Cl^- ions are present in the highest concentrations (ranging from 10-100 mM) and, as previously

described, undergo active reabsorption in the body [21]. Their concentration in sweat is affected by the sweat rate, implying that higher sweat rates result in higher concentrations. Consequently, the correlation between their levels in sweat and blood is poor [21]. The clinical significance of measuring Na^+ and Cl^- is limited without accurate sweat rate measurements and correlation with environmental factors [22,23].

Conversely, K^+ ions in sweat demonstrate passive transport, with concentrations ranging 1mM — 18.5 mM. and recent studies indicate better correlation with blood levels, particularly with sweat stimulation [24]. Despite these advancements, the correlation between glucose levels in sweat and blood remains unestablished using wearable biosensors. A strong correlation has been identified between glucose in the interstitial fluid and blood.

Another critical consideration is the considerable variation in sweat pH, which can significantly influence the signals received from enzymatic sensors used in sweat analysis . Monitoring pH levels, which usually range between 3 – 8, can also reflect changes in the concentration of various electrolytes in sweat, and thus help in the assessment of the athlete's metabolic state [21,25].

The need of personalized and in situ health assessment is pushing the use of portable and rapid analytical devices, like the commercial ISEs from Horiba, Ltd. Some studies report the good accuracy of these devices for sweat analysis [26–31]. However, while they show an excellent performance for discrete measurements, their geometry and size make them not compatible for integration in on-body real-time monitoring systems.

Although sweat is an easily accessible biofluid, its production is very slow and very small sample volumes can be collected for analysis in a short period of time. Indeed, exercise-induced sweat rate is typically in the range of 0.5 – 1.4 $\mu L\ cm^{-2}\ min^{-1}$ [32]. Thus, real-time and continuous analysis of sweat

requires the use of analytical platforms or wearable devices able to perform with low sample volumes.

1.4. WEARABLE BIOCHEMICAL SENSORS FOR SWEAT ANALYSIS

The advantages that sweat offers over other biofluids for the non-invasive detection of health issues and the prevention of injuries have driven the researchers to invest sources and efforts in understanding blood-to-sweat biomarker partition pathways, and developing analytical techniques for its analysis. Sweat analysis has gained increasing attention over the past decades, as can be interpreted from the increasing number of publications documented. But there's a field in which the interest has grown abruptly in the last two decades, and this is the development of wearable devices for sweat analysis (Figure 1.1).

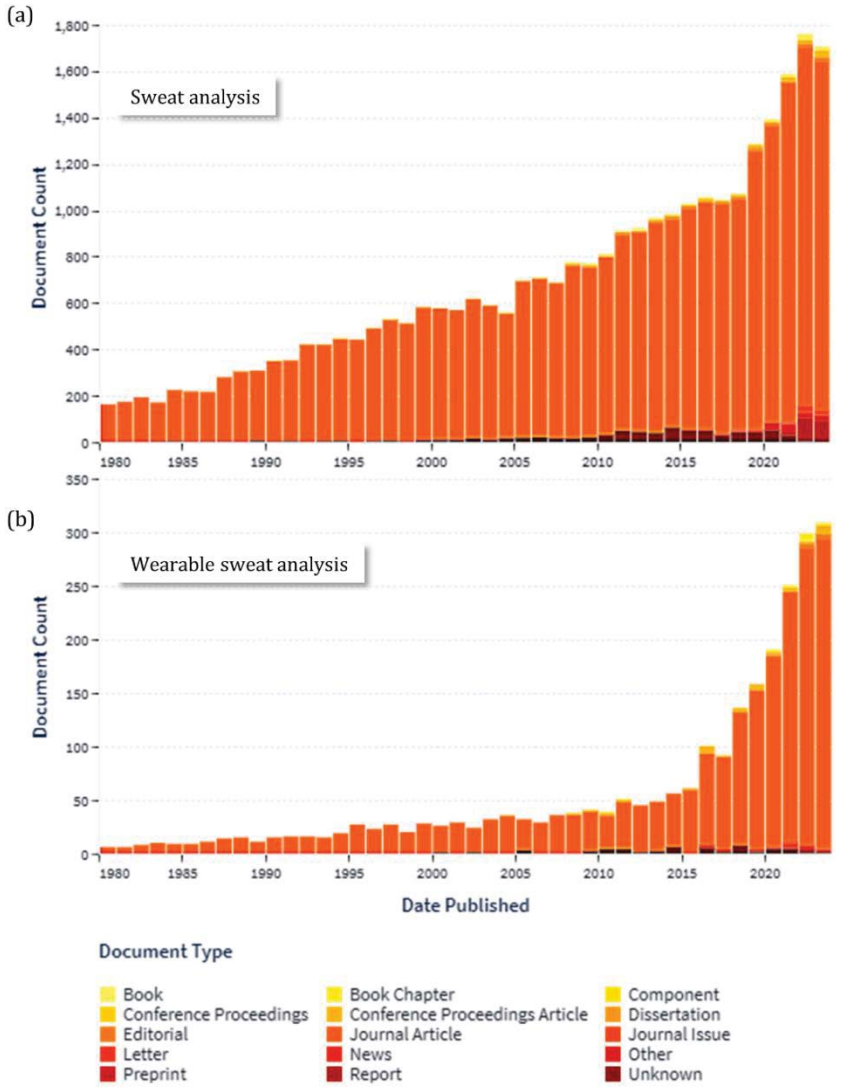

Figure 1.1. Scholarly work of (a) "Sweat analysis" and (b) "Wearable sweat analysis" from 1980 to 2023 based on lens.org [33].

The application on the athletic side is prominent, with wearable technology positioned as the leading fitness trend for the first time in 2016 [34].

Most wearable electrochemical sensor devices reported so far are based on the application of inkjet printing or screen-printing technologies to produce ISEs directly on flexible substrates [35–39]. These show the

advantages of fabrication simplicity and cost effectiveness, as well as easy adaptability to the body. However, they often suffer from a lack of reproducibility and electronic noise due to substrate bending and stretching under moving conditions. Besides, most of them do not incorporate fluidic approaches to continuously drive the sweat to the sensing areas and just an absorbent element in direct contact with the sensor is used for collecting sweat and then carrying out a single measurement.

1.4.1. Challenges in sweat analysis

The analysis of sweat composition through wearable sensors presents unique challenges owing to various factors that can alter analyte concentrations and affect the reliability of measurements. Sweat evaporation and skin contamination are primary concerns as they have the potential to modify the concentrations of analytes within sweat, thereby impacting the accuracy of the obtained data [20]. Additionally, certain analytes present on the skin demonstrate dependence on sweat rate, implying that alterations in their concentrations might not necessarily signify changes in an individual's health status (e.g., an increase in sodium concentration might not indicate dehydration but merely a variation in sweat rate)[21]. Moreover, the variability in sweat rate and composition among different body regions and individuals presents challenges in developing clinically relevant wearable devices for health monitoring. External environmental factors such as temperature, humidity, and physical activity can also influence sweat rate and composition, posing challenges in isolating and accurately measuring specific ions or biomarkers [23].

Silicon-based sensors produced by microfabrication technologies are promising alternatives for this purpose, showing small size and enabling the integration with various interfacing electronic readouts being CMOS-compatible. Specifically, ion-sensitive field-effect transistors (ISFETs) are usually highly robust devices produced at wafer level with a high yield, and

thus can be used for continuous monitoring during long-term exercise practices.

1.5. ISFETs

From an electronic perspective, an ISFET is a MOSFET structure where the gate metal is removed, exposing the insulating layer directly to an aqueous solution. The circuit is then completed through a reference electrode (RE). Therefore, the electronic behaviour of an ISFET is identical to that of MOSFET structures. A schematic representation of both MOSFET and ISFET devices is, and the ISFET's electronic diagram is shown in Figure 1.2. The MOSFET structure consists of a silicon substrate (bulk or substrate) doped with p-type dopants containing two heavily doped n-type silicon regions (diffusion regions) called the source and drain, separated by a channel. An insulating layer of silicon dioxide (SiO_2) is grown on top of this, followed by the deposition of a metal (gate electrode). [40]

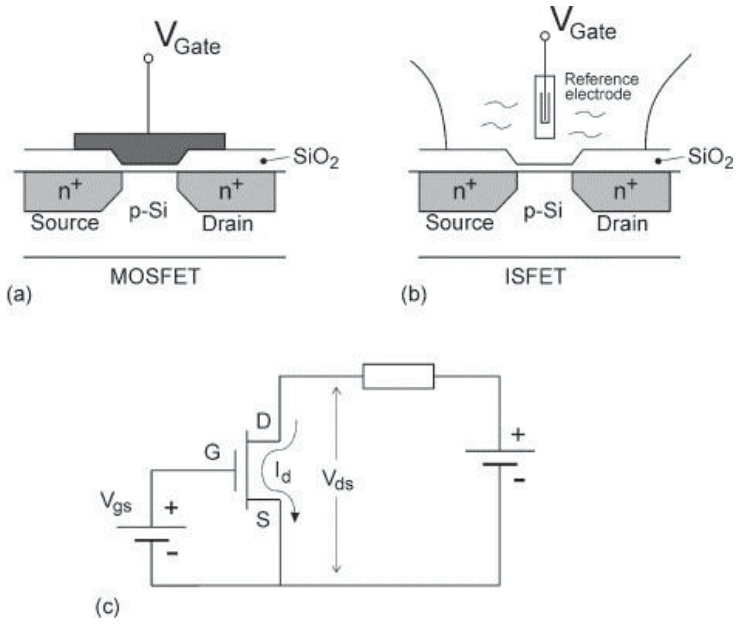

Figure 1.2. Schematic representation of MOSFET (a), ISFET (b), and electronic diagram (c). Reproduced with permission. [40] Copyright 2003 Elsevier.

The MOSFET behavior is based on the field effect, which is an electrical field between the drain and the source (V_{DS}) created when a perpendicular potential is applied to the metal gate (V_{GS}). Then, electrons are attracted to the semiconductor's surface, creating a channel between the drain and source, resulting in a a drain current (I_{DS}) between them. The general equation that relates all these parameters and the characteristics of the gate materials for a specific case of VDS value is expressed in Equation 1.1:

$$I_{DS} = \overline{\mu}_n C_{OX} \frac{W}{L}\left[(V_{GS} - V_{th})V_{DS} - \frac{V_{DS}^2}{2}\right] \text{ for } V_{GS} - V_{TH} \geq V_{DS} \quad \text{Equation 1.1}$$

Where V_{TH} is the threshold voltage or the minimum gate voltage to achieve the electrical field between the drain and the source; μ_n is the surface mobility of the electron; W is width of the channel; L is the length of the channel; and C_{OX} is the capacitance of gate insulator per unit area.

In the case of an ISFET, the metal gate of a MOSFET is removed and it is substituted by an electrolyte and a reference electrode. Then the dielectric layer (typically oxide layers) is in direct contact with the liquid media and the interaction between them causes an electrical double layer and consequently an electrochemical potential drop depending on the solution composition in a similar way that happens in a glass electrode. This potential drop is recorded by the RE.

This new potential caused by electrochemical interactions between the gate dielectric and the solution will depend on the material properties of the dielectric, as well as on the solution chemical composition, particularly on its pH value. The dependence of this surface potential with pH, in an analogous way as the glass electrode [41], can be expressed by an equation similar to the Nernst equation (Equation 1.2).

$$I_D = \overline{\mu}_n C_{OX} \frac{W}{L}\left[(V_{GS} - V_{th})V_{DS} - \frac{V_{DS}^2}{2}\right] \text{ for } V_{GS} - V_{th} \geq V_{DS} \quad \text{Equation 1.2}$$

Where Ψ_0 is the surface electrode potential, k is the Boltzmann constant, T is the temperature in K, q is the charge of the electron, pH_{pzc} is the pH at the point where the net charge due to the active centers of the surface is zero, and β is a constant depending on the reaction capacity and the density of active centers of the gate oxide, temperature, and the capacity associated with the electrical double layer of the interface. The value of β depends on the nature of the inorganic oxides (sensitive to the H^+ ions) deposited in the gate of the ISFET (SiO_2, SiN_4, Al_2O_3, Ta_2O_5). At high values of β the pH response is very similar to the Nernst Equation (presented later), also displaying a linear relationship between the measured potential.

This interfacial potential difference, Ψ_0, affects the threshold voltage as shown in Equation 1.5. Therefore, it is the responsible for the variation of the n-channel conductance.

$$V_{th}^{*} = V_{FB} + V_{ref} + \psi_0 - \frac{Q_B}{C_{ox}} + 2\phi_F \qquad \text{Equation 1.5}$$

The most common method to carry out ISFET measurements consists of maintaining the drain voltage, V_{DS}, and drain current, I_{DS}, at constant values. This means that any change in the interfacial potential difference, Ψ_0 is compensated by applying additional and opposite in sign voltages to the reference electrode.

As previously mentioned, the selectivity and sensitivity of pH-sensitive ISFETs are determined by the properties of the dielectric/electrolyte interface, specifically related to changes in the interface potential Ψ_0. The theory that explains the variation of the Ψ_0 with pH is the Theory of Active Centers or Local Links (Site-binding theory). This theory, initially proposed by Yates et al. [42] for colloidal SiO_2, and afterwards was applied by Siu and Cobbold [43]to elucidate the operation of pH-sensitive ISFETs. This theory assumes an ideally polarizable dielectric/electrolyte interface that achieves a state of chemical and electrostatic equilibrium. Due to these equilibriums,

there is no transfer of charge between both phases or, if any, it must be extremely slow. A common characteristic of silicon oxides or nitrides (gate materials of ISFETs) is that they all possess a certain surface density, of donor or acceptor groups of H^+ (see figure Figure 1.3) The Active Centers Theory implies that, due to the amphoteric nature of these surface groups (Active Centers), the surface can be neutral, positively charged (acidic reactions), or negatively charged (basic reactions). By developing equilibrium equations along with the electrostatic double layer model, the relationship between the equilibrium surface potential, Ψ_0, and the pH of the solution can be found as shown in Equation 1.4.

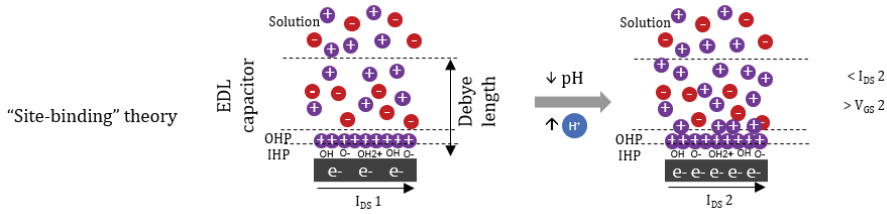

Figure 1.3. Scheme of the layers formed when an ISFET is immersed in an electrolyte solution, that enable pH sensing.

As shown from the constant values, this equation is very similar to the Nernst Equation (Equation 1.6), also displaying a linear relationship between the measured potential and the negative logarithm of the activity of a proton (pH), with a sensitivity of 59 mV decade^{-1} in the case of monovalent ions. For small β values, the sensitivity is lower than Nernstian and the high β values, the senstitivity approaches to Nernstian.

Otherwise, the response of an ISFET modified with a selective membrane is obtained by measuring the potential generated across the interface between the membrane and the electrolyte, due to the equilibrium established by the species being detected at the surface of the membrane. The potential response changes following the Nernst equation (Equation 1.6).

$$E = E^0 - \frac{RT}{z_i F}\ln(a_i) \qquad \text{Equation 1.6}$$

where E is the measured potential, E0 the standard potential, R the gas constant (8.314 J/Kmol), T the temperature in K, zi the charge of an ion, F the Faraday constant (96500 C/mol electrons) and ai the ion activity in the solution.

When ISFETs exhibit sensitivity to other interferent ions, a Nernst equation variant is used, including Kpot selectivity coefficient, the Nikolsky-Eisenman (Equation 1.7).

$$E = E^0 - \frac{RT}{z_i F} \ln\ (a_i + \sum K_{ij}^{pot} \times a_j^{z_i/z_j}) \qquad \text{Equation 1.7}$$

1.6. Data interpretation

Calibration is required before the analytical determination of the sample and to assess the sensor response characteristics. In potentiometry, the typical one is the external standard calibration, which relies on running a series of standards and constructing a calibration curve with the potentials in the Y and the logarithm of the ionic activities in X. Considering Nernst equation, the resulting equation would be as follows:

$$Calibration\ curve \rightarrow \ \ E = a - b \times \text{Log}\ (activity)$$

where a represents the potential when there's no presence of the analyte or it is < LOD and b is the sensitivity of the device.

Activity values can be obtained from the known concentrations of all the ionic species in a solution through the Debye-Hückel equation. When working with artificial sweat solutions, it's important to note that amino acids have different ionic groups, which may undergo protonation or deprotonation depending on the solution's pH and pKa values. It has been considered to calculate the activities of the biomarkers when the calibration has been carried out in artificial sweat media.

In situations where interfering species impact the sensor's response, the calibration curve should fit the Nikolsky-Eisenman equation:

$$Calibration\ curve \rightarrow \ E = a - b \times \mathrm{Log}\ (a_i + \sum K_{ij}^{pot} \times a_j^{z_i/z_j})$$

In this work, external calibrations were experimentally performed following two distinct methodologies: calibration using standard solutions and calibration via the addition of a concentrated stock solution to a solution. In the first approach, stock solutions with varying concentrations of the analyte of interest were prepared. The second method required accounting for the added volumes when determining the final concentration of the solution. The media in both cases were deionized (DI) water and artificial sweat solutions, depending on the test's purpose.

Independently of the calibration method used, to consider that the calibration line is satisfactory, the criteria established were:

- A correlation factor R > 0.99.

- The residual relative errors against the theoretical values must be < 20%.

The data was analysed with a 95% significance level (α = 0.05). The standard deviation (SD) of the data can help us evaluating the repeatibilty and reproducibility of the measurements.

The limits of agreement define the interval in which 95% of measurement differences were expected to fall. The lower and upper limits were computed as follows:

$$Limits\ of\ agreement = \ \bar{x} \pm \ 1.96 \ \times SD$$

Where $\bar{x}$ is the mean value, and 1.96 is the z value, which is given by the 95% significance level. It means that 95% of the area under a normal curve should lie within approximately 1.96 SD of the mean.

The interval of confidence (CI), which is the range of values that one can be 95% certain contains the true mean of the population, was calculated with the following equation:

$$Confidence\ interval = \ \bar{x} \pm \ 1.96 \ \times \frac{SD}{\sqrt{n}}$$

Where n is the size of the data.

The CI can give us information about the bias of the data when it is compared to the reference values. When the relative differences are plotted, as in Bland-Altman or scatter plots, a CI including 0 denotes the absence of significant bias.

If the results are not statistically different at the given level of significance, linear regressions comparing two methods should yield a straight line of approximately unity slope and zero intercept. This is used to evaluate the agreement between the two methods. On the other hand, the coefficient of determination (R^2) is used to assess the strength of the relation between two variables, not the agreement between them.

1.7. State-of-the-art on ISFETs in Wearable Prototypes

Few wearable platforms integrating ISFET sensors have been reported, probably due to the challenges presented above. In this section, the current state-of-the-art of the devices using ISFETs sensing technology for the on-body analysis of sweat will be presented. First, Jin-Hyeok Jeon and Won-Ju Cho integrated a pH ISFET into a flexible transparent substrate (Figure 1.4a), achieving high sensitivity in detecting human sweat pH [44]. Researchers, such as Eun-Ki Hong and Won-Ju Cho, introduced nanomaterials to optimize the gate channel (Figure 1.4b), enhancing ISFET performance in terms of pH sensitivity, drift rate and hysteresis. This enhancement significantly mitigates device non-idealities, enabling accurate detection of human pH levels [45]. One of the challenges in the field of wearable potentiometric devices is the fabrication of a miniaturized, robust and chemically stable reference electrode. Pursuing this goal, Sang-Chan Park et al. innovatively integrated an Ag/AgCl RE into a single-chip ISFET sensor system, achieving miniaturization and facilitating real-time, continuous monitoring of sodium ions in human sweat (Figure 1.4c)[46]. Going further in this direction, Shi Qiu et al. reported a RE array (2 × 10 mm, 42 × 4) (Figure 1.4d) to achieve

excellent pH ISFET sensing performance [47]. All the previously mentioned devices could monitor a single biomarker, and its performance has not… The simultaneous monitoring of multiple biomarkers in real-time is essential to obtain relevant information about individual's health, as the physiological state of the individual may alter more than one parameter. Furthermore, demonstrated how big data can be used to find correlations between wearable sensor readings and health status, even without a complete understanding of their causal relationship [48]. Therefore, integrating multiple functionalities into ISFET sensors has been pivotal for comprehensive health monitoring.

Shogo Nakata et al. combined flexible temperature and ISFET sensors for real-time sweat pH and skin temperature measurements (Figure 1.4e) [49]. Erick Garcia-Cordero et al. introduced ultra-thin ISFET sensors and microfluidic systems onto a single silicon chip, creating a compact wearable device for real-time monitoring of pH, Na^+, and K^+ concentrations in sweat (Figure 1.4f) [50].

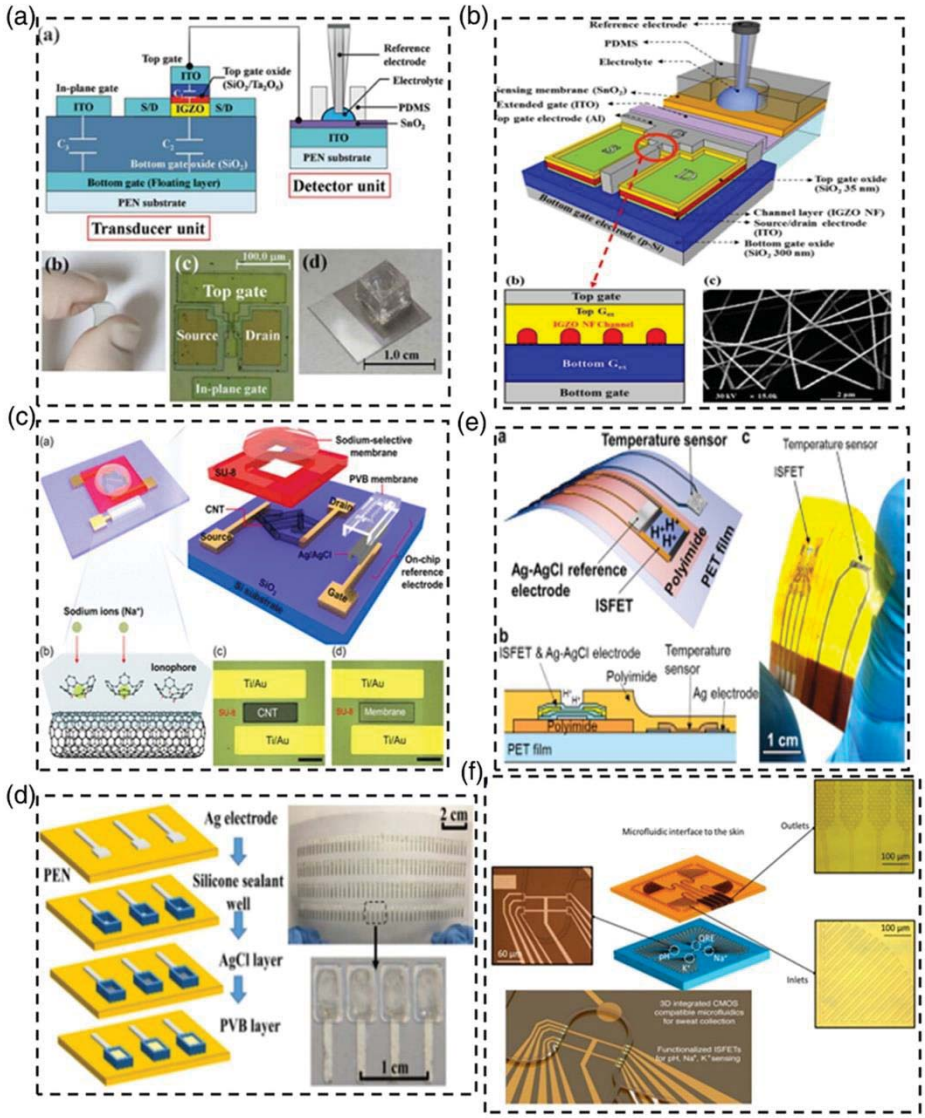

Figure 1.4. (a) Schematic diagram of IG-ISFET sensor for wearable pH detection. Reproduced with permission. [44] Copyright 2020 Taylor & Francis. (b) Structural diagram of DG-ISFET flexible sensor with nanofiber channels. Reproduced with permission. [45]. Copyright 2021 Elsevier. (c) ISFET sensor with a newly designed RE in a system-on-chip. Reproduced with permission. [46] Copyright 2017 IEEE. (d) The manufacturing process of Ag/AgCl RE array on a plastic substrate. Reproduced with permission. [47] Copyright 2018 RSC. (e) Schematic illustration of the integrated ISFET sensor for pH detection in sweat and skin surface temperature monitoring. Reproduced with permission. [49] Copyright 2017 ACS. (f) The schematic diagram of an integrated ISFET miniature sensor for multi-ion detection with small RE and sensing area of a few square microns. Reproduced with permission. [50] Copyright 2017 Elsevier.

Additionally, we have summarized in Table 1.1 the few publications reporting off-line sweat samples determination with Na+ ISFETs.

Table 1.1. State-of-the-art in Na+ ISFETs for sweat sensing.

Concentration range [M]	Sensitivity [mV/dec]	Interference tests	Sweat samples validated	Reference method	Relative error [%]	Ref.
$10^{-5}-1$	55[a]	No	5	Potentiometric[b]	NG[c]	[51]
$10^{-3}-10^{-1}$	57	Yes	2	Potentiometric[d]	12%	[29]
$10^{-4}-1$	57	Yes	1	Potentiometric[b]	4%	[52]

[a]The total sensitivity is the sum of Na+ ISFET (55) and Ag/AgCl (55) sensitivities. bRoche Hitachi 912 chemistry analyzer. cNG: Not given. dHoriba LAQUAtwin Na+ 11.

As we move forward, the aspiration is to design an ISFET platform flexible, robust, reusable, with outstanding sensing performance and stability. Although advances have been made, the existing ISFET-based sensing systems do not yet entirely meet these criteria.

2 OBJECTIVES

The need for improving personalized and preventive medicine through the rapid detection of physiological parameters in a non-invasive manner has prompted the development of wearable platforms that can be adhered to the skin and show the ability to detect not only physical but biochemical parameters in sweat biofluid. The latter has been addressed in a wide number of technological approaches published during the last decade with more or less success. This, together with the investment done by private companies are a clear indicator of the interest that this field has drawn. However, none of the reported platforms has arrived to the market because monitoring sweat biochemical parameters has posed many challenges that could not be fully worked out.

In this context, and in the framework of a project funded by the Swiss National Science Foundation, entitled "Wearable Platform For Real-Time Monitoring Of Biomarkers In Sweat", this Thesis was focused on developing a multiparametric platform that enabled the continuous monitoring of different electrolytes in sweat related to the hydration status and that could be of potential interest for athletes and in sports medicine in general. Unlike previously reported approaches, the aim of this work was the use of robust potentiometric transducers whose fabrication process was standardized at the IMB-CNM and that could be packaged on flexible substrates and coupled with simple fluidic components together with tailor-made electronics to produce an easy-to-wear

device while doing exercise. This main objective included the following specific objectives:

1. **Development of potentiometric sensors for pH, Na^+, K^+ and Cl^- that could jointly be implemented on flexible substrates.**

   Functionalizing Si_3N_4 ISFETs with ion-selective membranes or recognition elements to accurately and selectively determine biomarkers within the physiological concentration range found in sweat.

2. **Validation of the sensors for the measurement of the selected biomarkers in sweat**

   Evaluating the ISFETs accuracy in the determination of biomarkers in a continuous flow of human sweat. This involves comparing the determination results with the concentrations measured with reference methods.

3. **Development of a solid-state reference electrode, required to be integrated together with the sensors for robust potentiometric measurements.**

   Fabrication of a miniaturized reference electrode, capable of keeping its properties in a wearable application. This requires testing materials able to offer the electrode long-term potential stability, minimal drift and noise, mechanical and chemical robustness, minimal swelling and electrolyte leaching.

4. **Design of the wearable platform architecture and connection to a tailor-made readout electronics.**

   Designing and fabricating platforms that integrate the sensors into a small surface, taking into account the sample flow requirements.

5. **Integration of a fluidic component in the wearable platform**

Designing a fabricating a fluidic structure to drive the athlete's regional sweat over the sensors, offering continuous and real-time sampling. Different materials, based in capillary transport, should be tested to avoid external pumping components. The material and design may offer maximum flow rate and complete sample renewal.

6. **Validation of the wearable prototype on-body and study of the correlation of the biomarker concentration profiles recorded during exercise with the user physical status.**

   Evaluation of the wearable sensing platform with the fluidic components on an athlete performing physical exercise during long periods. The platform should be able to precisely monitor the biomarkers concentration changes throughout the session in real-time. The accuracy of the extracted data would be given by sweat samples determination with reference methods. The trends could be correlated the athlete's physiological status.

3 MATERIALS AND METHODS

3.1. REAGENTS AND SOLUTIONS

All reagents were of high purity, analytical grade or equivalent.

The following components, used for preparing calibration solutions and artificial sweat solutions, were all purchased from Sigma-Aldrich (St. Louis, MO, USA): Sodium chloride (NaCl), potassium chloride (KCl), potassium nitrate (KNO_3), sodium hydroxide (NaOH), sodium sulphate (Na_2SO_4), sodium bicarbonate ($NaHCO_3$), magnesium chloride hexahydrate ($MgCl_2 \cdot {}_6H2O$), sodium phosphate anhydrous monobasic (NaH_2PO_4), dl-alanine, l-(+)-arginine, l-(+)-aspartic acid, l-(+)-citrulline, l-(+)-glutamic acid, glycine, l-histidine, l-isoleucine, l-leucine, l-(+)-lysine monohydrochloride, l-(+)-ornithine monohydrochloride, l-phenylalanine, l-threonine, l-(–)-tryptophan, l-tyrosine, l-valine, ammonium hydroxide, uric acid, urea, creatinine, thiamine hydrochloride, riboflavin, nicotinic acid, d-pantothenic acid calcium salt, ferrocenemethanol 97% (FcMeOH) and Tris(hydroxymethyl)aminomethane (Tris, Trizma base). Hydrochloric acid (37%) (Panreac AppliChem, Barcelona, Spain) was diluted and used for pH ISFET calibrations.

The pre-encapsulating layer used to protect the electrical contacts of the ISFET was prepared with the diacrylated urethane oligomer (Miramer PE210), the 1,6-hexanediol diacrylate cross-linker (HDDA) (Miramer M200) (Miramer®, Miwon, South Corea) and the Irgacure 651 photoinitiator (Ciba

Geigy). The proportions were 70% oligomer, 27% crosslinker, and 3% photoinitiator [53].

Before the membrane deposition, the ISFET gate was activated and silanized. For that, 31% hydrogen peroxide (H_2O_2) (BASF, Ludwigshafen, Germany), 5% hydrofluoric acid (HF) (Honeywell, United States), NaOH pellets (Sigma-Aldrich), and 3-(trimethoxysilyl) propyl methacrylate (Sigma-Aldrich) reagents were employed.

The polymeric matrix for producing the ISFET selective membranes included the Ebecryl® 270 oligomer (Allnex Resins, Germany GmbH), the HDDA cross-linker (Miramer M200) (Miramer®, Miwon, South Corea), and the Irgacure 651 photoinitiator (Ciba Geigy). The following ionophores and selective compounds were added to the matrix: 4-tert-butylcalix[4]arenetetraacetic acid tetraethyl ester (Ionophore X) (Sigma-Aldrich) for Na^+, valinomycin for K^+ (Sigma-Aldrich), and tridodecylmethylammonium chloride (TDMACl) (Sigma-Aldrich) for Cl^-. Bis(2-ethylhexyl)sebacate (DOS) (Sigma-Aldrich) was used as plasticizer and potassium tetrakis(4-chlorophenyl)borate (KTClPhB) (Fluka, Honeywell, United States) was added as a lipophilic anionic additive in the Na^+ and K^+ membrane formulations. The mixtures were solubilized in tetrahydrofuran (THF) (Fluka).

96%-purity ethanol (Panreac) has been used to clean the electrodes. 3-(trimethoxysilyl) propyl methacrylate silane agent was dissolved in 99.9 % purity ethanol (Panreac) to carry out the ISFET gate functionalization.

For the solid-state RE fabrication, polyvinyl butyral (PVB), and 99.9% HPLC quality methanol from Sigma-Aldrich, together with an Ag/AgCl ink (82/18) from Creative Materials (USA) were used.

The reagents used to synthesize the polyHEMA-based hydrogels were 2-hydroxyethyl methacrylate (HEMA) (Sigma-Aldrich), ethylene glycol (EG) (Honeywell), ethylene glycol dimethacrylate (EGDMA) (Sigma-Aldrich), 2,2'-dimethoxy-2-phenylacetophenone (DMPA) (Fluka), [2-

(methacryloyloxy)ethyl] trimethylammonium chloride (METAC) and 2-acrylamido-2-methyl-1-propanesulfonic acid (AMPS).

Stock solutions of NaCl, KCl, KNO_3, NaOH, and Tris buffer, as well as a universal buffer solution containing 0.04 M H_3BO_3, 0.04 M acetic acid, 0.04 M H_3PO_4, and 0.1 M KNO_3 (pH 2), were prepared in deionized water and used for the sensor characterization. The calibration solutions were prepared from 10^{-4}, 10^{-2}, 10^{-1} and 1 M stock solutions. Commercial buffer solutions from Panreac AppliChem ranging from pH 2-10 were used for pH ISFET batch characterization. Commercial REs used KCl 3M as external electrolyte.

An artificial sweat solution was prepared to carry out the analytical assessment of the sensors based on the formulation reported in [54]. The solution contained electrolytes, amino acids, nitrogenous substances, and vitamins as indicated in **Table 3.1.** Composition of the artificial sweat solution.Table 3.1. A 35x concentrated stock solution of this composition was prepared and stored aliquoted at -20°C until use. Calibration solutions were also prepared in this matrix by serial dilutions and spikes with TRIS, NaCl and KNO_3 at five different concentration levels:

C1: pH 4, 10 mM NaCl and 2 mM KNO_3

C2: pH 5, 20 mM NaCl and 4 mM KNO_3

C3: pH 6, 40 mM NaCl and 8 mM KNO_3

C4: pH 7, 80 mM NaCl and 16 mM KNO_3

C5: pH 8, 160 mM NaCl and 32 mM KNO_3

Table 3.1. Composition of the artificial sweat solution.

Components	Concentration (M)
Electrolytes	
Sodium sulphate (Na_2SO_4)	1.0E-04
Sodium bicarbonate ($NaHCO_3$)	1.0E-03
Potassium chloride (KCl)	1.0E-04

Magnesium chloride hexahydrate ($MgCl_2 \cdot 6H_2O$)	8.2E-05
Sodium phosphate anhydrous monobasic (NaH_2PO_4)	1.0E-04
*Organic acids and carbohydrates	
Lactic acid (sol 1 M)	1.4E-02
Pyruvic acid ($C_3H_4O_3$)	1.8E-04
d(+)-Glucose ($C_6H_{12}O_6$)	1.7E-04
Amino acids	
dl-Alanine ($C_3H_7NO_2$)	5.7E-04
l-(+)-Arginine ($C_6H_{14}N_4O_2$)	7.8E-04
l-(+)-Aspartic acid ($C_4H_7NO_4$)	3.4E-04
l-(+)-Citrulline ($C_6H_{13}N_3O_3$)	4.0E-04
l-(+)-Glutamic acid ($C_5H_9NO_4$)	3.7E-04
Glycine ($C_2H_5NO_2$)	3.9E-04
l-Histidine ($C_6H_9N_3O_2$)	5.2E-04
l-Isoleucine ($C_6H_{13}NO_2$)	1.7E-04
l-Leucine ($C_6H_{13}NO_2$)	2.1E-04
l-(+)-Lysine Monohydrochloride ($C_6H_{14}N_2O_2 \cdot HCl$)	1.5E-04
l-(+)-Ornithine Monohydrochloride ($C_5H_{12}N_2O_2 \cdot HCl$)	1.5E-04
l-Phenylalanine ($C_9H_{11}NO_2$)	1.3E-04
l-Threonine ($C_4H_9NO_3$)	4.5E-04
l-(−)-Tryptophan ($C_{11}H_{12}N_2O_2$)	5.5E-05
l-Tyrosine ($C_9H_{11}NO_3$)	1.7E-04
l-Valine ($C_5H_{11}NO_2$)	2.5E-04
Nitrogenous substances	
Ammonium hydroxide (NH_4OH) 1 M solution	5.2E-03
Uric acid	5.9E-05
Urea (CH_4N_2O)	1.0E-02
Creatinine	8.4E-05
Vitamins	
Thiamine hydrochloride ($C_{12}H_{17}ClN_4OS \cdot HCl$)	5.0E-04
Riboflavin ($C_{17}H_{20}N_4O_6$)	2.0E-04
Nicotinic acid ($C_6H_5NO_2$)	4.1E-02
d-Pantothenic acid calcium salt ($(C_9H_{17}NO_5)_2Ca$)	1.0E-02

*not included in the final artificial sweat solution

For the aptasensor development, the Si_3N_4 ISFET gate was activated and functionalized with an aldehyde-silane, 11-(triethoxysilyl)undecanal (TESUD). 90 % purity TESUD was purchased from abcr (Germany). This reagent needs to be treated under the fume hood and, if possible, stored under a N_2/Ar atmosphere to avoid hydrolysis and self-condensation.

A goat IgG antibody labelled with tetramethylrhodamine isothiocyanate flurophore (TRITC; excitation peak at 557 nm and emission peak at 576 nm), was purchased from Sigma-Aldrich and used to test the effective silanization process of the ISFET gate.

ISFET gates were functionalized with an aptamer that had been previously reported to be sensitive to cortisol [55,56], but changing the thiol-end group used in the previous report, by an amine-end group at the 5' terminal of the oligonucleotide sequence. The full sequence was the following. 5'-amine-C6-GGA ATG GAT CCA CAT CCA TGG ATG GGC AAT GCGGG GTG GAG AAT GGT TGC CGC ACT TCG GCT TCA CTG CAG ACT TGA CGA AGC TT-3'. It had 85 nucleotides and was provided by Kaneka Eurogentec (Germany).

Ethylenediaminetetraacetic acid tetrasodium salt (EDTA) from Sigma-Aldrich was used to prepare a Tris-EDTA (TE) buffer solution, employed to stabilize the DNA sequences of aptamer solutions. Sodium cyanoborohydride ($NaBH_3CN$) from (Sigma-Aldrich) solution was also used during the covalent immobilization of the aptamer to the silanized ISFET gate.

Bovine Serum Albumin (pI ~4.7) (BSA, ≥ 98%, Sigma-Aldrich) was employed to block any empty areas on the ISFET gate upon aptamer immobilization. This blocking agent was use to avoid the non-specific interaction of any biomolecule present in the sample on the ISFET gate surface.

The solutions used for the preparation of sensors and characterizations are the following:

Two solutions were tested for functionalizing the Si_3N_4 ISFET gate: a 99 % ethanolic solution containing 5% TESUD and 5% 0.1M acetate buffer at pH 5.6 [57] and a 99 % ethanolic solution containing 20% (v/v) TESUD [58].

A stock solution of the TRITC-antibody conjugate was purchased in 0.01 M phosphate buffered saline, pH 7.4, containing 0.1% sodium azide as a preservative. Further dilution of the antibody stock solution in a 1/30 ratio in phosphate-buffered saline (PBS) (x1) used in our studies.

A 10 mM Tris buffer solution containing 1mM EDTA was prepared in deionized water. The solution was pH was adjusted to 7.5-8 with HCl 30% and sterilized by filtration using a 0.22-μm filter.

Aptamer solutions were prepared as follows. The aptamer was purchased lyophilized and was reconstituted by adding TE buffer solution, to get aliquots containing 100 μM aptamer concentration. These solutions were stored at -20°C, until use. At those storage conditions, the aptamer was stable for not more than 5 freeze-thaw cycles and 24 months.

A $NaBH_3CN$ solution was prepared using the appropriate safety measures taking account its corrosiveness. A 5 mM solution was prepared by dissolving the proper amount of $NaBH_3CN$ in PBS solution.

A 1% BSA (w/v) solution was prepared in PBS and stored at 4 ºC until use.

The Cortisol Binding Buffer (CBB) aqueous solution was used that consisted of 50 mM Tris (pH 8) containing 137 mM NaCl, and 5 mM $MgCl_2$. The pH was adjusted to 7.4 with diluted HCl.

3.2. ISFETs Fabrication

ISFETs were selected to be integrated in the wearable device based on the group's previous experience. The good performance of sodium, potassium,

chloride, calcium and nitrate ISFETs has previously been reported [59–62]. In this work, ISFETs were produced on BESOI (bonded and etch-back silicon on insulator) wafers that enabled a more simple encapsulation procedure than the one used in the group on a common basis, while robustly protecting the device against electrical discharges [63]. Typically, ISFET chips require a protective encapsulation layer covering the entire chip edge to insulate the substrate from the solution. However, using BESOI wafers, this is unnecessary. BESOI wafers are formed by three layers: a thick silicon substrate, an intermediate silicon oxide layer, and an upper thin silicon nitride layer. The SiO_2/Si_3N_4 passivation layer covers the entire surface up to the edges and ensures its insulation [64] (Figure 3.1a). ISFETs were fabricated in the Clean Room for Micro and Nanofabrication of the IMB-CNM according to standard photolithographic techniques [65,66]. In Figure 3.1b, the layout of the masks used for a chip's fabrication is shown. The chip size was 3 x 3 mm^2.

A particular wafer-level pre-encapsulation process was developed in this work to facilitate the further chip encapsulation process on the substrate and the posterior deposition and anchoring of the membranes to the ISFET surface. Besides, this process enhanced the reproducibility of the sensor fabrication and provided a planar surface of the pre-encapsulation layer required for ISFET integration in the flow system of the wearable device, as will be explained in Chapter 6. The encapsulation process consisted of defining a 232-µm thick -layer of the photopolymer on the wafer that left the contact pads and the gate area opened to the environment. As shown in Figure 3.1c, the opened area around the ISFET gate defined a 1-mm diameter well where the membranes were deposited. Working in this way, membrane layers showing a reproducible thickness and protected against mechanical stress were produced. The prepolymerization solution was spin-coated on the wafer and then irradiated under a 365 nm UV light using a mask designed for patterning definition.

Chips were individually diced from the wafer and fixed to printed circuit board (PCB) substrates for wire bonding and final packaging. Rigid and flexible PCB substrates were used for the sensor analytical characterization [67], and the eventual production of the wearable device, respectively. The final packaging was carried out by depositing an additional layer of the photocurable polymer that protected the contact wires and pads of the PCB strips, following a custom-made photolithographic method developed at the IMB-CNM [68].

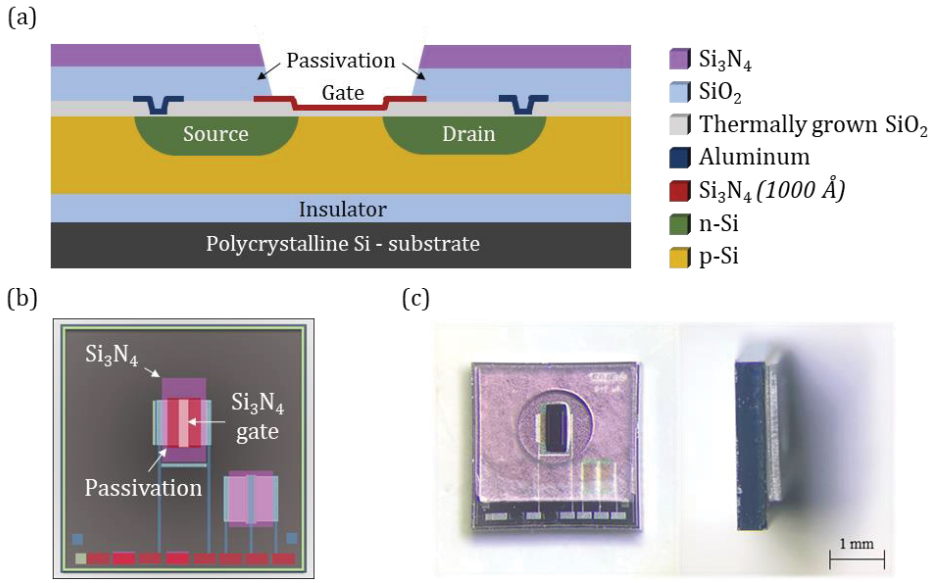

Figure 3.1. ISFET's structure and components. (a) Cross-section view of the different layers and their materials composition. (b) Layout of ISFET design illustrating different colours the layers of the sensor. (c) Top *(left)* and side *(right)* images of a chip with pre-encapsulation layer.

As introduced earlier, pH ISFETs inherently respond to changes in pH, hence, the term "pH ISFETs" refers to bare ISFETs devoid of any selective membrane. Once encapsulated, their treatment primarily involves the removal of the SiO_2 layer resulting from environmental oxidation on their gate, exposing the Si_3N_4 layer, which is more sensitive to pH changes. Based on the conventional HF wet etching method [69], our group validated a procedure that involved immersing the ISFETs in a 5% HF solution for 10

seconds followed by a subsequent immersion in a 2.5% NaOH solution for 30 minutes. It was implemented on pH ISFETs immediately before their use.

Ion-selective membranes were deposited on the well, defined around the ISFET gate, as described above. This is a multi-step process, consisting of hydration/activation, silanization, deposition of prepolymer mixture, and photopolymerization. In this thesis, a new methodology was developed for depositing the membranes on Si_3N_4 gate ISFETs, as they had traditionally been deposited on SiO_2 gate ISFETs. The hydration/activation step in this work involved immersing the sensors in oxidising or a basic media to promote the formation of Si-OH moieties and the deprotonation of the hydroxyl groups. Then, a silanization process was carried out using a 3-(trimethoxysilyl) propyl methacrylate solution in absolute ethanol (1:10 v/v) dispensed in the ISFETs gate well. Then, the silanized ISFET substrate was dried in an oven at 80°C for one hour. Further details regarding the chemical mechanisms behind this process can be found in Chapter 4.

Three membrane compositions for Na^+, K^+ and Cl^- ions detection based on photocurable urethane polymers were prepared following the protocols described elsewhere [61,70–73]. The polymeric matrix of the membranes consisted of a urethane diacrylate oligomer (Ebecryl® 270), a crosslinker (HDDA), and a photoinitiator (Irgacure 651), mixed in an 81:17:2 wt/wt ratio. The oligomer provided mechanical consistency to the membrane. Acrylic oligomers are among the most widely used in UV-curable systems due to their high reactivity and low volatility. HDDA is a monomer used as reactive diluent and a crosslinker or crosslinking agent. Low molecular weight monomers like HDDA are usually introduced into the polymer composition to reduce the viscosity of the oligomers and to increase the cure speed. The addition of a photoinitiator to the mixture is necessary to trigger the radical polymerization reaction.

Once the polymeric solution was prepared, it was mixed with the specific ionophores, and other components including a plasticizer agent and some

additives, as indicated in Table 3.2, to obtain the ion-selective membrane cocktail previously reported [61,71,74,75]. The components were dissolved in THF, and the membrane cocktail was homogenized in an ultrasonic bath until a homogeneous solution was obtained. Then, the excess of solvent was evaporated at room temperature overnight.

Table 3.2. Composition of the ion-selective membranes.

Sensitive ion	**Ionophore (wt%)**	**Plasticizer (wt%)**	**Additives**	**Polymer matrix (1) (wt %)**
Na^+	Ionophore X 1.8%	DOS 38.6%	KtClPhB 0.4%	59.2%
K^+	Valinomycin 2.0%	DOS 38.5%	KtClPhB 0.5%<	59.0%
Cl^-	TDMACl 50%	—	—	50.0%

(1) Polymeric matrix: 82 % Ebecryl 270, 17% HDDA, 0.5% Irgacure 651.

The prepolymer solutions were manually deposited by drop-casting, filling the wells defined over the ISFET gates (3 μL). The membranes were cured in an oxygen-free atmosphere (box with N_2 flow) by exposing them to UV light using a standard mask aligner equipment with radiation of 22 mW cm^{-2} at the wavelength of 365 nm. The exposure time was 15 s for Na^+ and K^+ membranes, and 60 s for Cl^-. This resulted in a membrane of the same thickness as the pre-encapsulation well (232 μm).

3.3. WEARABLE PATCH SENSORS AND MATERIALS

The wearable platform included four ISFETs, a Pt thin-film electrode, and a temperature sensor. The ISFETs were fabricated as described in section 3.2. The Pt thin-film electrodes were fabricated in the Clean Room for Micro and Nanofabrication of the IMB-CNM according to standard photolithographic techniques [76]. The chip size was 3 x 3.5 mm^2. The temperature sensor consisted of a commercial 10 kOhm thermistor (Saitama Murata Manufacturing, Kyoto, Japan).

The substrate of the PCB for wearable sensing was made of polyimide (PI) (Kapton®, DuPont, Switzerland). A poly(methyl metacrylate) (PMMA, IRPEN, S.A.) layer was attached to the substrate with ARclear 8932EE silicone-adhesive (Adhesives Research Inc., United States). To attach the Si chips to the substrate and protect the wire-bonding, various coatings with special properties were tested:

- Epoxy resin EPO TEK® H70-E2 (Epoxy Technology Inc., United States)
- Epoxy resin Delo-duopox® CR8021 (DELO Industrial Adhesives, Germany)
- Silicone adhesive/coating Dowsil™ 3140 RTV (Dow Corning Corporation)

The pseudo-reference electrode encapsulated was coated by drop-casting a prepolymer mixture within a pressure-sensitive adhesive (PSA) (Henkel Adhesives) frame.

Subsequently, a fluidic structure was designed to drive the sweat to the sensors in the patch. Different materials were tested for the intended use:

- Standard filter papers (grades 1, 4 and 6, Whatman®, Cytiva, United Kingdom)
- Sterile medical gause pads (10 x 10 cm) (Medicomp)
- 0.5 mm-thick polyethylene/polypropylene (PE/PP) and a 0.6 mm thick polyethylene (PE) hydrophilic flat sheets (the materials were kindly provided by Porex Filtration Group Corporation)

PMMA structures were fabricated to ensure intimate contact of the fluidic channel with the sensors. They incorporated polydimethylsiloxane (PDMS) joints, prepared with a mixture of silicone elastomer and curing agent (SYLGARDTM 184, Dow Corning). Furthermore, neodymium magnets (Supermagnete, Germany) were attached in one of the PMMA structures.

3.4. EQUIPMENT

3.4.1. Multi-ISFET meter

The potentiometric measurements were performed with a portable homemade multi-ISFET meter fabricated at the IMB-CNM [77]. The size of the equipment is 21 cm x 10 cm x 3 cm and records simultaneously the potential from six ISFET channels. The ISFET measurement was carried out by applying 100 μA and 0.5 V between the drain and the source and recording the ISFET gate potential (in mV). The visualization of the results and their treatment was carried out using a laptop connected by USB to the multi-ISFET meter and by employing a virtual instrument programmed with LabView 2013 (National Instruments, Austin, USA). The whole set-up is illustrated in Figure 3.2.

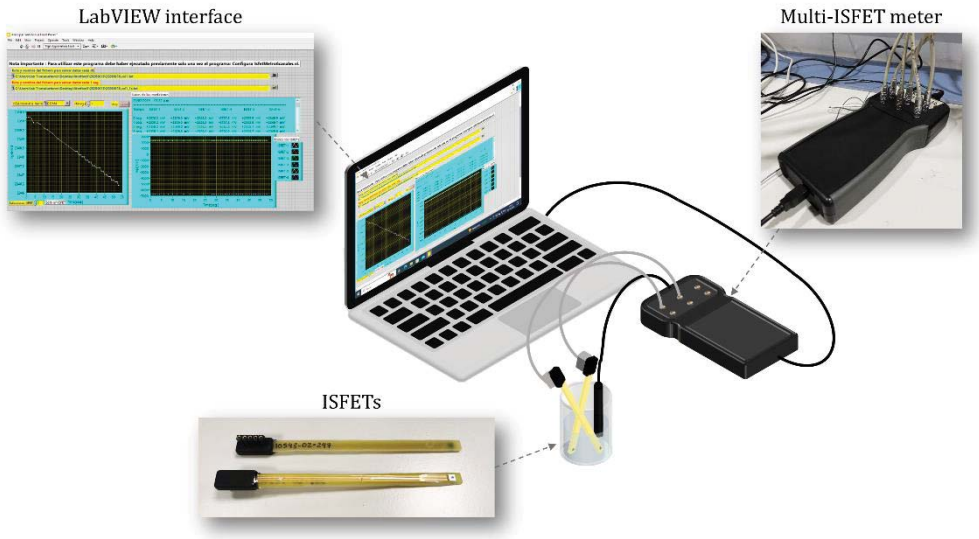

Figure 3.2. Scheme of the measurement system.

3.4.2. Virtual ISFET meter

The electrical characteristics of the ISFETs were obtained with a virtual ISFET meter that consisted of a National Instrumentation (PXI-1031) board, that included a digital multimeter and data acquisition module, a shielded

connector block (National Instrumentation, SCB-68), and LabVIEW software. This equipment was developed for the internal use at the laboratory of IMB-CNM.

3.4.3. Commercial ion-selective electrodes

The pH of calibration solutions was adjusted using a benchtop pHmeter (pH & Ion-Meter GLP 22+, Crison).

Commercial ISEs for Na^+, K^+ and pH (LAQUAtwin Na-11, K-11 and pH-11, HORIBA Advanced Techno Co., Ltd., Kyoto, Japan) were used for the comparative analysis of sweat samples (Figure 3.3), as explained in Chapters 5 and 7. To carry out the measurements, the electrode reservoir had to be filled with 300 µL of the sample and the sensor response took just a few seconds. The accuracy of the devices is ±100 ppm (±5 mM) for Na-11, ±10 ppm (±0.25 mM) for K-11 and ±0.1 for pH-11.

Figure 3.3. Picture of Na^+, K^+ and pH commercial ISEs.

3.4.4. Potentionstat-galvanostat

Electrochemical measurements were carried out at room temperature using an Autolab potentiostat/galvanostat, model PGSTAT30 (Eco Chemie, Utrecht, The Netherlands). The equipment was connected to a computer via

an Autolab USB interface and controlled using NOVA 2.1 software package for all measurements. A two-electrode electrochemical cell arrangement using an Ag/AgCl commercial RE and the device as working electrode (WE) was used to perform open-circuit potential (OCP) measurement. A three-electrode electrochemical cell using a platinum commercial counter electrode to the above configuration was used to carry out measurements by cyclic voltammetry (CV) and chronoamperometry.

3.4.5. Custom-made multi-channel readout electronics

A multi-channel readout electronic system, depicted in Figure 3.4, was produced to be implemented with the wearable device (Chapter 6). It was designed and fabricated by the Integrated Circuits and Systems Group (ICAS) group at the IMB-CNM within the WeCare project. This had a size smaller than a credit card (6 × 4 cm) and works in the desired constant I_{DS}-V_{DS} operation mode. It incorporated an analogue multiplexer to connect each ISFET sensor to the common microcontroller unit in charge of both the analogue-to-digital data conversion and the USB data communications. In this way, the wearable system could be read and configured from a wide variety of commercial portable devices, like smartphones, tablets or laptops. The resulting plug-and-play hardware was completed with a Scientific Python software interface. This is thoroughly described elsewhere [78].

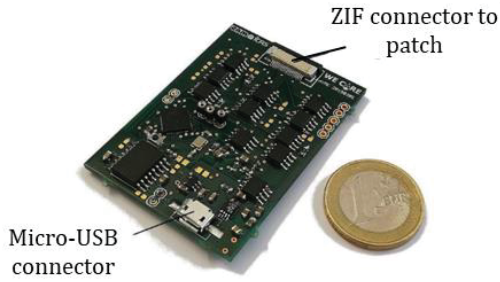

Figure 3.4. Picture of the multi-channel PCB implementation.

3.4.6. Other materials and equipment

Different Ag/AgCl commercial REs have been used for the electrochemical measurements. They are listed here below:

- An Orion 90–02–00 double junction Ag/AgCl RE (Thermo Fisher Scientific Inc., Waltham, MA, USA) with 3 M KNO_3 solution in its outer chamber to test the sensors in batch.
- An Ag/AgCl/10% (w/v) KNO_3 RE (Metrohm 0726 100, Herisau, Switzerland) to test the sensors in batch.
- A Dri-Ref RE of 5 mm diameter (World Precision Instruments, Sarasota, Florida, USA) in tests with the flow system.
- A Dri-Ref RE of 2 mm diameter (World Precision Instruments, Sarasota, Florida, USA) in tests with the patch and for cortisol measurements.

As counter electrodes (CE) for the amperometric measurements, the following devices were employed:

- A Pt wire for patch's characterization tests.
- A Pt sheet electrode from Metrohm for the solid-state RE evaluation in strip.

Other equipment:

- UV curing flood lamp with radiation of 225 mW cm^{-2} at the wavelength of 365 nm (Dymax Corporation, United States)
- Optical stereo microscope (M80, Leica Microsystems GmbH, Germany)
- Confocal microscope (Sensofar PLμ2300, Spain)
- Olympus IX81 inverted microscope with 10x magnification lens. Images from the microscope were recorded with a Hamamatsu Orca Flash 4.0 camera. Equipment installed in the Microscopy Service of the faculty of Sciences at the Autonomous University of Barcelona (UAB)

- Digital material dispensing equipment (DMD100™ deposition system, Kelenn Tech., France)
- Peristaltic pump (Miniplus 3, Gilson, United States)
- Syringe pump Nemesys (CETONI GmbH, Germany)
- CO_2-laser cut system (Epilog Mini 24, Epilog Laser, United States)
- Ion chromatograph (IC) (940 Professional IC Vario, Metrohm, Switzerland) installed in the faculty of Geosciences and Environment at the University of Lausanne (UNIL) (Switzerland)

4 DEVELOPMENT AND CHARACTERIZATION OF PH, NA+, K+ AND CL- ISFETS

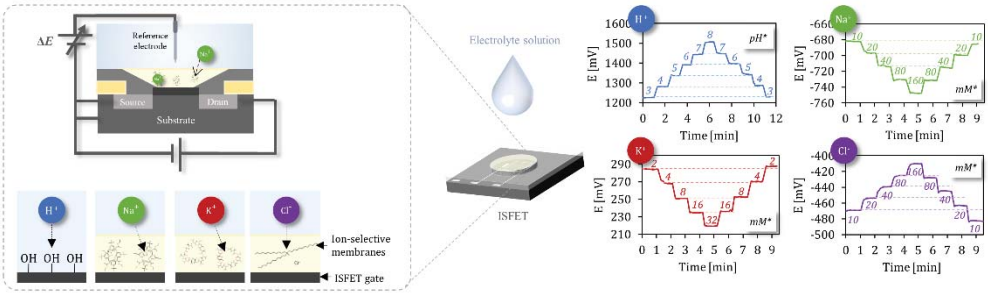

Figure 4.1. Graphical abstract illustrating the detection mechanisms and the reversible Nernstian responses of pH, Na+, K+ and Cl- ISFETs.

4.1. INTRODUCTION

4.1.1. ISFET's selectivity modification

ISFETs can be chemically modified with polymeric membranes in order to detect and quantify ions in a solution. Ionophores selective to the specific ion are trapped in the membrane and, when in contact with a solution, they interact with the target ion, resulting in a change in the electrical properties of the ISFET. This change is transduced into an electrical signal that can be measured and analysed.

The functionalization of the ISFET depends on the functional groups present in the transducer surface and in the polymeric membrane. The ISFETs employed had Si_3N_4 dielectric at the gate. The membrane's matrix polymer used for Na+, K+ and Cl- ISFETs was an aliphatic urethane diacrylate oligomer, which has been widely used in this type of sensor [59,68,79,80]. In

order to bind both parts, the gate's surface must be treated to promote the homogeneous formation of hydroxyl groups and then silanized. O_2 plasma treatment has been extensively reported to treat these surfaces [81], however, the encapsulation layer hinders its use. Chemical treatments can be used instead [69], as long as they don't require high temperatures (>100°C) or use acetone, which would damage the encapsulation layer. Oxydising and basic conditions can be applied to the gate, to promote the SiO^- groups.

Then, 3-(trimethoxysilyl)propyl methacrylate is commonly used as a silane coupling agent to functionalize surfaces [62,73,82]. Owing to its three reactive alkoxy groups, stable bonds can be formed between the surfaces, leading to great adhesion strength [83]. These are hydrolyzed in aqueous environments or anhydrous organic solvents and form silanol groups (Si-OH) [84]. When applied to Si3N4 surfaces, silanol groups undergo condensation reaction with the hydroxylated surface via the hydrogen bond and form siloxane (Si-O-Si) linkages over the treated surface (reaction 1).

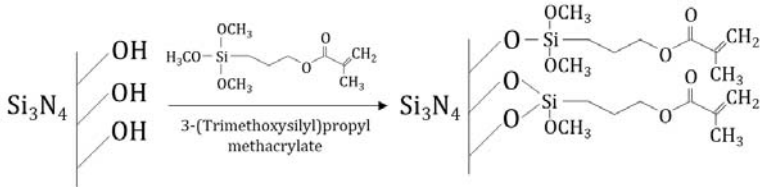

(1)

Then, the prepolymer mixture can be photochemically polymerized by UV-irradiation on top of the gate, following the well-known radical mechanism described in [85]. As result, the polymer is covalently bound to the substrate.

Among alkali metal cations, Na^+ and K^+ play key roles in the regulation of numerous biological processes. Consequently, extensive research efforts in the fields of analytical and biological chemistry have been dedicated to achieving precise differentiation between Na^+ and K^+. Nature produces a remarkable ionophore, valinomycin, which exhibits exceptional selectivity for K^+. In contrast, there is not a comparably effective ionophore in nature for

the selective recognition of Na^+ over K^+. This has prompted the synthesis of artificial ionophores designed for this purpose. Among these, calix(4)aryl esters have emerged as particularly prominent, owing to their rigid molecular structure that accommodates an ionophoric cavity perfectly suited to the size of Na^+. However, it is worth noting that the greater lyotropic properties of K^+ compared to Na^+ (following the Hofmeister series) can result in Na^+-selective electrodes exhibiting some degree of response to K^+ ions.

Special emphasis has been placed on the accuracy of Na^+ ISFET's determination, as the biomarker's concentration in sweat has been related to sweat rate whole body sweat Na+ concentration has been demonstrated to be highly dependent on the heat acclimatization status and the energy expenditure [28].

This Chapter studies the treatment of ISFET gate surfaces, a crucial step in affixing the selective membranes. It also shows the subsequent characterization of the selective ISFETs, specifically for the detection of Na^+, K^+, and Cl^- in both aqueous solutions and sweat samples. Additionally, recognizing the substantial significance of the Na^+ biomarker in the context of sports-related health concerns, supplementary characterization studies were conducted to achieve precise quantification.

4.2. EXPERIMENTAL SECTION

General materials and methods have been described in Chapter 3. Membrane modification of pH ISFETs and analytical characterization of the resulting sensor devices are described below. The assessment of the devices intended for the monitoring of biomarkers required the application of several methodologies including visual inspection, as well as thorough electrical and electrochemical characterization. All the potentiometric measurements were performed with the portable homemade multi-ISFET meter described in section 3.4.1.

4.2.1. Polymeric membranes

The ISFET gate is modified with a membrane to make it sensitive to different analytes, in such a way that the potential change is exclusively due to the presence of the selected target analyte. Thus, ISFETs sensitive to Na^+, K^+ and Cl^- ions were produced by modifying the pH ISFET gate with membranes mainly comprising a polymer matrix entrapping ionophore selective recognition molecules. The composition of the membranes and the deposition methodology have been described in section 3.2.

Before the silanization and deposition, ISFET's gate can be activated to be a better grafting surface. Different procedures were applied to the ISFET's gate to achieve the best membrane adhesion: without hydration step, hydrating them in H_2O_2 3% solution for 2.5h [82] and treating them with HF 5% for 10 s and immersion in NaOH 2.5% for 30 min.

4.2.2. Visual inspection

First of all, an inspection of the devices was carried out with the optical stereo microscope to ensure the absence of defects on the ISFET chip pre-encapsulation layer. Then, chips were encapsulated as described in section 3.2 and membranes selective to each ion were deposited.

The membranes were examined with the optical stereo microscope. Some of the critical points that could affect sensor performance were:

- *Ionophores precipitation*: in the absence of solvent or other necessary components, leading to a notable alteration in the membrane's appearance from transparent to opaque. This transformation typically results in a reduction in the sensitivity of the sensor.
- *Air bubble presence*: air bubbles may be formed during the drop-casting of the prepolymer mixture. When the membrane

undergoes curing, these bubbles can introduce charges, potentially leading to signal instability.

- *Detachment or scratch*: if the cured membranes are unable to withstand mechanical stress resulting from excessive curing, inadequate adhesion, or an inadequate amount of prepolymer mixture, they may become detached from the ISFET gate or fractured.

4.2.3. Electrical characterization

Packaged ISFETs were electrically assessed by applying gate-source potentials (V_{GS}) in a range of from -1.5 to 0.3 V with a 0.05 V step and recording the drain-source current (I_{DS}) to get the I_{DS}- V_{GS} curve. These studies were carried out by means of a virtual instrument programmed with a LabView 2013 (National Instruments, Austin, USA). From the I_{DS}- V_{GS} curves, the threshold voltage (V_{TH}), the transconductance (G_M), and gate leakage current (I_{off}) parameters were extracted. The potential between drain and source (V_{DS}) was fixed at 0.5 V, according to previous works of our group [86].

The V_{TH} is the gate voltage required to create a conducting channel between the source and drain. This parameter depends on the geometry of the gate and the dielectric properties and reflects the bias condition of the transistor. It could be calculated by the straight-line extrapolation of the I_{DS}-V_{GS} curve at its maximum slope to the x-axis. The G_M represents the variation of I_{DS} with respect to the variation in V_{GS} applied to the ISFET. It is mathematically expressed as:

$$G_M = \partial I_{DS} / \partial V_{GS}$$

It depends on the sensor geometry and it is typically measured by Siemens (S) or Amperes per Volt (A/V). The parameter of interest is the G_M max, which is the highest slope value of the I_{DS}- V_{GS} curve and represents the device's sensitivity.

The I_{off} is the current passing through the gate when the channel has not yet been formed, and it should be close to 0. It was calculated as the I_{DS} current measured at V_{GS} = -1.5 V.

4.2.4. Electrochemical characterization

ISFETs packaged on the PCB strips were analytically assessed in aqueous solutions. The potentiometric measurements were performed with a portable homemade multi-ISFET meter fabricated at the IMB-CNM [77] using an Orion 90–02–00 double junction Ag/AgCl reference electrode. ISFETs measurements were carried out by applying a 100 μA current and 0.5 V V_{DS} and recording the ISFET gate potential (in mV). The visualization of the results and their treatment was carried out using a laptop connected by USB to the multi-ISFET meter or by employing the virtual instrument mentioned above. The ISFET performance was evaluated by applying the Nernst equation (defined in section 1.5) to the potentials recorded in stock solutions of varying target analyte concentrations or activities. The ionic activities of the calibration solutions were calculated following Debye-Hückel's equation considering all the ionic species present in the media.

The experimental methodologies used to characterize each parameter of the ISFETs' performance are described below.

Polymeric membranes were deposited on 15 ISFETs to evaluate the membranes' adhesion to the transducer. For this, just the Na^+ membrane formulation was used. Sensors were calibrated 15 times for 27 days. During this period, some of them were stored in dry while others were kept immersed in a 10^{-3} M NaCl solution.

To determine the response characteristics of Na^+, K^+ and Cl^- ISFETs, calibrations were performed by adding certain volumes of 10^{-4}, 10^{-2}, 10^{-1}, and 1 M NaCl and KCl standard solutions to 50 mL of deionized water every 1.5 minutes under stirring conditions. Parameters including sensitivity (slope

extracted from the adjustment to the Nernstian equation), linear range and LOD were determined. The studied concentration range was from 10^{-7} M to 1 M for all of them. pH ISFETs were calibrated in a range from pH 2 to 12 by adding diluted NaOH to a universal buffer solution, whose composition is described in Section 3.1.

The hysteresis effect of the different ISFETs was evaluated with a double calibration by first increasing and then decreasing the measured analyte concentrations. Five separate solutions containing 10, 20, 40, 80, and 160 mM NaCl or KCl were used for recording the Na^+ and K^+ ISFET calibration curves. Universal buffer solutions of pH 3 to 8 were used for the pH ISFETs. The sensors were successively changed from one solution to another every 60 seconds.

The temporal drifts of Na^+, K^+ and Cl^- ISFETs were evaluated by recording their potential for 1 hour by sensor immersion in low-concentration solutions under stirring conditions. 10 mM NaCl, 2 mM KCl and 5 mM NaCl solutions were used, respectively. For the pH sensor, a pH 7 buffer solution was used.

The evaluation of each ISFET's selectivity against the various components found in sweat involved the preparation of multiple solutions. These solutions contained a constant concentration of the target ion together with the usual concentrations of potential interfering species that could be found in sweat. The sensors were initially immersed in a solution where only the target analyte was present, followed by sequential immersions in solutions containing the interfering species for 1 minute. Finally, they were immersed in a solution where no potential interferents were present but containing a different concentration of the target analyte to assess their sensitivity.

The next test was focused on the sensor performance in an artificial sweat solution and in limiting the presence of target analyte concentrations to those commonly present in sweat, that is, 4-8 pH, 10-160 mM Na^+, 2-30 mM K^+, and 10-160 mM Cl^-.

Additional tests were performed on Na^+ ISFETs that included: minimum step change determination, sensor repeatability and reproducibility, pH influence, matrix effects of different sweat components as well as sensor lifetime and working stability. The minimum step change in concentration that could be differentiated from noise was determined by adding increasing amounts of 0.1 and 1 M NaCl stock solutions to DI water under stirring, to get Na^+ concentrations ranging from 0.01 mM to 10 mM. Repeatability and reproducibility values were obtained by performing triplicate calibrations in batch with five different sensors in DI water solutions containing Na^+ concentrations ranging from 10 to 160 mM NaCl.

The influence of the solution pH on the Na^+ ISFET response was tested by immersing the four sensors in five solutions containing 10 mM NaCl at pH 4, 5, 6, 7, and 8, with the pH adjusted with TRIS and HCl stock solutions. The sensors were sequentially immersed in solutions from higher to lower pH and measurements were repeated three times. The selectivity of the Na^+ sensor over K^+ was additionally assessed by changing the concentration of the target ion in the solution while maintaining a constant concentration of the interfering ion, following the methodological approach known as the Fixed Interference Method. To examine the potential interference of K+ ions on the Na^+ ISFET response in sweat, the sensor was calibrated by adding the required amounts of a NaCl stock solution into solutions containing 1 mM and 32 mM KCl, which are the minimum and maximum concentrations of K^+ in sweat. The limits of detection determined in each calibration established the minimum analyte concentration that could be detected in the presence of the interfering ion. These values were employed to calculate the selectivity coefficient ($K_{Na,K}^{pot}$) of the sensor. Finally, ten Na^+ ISFETs were calibrated in the presence of chemical species present in sweat that belonged to different families as defined in Table 3.1**¡Error! No se encuentra el origen de la referencia.**. A DI water solution and five solutions containing each family of

chemical species were prepared and sensors were calibrated in batch in five solutions with NaCl concentrations ranging from 10 to 160 mM.

The sensor lifetime and working stability were studied by performing 15 calibrations with four sensor units for over a month period in artificial sweat solutions. The range of concentrations was from 20 to 160 mM Na^+, with a resolution of 0.05 pNa. Aliquots of 1 M NaCl stock solution were added every two minutes in the artificial sweat solution initially containing 1 mM Na^+ under stirring.

4.3. RESULTS AND DISCUSSION

This section shows the most relevant results obtained in the fabrication and characterization of the ISFET devices described above.

4.3.1. Na^+, K^+ and Cl^- ISFET sensor development

4.3.1.1. *ISFET gate activation*

In this thesis, a new method for the deposition of selective membranes on Si_3N_4 gate ISFETs was developed. The optimal functionalization of the gate prior to the membrane deposition and the sensor storage conditions were shown to be key to producing a sensor with excellent analytical performance for our particular application. Different activation treatments of the ISFET gate and storage conditions were evaluated by studying the analytical performance of the sensors after membrane deposition.

During the test, 15 Na^+ ISFETs were divided into three groups. One group did not receive any treatment, the second one underwent H_2O_2 treatment, and the third one was subjected to HF + NaOH treatment, before the membrane deposition. Within each group, two ISFETs were immersed in a 10^{-3}M NaCl solution while stored in between calibrations, while the remaining three were stored in dry conditions. The sensors were periodically calibrated for 27 days, and the mean sensitivity values were recorded and shown in the graph bar in Figure 4.2a. These ranged from 52.3 to 54.3 mV

dec-1 and from 57.3 to 58.0 mV dec-1 when stored in solution and dry, respectively. These values reveal the lack of influence of the ISFET gate initial treatment on the ISFET sensor sensitivity, considering that the calibration slope varied within a narrow range of ±1.05 mV dec^{-1} in solution and ±0.35 mV dec^{-1} in dry conditions.

Regarding the storage conditions, the sensors stored in dry exhibited consistent and reliable performance throughout the test. They also demonstrated good reproducibility and repeatability. By contrast, those stored in solution displayed poorer sensitivities, marked by significant variations among sensors and over time. This sensitivity loss can be attributed to the gradual leaching of ionophores into the solution, despite their hydrophobic nature. A closer examination of sensitivity values for the sensors stored in solution revealed that two of the untreated sensors and one that underwent H_2O_2 treatment exhibited a sudden loss of sensitivity in the last calibrations carried out with them, as depicted in Figure 4.2b. Upon visual inspection, it was found that the sensor membranes were broken. Thus, the solution appeared to have penetrated the ISFET gate, resulting in recorded potential values that depended not only on the analyte-ionophore interaction inside the membrane but also on the solution. In Figure 4.2c the difference between an intact membrane and a broken one is exemplified. It is evident that the damaged membranes did not withstand the mechanical stress induced by the solution, as their adhesion to the gate surface was weak, with most of them remaining attached primarily along the perimeter of the well defined by the encapsulation process. By contrast, those treated with HF and NaOH displayed a similar appearance to their initial state, indicating a stronger adhesion. As a conclusion, the HF and NaOH treatment was selected to manufacture the sensors. HF treatment would remove the native oxide layer of the ISFET gate, exposing the Si_3N_4 layer/ SiNxOy beneath it. Subsequent immersion of the sensors in an alkali solution (NaOH) would cause the hydrolyzed oxynitride to undergo deprotonation and generate a

sub-monolayer of deprotonated Si-O- groups that are very active to covalently attach the organosilane component of the membrane to the gate surface by a hydrolysis and condensation robust sol-gel reaction [87].

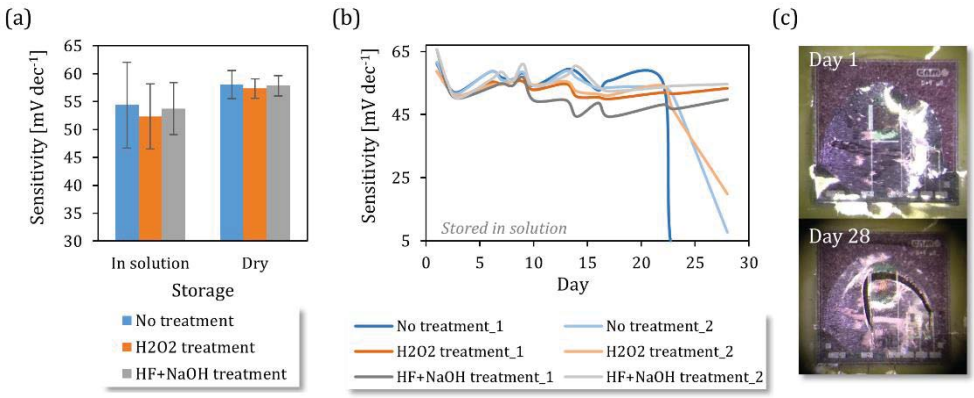

Figure 4.2. (a) ISFET's average sensitivities and their standard deviation during one month of testing, classified depending on the treatment suffered and the storage conditions. (b) Sensitivities of the ISFETs stored in wet conditions during almost one month. (c) Appearance of a membrane in good conditions (*Day 1*) and once broken (*Day 28*).

4.3.1.2. *Electrical characterization*

Before and after the gate's activation treatment, the sensors electrical parameters including the V_{TH}, the G_M max and the I_{off}, were calculated from the I_{DS}-V_{GS} curves of three devices, in order to assess the device's correct performance before membrane deposition. In Figure 4.3a, the curves recorded before activating the surfaces are represented as solid lines and the ones after the activation are depicted as dashed lines. This was the expected behaviour considering that the ISFET gate dielectric material got more conductive and its surface uniformly smoother.

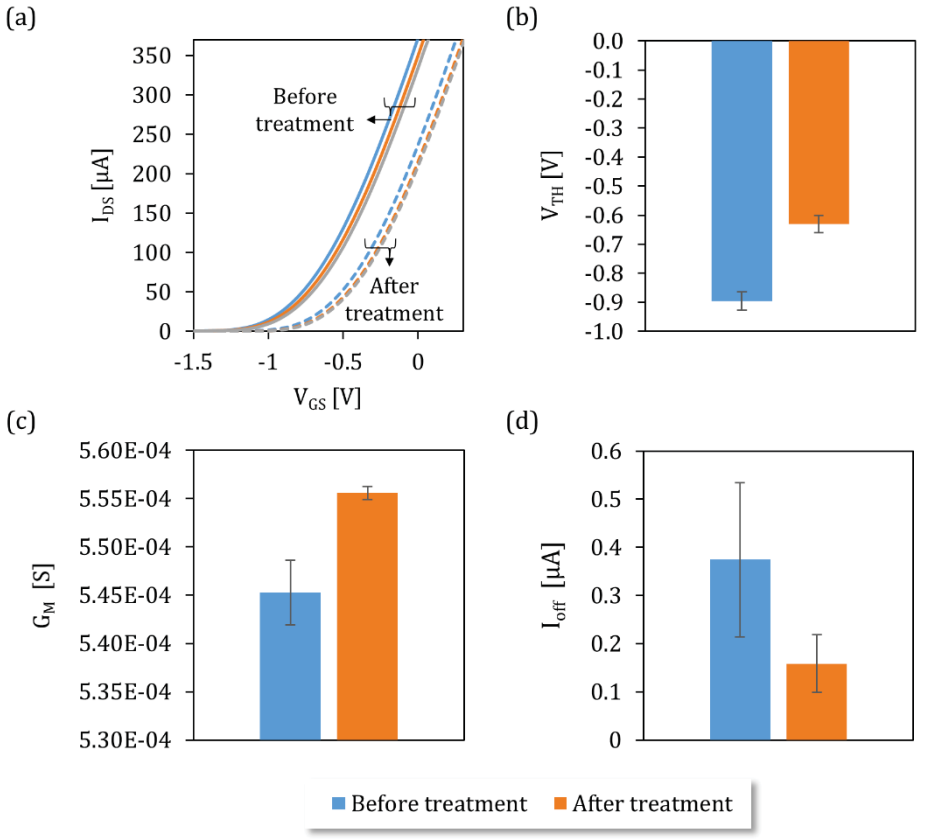

Figure 4.3. I_{DS}-V_{GS} curves of three ISFETs before *(solid lines)* and after *(dashed lines)* being treated with HF and NaOH, and the average V_{TH} (b), G_M (c), and I_{off} (d) values calculated from the curves. The error bars correspond to the standard deviation.

A shift in V_{TH} towards lower absolute values was clearly observed in the I_{DS}-V_{GS} curves of the three ISFETs (Figure 4.3a). It was quantified, as shown in Figure 4.3b, and the average displacement was +0.265 V. As the SiO_2 traces of the native layer were removed during the treatment and a homogeneous oxide layer was formed, the ISFET gate required lower potential differences to create the n-conductive channel. The average G_M max, which represents the device sensitivity, increased from 545.3 ± 3.3 µS to 555.6 ± 0.7 µS (Figure 4.3c). This means that after the treatment, a change in V_{GS} resulted in a larger change in I_{DS} at fixed V_{DS}, which allowed to detect smaller V_{GS} changes. All the measured parameters showed improved reproducibility after the treatment. Finally, the I_{off} revealed lower gate leakage after the treatment (Figure 4.3d).

Leakage currents are produced when there are imperfections in the dielectric layer, such as pin-holes or other irregularities, which were minimized while removing the oxide traces of the native SiO_2 layer from the gate surface.

4.3.2. Characterization of pH, Na^+, K^+ and Cl^- ISFETs in standard aqueous solutions

First, a complete characterization of individual sensors was carried out in a set of standard aqueous solutions containing the target analytes in a wide concentration range. As shown in Table 4.1, the sensors showed a nearly Nernstian response in a large range of concentrations covering the sweat's physiological ion content. The LODs were below the lowest ion sweat concentration (10^{-8} M for H^+ and 10^{-3} M for Na^+, K^+ and Cl^-), indicating that any change within their physiological range could be detected. All these values were in agreement with previous data reported for these sensors [66,88].

Table 4.1. Response characteristics of pH, Na^+, K^+, and Cl^- ISFETs in aqueous solutions.

Sensitive ion	Concentration range [M]	Sensitivity [mV dec^{-1}], N=3 (SD)	LOD [M], N=3 (SD)
H^+	pH 2 – 12	53.4 (2.5)	1.4×10^{-12} (5.3×10^{-13})
Na^+	10^{-5} – 10^{-1}	52.3 (2.1)	9.5×10^{-6} (4.5×10^{-6})
K^+	3×10^{-6} – 10^{-2}	54.3 (0.7)	2.1×10^{-6} (1.2×10^{-6})
Cl^-	10^{-5} – 10^{-1}	-60.7 (0.7)	9.4×10^{-6} (1.4×10^{-7})

The reversibility of the ISFET sensor response was assessed by studying the hysteresis of the voltage signal obtained when sequentially changing the target ion concentrations from low to high concentrations, and *vice versa*. The corresponding recordings are plotted in Figure 4.4a. The maximum potential variation observed for the same concentration was 5.6 mV for pH, 3.2 mV for Na^+, 3 mV for K^+, and 14.2 mV Cl^- ISFETs. These variations may be attributed to the sensor memory effects and temporal drifts. For pH, Na^+, and K^+ ions it

corresponded to a 5 – 10% of the sensor sensitivity and could be considered negligible. However, for Cl^- sensors, this variation was significant due to the slow Cl^- effusion rate from the membrane, as previously reported [89]. For all the sensors, the response time, representing the duration required to attain 95% of the stable potential, was less than 5 seconds.

The ISFETs V_{TH} temporal change, also known as drift, was determined in solutions containing low analyte concentrations. The average ISFET drifts were estimated to be 5.50 ± 2.83, -7.76 ± 0.15, -8.81 ± 0.13, and -10.52 ± 4.98 mV h^{-1}, for pH, Na^+, K^+, and Cl^-, respectively. From these values, it could be anticipated that the presented sensors are suitable for performing continuous measurements during a mid-term exercise practice. Another feature that may affect the sensor working stability is the well-known leaching effect of the ionophores from the polymeric membranes. In order to assess it, sensors for each target ion were stored between calibrations in their corresponding conditioning solutions for a month. Results indicated that the sensors lost less than 5% of their original sensitivity.

To identify sweat compounds that could affect the accuracy of the detection, potential interferents were added to different solutions containing a fixed concentration of the target ion. The ISFETs were immersed in the solutions containing relevant sweat compounds, and also in solutions with a different concentration of the target ion to check the sensor sensitivity to it. The recordings of the test are plotted in Figure 4.4b. The potential of Na^+, K^+ and Cl^- ISFETs in the prepared solutions differed a maximum of 2.5, 5.7, and 2.6 mV, respectively, from the solution containing only the target analyte. Considering that their sensitivity to Na^+, K^+, and Cl^- resulted in 60.0, 65.1, and -42.2 mV dec^{-1}, the variation would correspond to less than 10% of the measured concentration. The pH ISFET was evaluated by comparing the recorded potential to the expected one considering the 54.4 mV pH^{-1} sensitivity. The maximum difference was 9.0 mV. According to the results, the changes in the potential output caused by the interfering substances were

much smaller than those produced by the target analytes, which indicated the high specificity of the sensors.

Once defined the linear range of the ISFETs and the feasibility of measuring the target analytes within the sweat range, an artificial sweat solution was used to carry out an initial analytical assessment for our particular application. Sensors were calibrated in a range that covered the average target analyte concentrations in sweat, as described above. As shown in Figure 4.4c, for pH, Na^+, K^+ and Cl^- ISFETs average sensitivities of 51.7 ± 0.8, 57.1 ± 2.4, 52.0 ± 1.6 and -47.5 ± 9.6 mV dec^{-1} (N=3) were obtained, respectively, showing comparable performances in artificial sweat and in aqueous solutions. The low standard deviations of the estimated sensitivity values indicate adequate reproducibility for pH, Na^+, and K^+ ISFETs. For Cl^- ISFETs the reproducibility was lower. Also, the linear range for Cl^- ISFET was shorter due to the more accused matrix effect on the sensor signal.

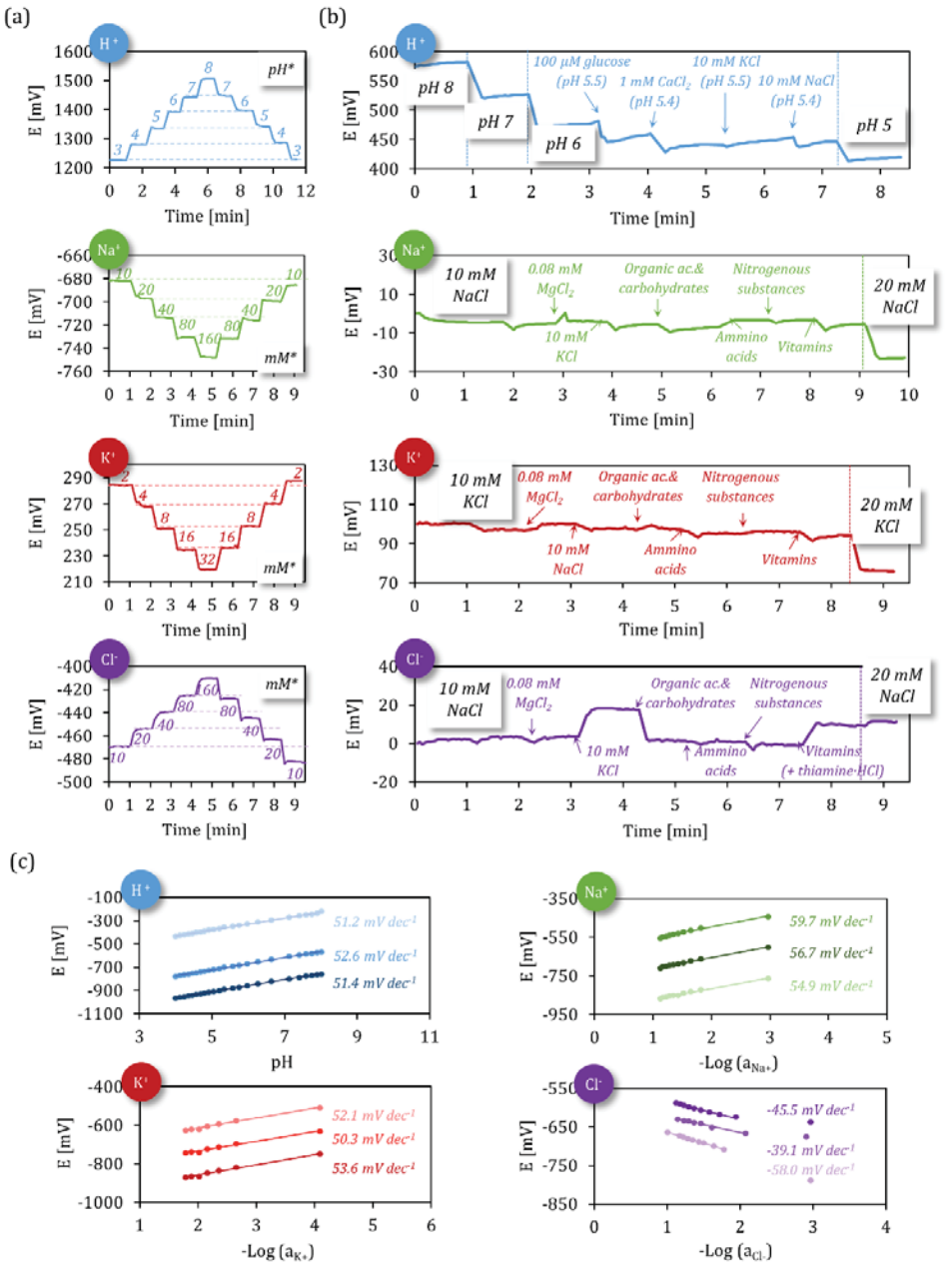

Figure 4.4. Characterization of ISFET sensors. (a) Recording of hysteresis responses for pH, Na+, K+, and Cl- ISFETs in aqueous solutions. The values of the respective concentrations of the analytes are shown in mM. (b) Recording of pH, Na+, K+ and Cl- ISFETs adding possible interfering substances present in human sweat. Data recording was temporarily paused for each change of solution. (c) Calibration curves of pH, Na+, K+, and Cl- ISFETs in artificial sweat solutions.

4.3.2.1. In-depth study of the Na^+ ISFET performance in sweat

Sodium has been extensively demonstrated to be one of the most relevant biomarkers in sweat. Consequently, we aimed to ensure that the Na^+ analysis with our sensor was as accurate as possible.

The minimum step change in concentration that could be differentiated from noise was determined by measurements in solutions of increasing Na^+ concentration ranging from 0.01 mM to 10 mM. From the results, depicted in Figure 4.5a, it was concluded that differences up to Δ1 mM, corresponding to 1.07 mV, could be quantitatively detected.

The repeatability for the same ISFET sensor was quantified. For that, five ISFETs were immersed in a water solution whose Na^+ concentration was increased from 10 mM to 160 mM. Sensors were calibrated three times. In Figure 4.5b these calibration curves are depicted. Although the repeatability was high for each ISFET, considering the mean values + the standard deviation of the sensitivity and intercept of 2.3 ± 1.0 mV dec^{-1} and 3.1 ± 1.3 mV, for the three recorded calibration curves, results were better for the second and third calibration replicates, which provided values of the mean sensitivity and intercept values + the corresponding standard deviation of 0.6 ± 0.5 mV dec^{-1} and 0.6 ± 0.4 mV, respectively. This indicated that the sensor required an initial conditioning step before being calibrated.

In the same study, the reproducibility among different sensors was assessed. The mean sensitivity value obtained for the five ISFETs tested was 60.7 ± 0.5 mV dec^{-1}, estimated using the values of the third calibration. The mean value of the intercept was -797.4 ± 74.7 mV. This value is indicative of the ISFET Vth and it is within the technological parameters already defined for these devices [88,90]. In previous works using Na^+ ISFET sensors for sweat analysis, values ranging from 55 to 62 mV dec^{-1} were found [29,50–52]. However, a full analytical characterization of the devices was not carried out since operational parameters presented like LOD, minimum concentration change detectable, working stability, etc. were neglected.

From our experiments, it could be concluded that the developed Na^+ ISFET sensors showed reproducible Nernstian responses in the Na^+ physiological concentration range in sweat.

A study was performed to evaluate the sensor lifetime and working stability. For that, four ISFETs were periodically calibrated in artificial sweat solutions over a period of more than one month (Figure 4.5c and Figure 4.5d). As it has been extensively reported [91,92], the conditioning step before the use of ion-selective potentiometric devices was critical. At first, the ISFETs were stored dry, and they were just conditioned in a 1 mM NaCl solution for 30 minutes before the first calibration. Apparently, it was not enough time since lower sensitivities were obtained on the first day (Figure 4.5c). The maximum sensitivity could have been achieved being immersed for at least 1h in the NaCl solution, before use. For subsequent calibrations, they were stored in a 1 mM NaCl solution to ensure a stable and reproducible sensitivity value. Excluding the first-day calibration, the standard deviation of the mean sensitivity values between days was 4.1 ± 1.8 mV dec^{-1}. The intercept of the calibration curves showed a similar trend for all ISFETs (Figure 4.5d). Until the thirtieth day, the intercept steadily increased day after day. Later, it got stabilized and then it decreased again. However, the variation of the intercept estimated considering the 15 consecutive calibrations was 35.8 ± 9.2 mV on average, which was in accordance with the sensor temporal drift previously reported [93].

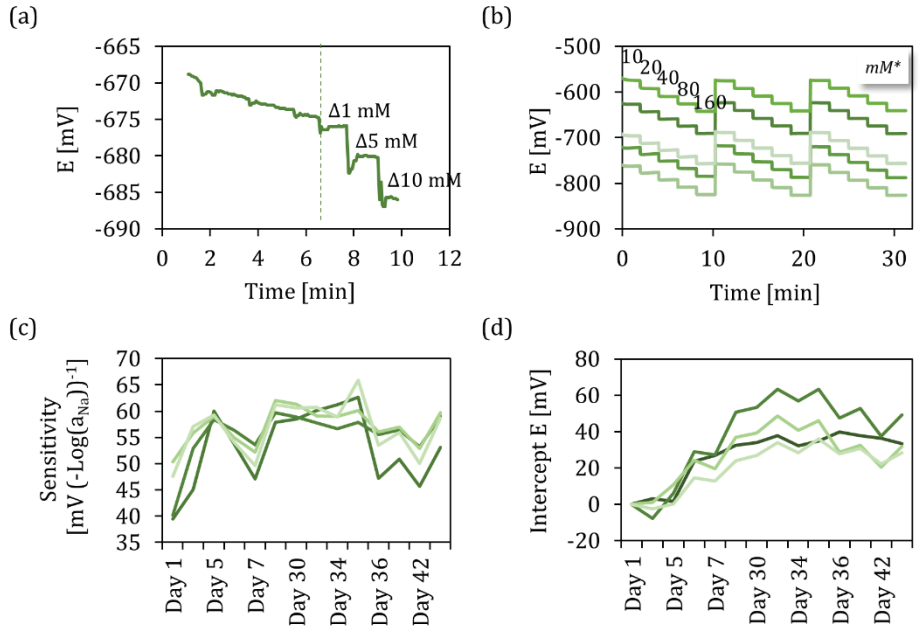

Figure 4.5. (a) Recording of the potential changes when adding increasing volumes of NaCl standard solutions. The dashed line indicates the minimum step change that can be detected with Nernstian slope. (b) Recordings of three consecutive calibrations at five concentration steps to study repeatability and reproducibility. Sensitivity (c) and intercept potential (d) of four ISFETs calibrated periodically during a period of 43 days.

This study allowed the development of an end-to-end prediction neural network to avoid individual sensor calibrations [94], mentioned as Publication 7. On the dataset obtained from these calibrations, the end-to-end prediction network developed by our partners at the Institute of Neuroinformatics (University of Zürich and ETH Zürich) could predict the Na^+ concentration with a root-mean-square errors (RMSE) of 20.7 mM, close to the 15.0 mM RMSE that would be achieved if a sensor calibration curve of the first day was applied to the recordings got with the same sensor during the following days (intra-sensor calibration). Compared to other conventional low-workload calibration methods, the prediction network greatly improved prediction accuracy. An example and a comparison with other methods RMSEs are shown in Figure 4.6a and Figure 4.6b, respectively.

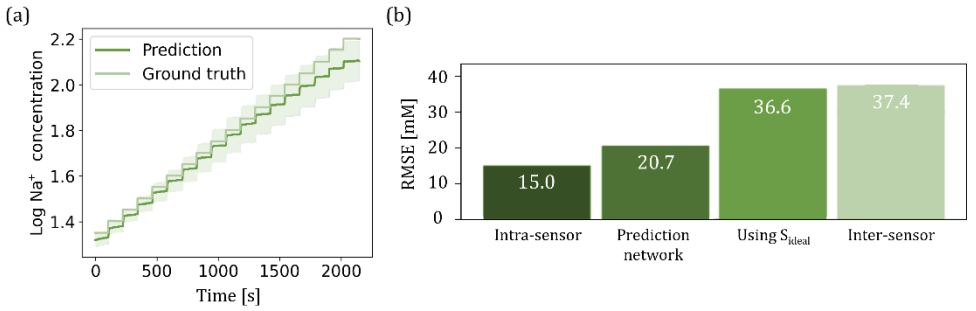

Figure 4.6. (a) Example of a Na^+ concentration prediction (*dark green*) from the prediction network and the corresponding ground truth (*light green*). The prediction consists of the expected prediction (*solid curve*) and the standard deviation (*shaded region*). (b) RMSEs for Na^+ concentration prediction using the baseline methods and our end-to-end prediction network,

Although the ionophore X is selective to Na^+, K^+ ions can also fit into its cavity and, therefore, the sensor gives some degree of response to its concentration changes (Figure 4.7a). For this reason, the selectivity of Na^+ ISFETs to K^+ was assessed. It was evaluated by means of the fixed interference method. For that, the response of five Na^+ ISFETs was recorded under increasing concentrations of the primary ion (Na^+), and in a fixed concentration interfering ion (K^+). From these recordings, the $K_{Na,K}^{pot}$, which defines the ability of the sensor to distinguish Na^+ from K^+, was extracted. The smaller the value of $K_{Na,K}^{pot}$ the greater the sensor's preference for Na^+. In Figure 4.7b, three calibration curves are depicted: a calibration in deionized water and two in solutions with fixed KCl concentrations. The average $K_{Na,K}^{pot}$ in a 1 mM KCl solution was 0.0899 ± 0.0065, whereas in a 32 mM KCl solution, it was 0.0492 ± 0.0029. The results demonstrate a significant interference from K^+ ions affecting the response of Na^+ ISFETs, especially at concentrations of potassium exceeding 1 mM. However, considering the 10X higher concentration of Na^+ over K^+ in sweat this interference is expected to have minimal impact on the measurement of Na^+ ion concentrations. The average value of 0.0695 derived from both $K_{Na,K}^{pot}$ was kept for further evaluation in real sweat solutions. This assessment aims to determine

whether the inclusion of this contribution would enhance the precision of the Na^+ concentration determination.

The pH effect on the sensor was evaluated. The potential recorded from the ISFETs in solutions containing 10 mM NaCl at the physiological range of 4 to 8 pH units remained almost constant (Figure 4.7c). The standard deviation of the potential values recorded with the four ISFETs was between 0.8 – 3.5 mV.

An extensive test of the sweat matrix effects on the ISFET response was performed by calibrating ten sensors simultaneously in six background solutions containing different families of components present in sweat (Table 3.1). Figure 4.7d shows the results. The sensitivity to Na^+ in the different solutions was compared with the one in water using the paired samples t-test (α=0.05). The values obtained in the different solutions were not statistically comparable to the ones in water, except for the organic acids and carbohydrates (t_{calc} 0.77 < t_{tab} 2.26). Thus, the last was the only group not included in the artificial sweat solution used in the following studies.

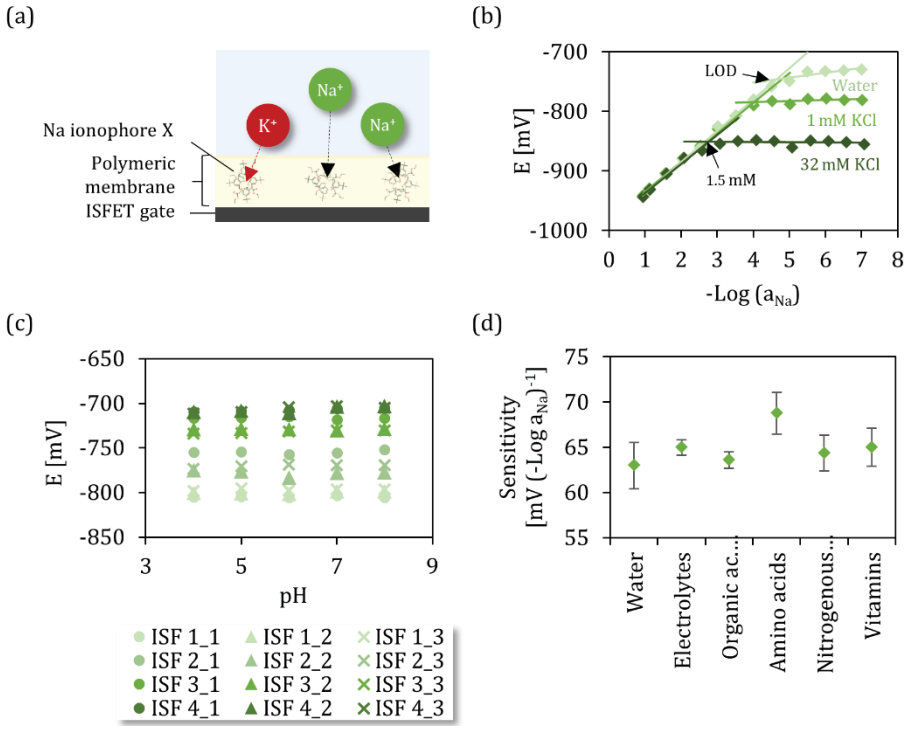

Figure 4.7. (a) Scheme of interactions between Na^+ and K^+ ions with the Na^+ ionophore X in the selective membrane. (b) Responses of a Na^+ ISFET in deionized water and 1 mM and 32 mM KCl solutions. (c) Output potential values recorded with four ISFETs in five solutions with fixed concentrations of NaCl and different pH (4-8) in triplicate. (d) Sensitivity of five Na^+ ISFETs to NaCl changes in different matrices.

4.4. Conclusions

The fabrication of potentiometric ISFET devices for the pH, Na+, K+ and Cl- sensing used throughout this thesis work was carried out and all the characteristics of their performance were evaluated. The sensors exhibited consistent, Nernstian, reversible, repeatable, and reproducible responses in long-term use in standard electrolyte solutions. Their cross-selectivity was assessed, and results drove to conclude that artificial sweat solutions would be used for its calibration prior to sweat analysis. All the characteristics assessed led us to foresee the sensors' potential for sweat analysis.

The fabrication and characterization of pH, Na^+, K^+ and Cl^- ISFETs served also to develop an electronic tongue for beverage classification, described in Publication 3. Furthermore, the exhaustive analytical assessment of the Na+ ISFET in standard solutions was published in Publication 5.

5 Analytical Validation of pH, Na^+, K^+ and Cl^- ISFET Sensors in Sweat Samples

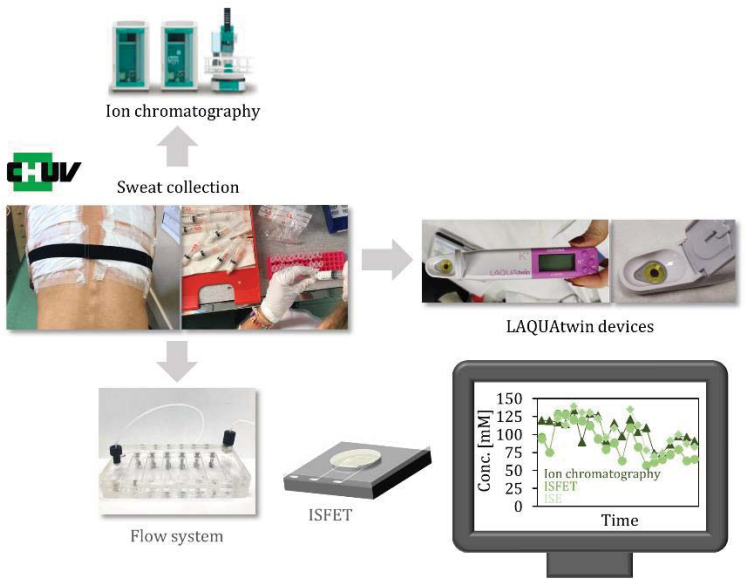

Figure 5. 1. Graphical abstract of the steps involved in the sweat samples collection and analysis with reference methods (IC and commercial ISEs) and with ISFETs under flow conditions.

5.1. Introduction

The following chapter encompasses the fabrication of a fluidic setup for low volume sample analysis and the findings from the analytical validation of pH, Na^+, K^+, and Cl^- ISFET sensors in sweat samples under flow conditions.

The validation of ISFETs measurements required the sweat samples analysis with reference techniques. The use of this biofluid for health assessment is still under research, Therefore few studies have reported sweat analysis using gold-standard analytical methods such as ion-chromatography or inductively coupled plasma mass spectrometry (ICP-MS) [26,95]. The disponibility of such bulky and expensive instrumentation and the acquisition of sufficiently large sweat volumes for sampling purposes present challenges in sweat determination with standard methods. To proceed with our devices validation, the methodologies for sample collection and analytical techniques used were based on a work reported by Baker et al. in [26], in which sweat's Na^+ and K^+ determination using ion chromatography and commercial LAQUAtwin ion-selective electrodes (ISEs) was compared.

A standardised regional absorbent patch technique was used to collect the sweat [96]. Its advantages included the considerable amount of sweat that can be collected and the possible use in any part of the body. However, we must ensure skin cleaning and patch isolation to avoid contamination and evaporation of the sweat secreted.

The results obtained through this analytical validation shed light on the sensors' capabilities in real-time continuous sweat analysis.

5.2. EXPERIMENTAL SECTION

Reagents and solutions used have been described in Chapter 3. The potentiometric measurements were performed with the portable homemade multi-ISFET meter described in Section 3.4.1.

5.2.1. Set-up for analysis in under flow conditions

A fluidic architecture was used for carrying out sweat sample analysis with the developed ISFET sensors. PMMA pieces were designed using CorelDraw Graphics Suite 2018 software and manufactured by rapid prototyping using a CO_2-laser cut system. The design and the different parts that conformed the cell are depicted in Figure 5.2a. The fluidic assembly comprised three 110 mm x 60 mm PMMA layers of different thickness. The different layers with the required pattern were firmly attached by intercalating PSA films. The fluidic set-up was designed to easily implement pH, Na^+, K^+ and Cl^- ISFET sensors together with a 5 mm-diameter Dri-Ref RE. Two additional channels were included for potential simultaneous monitoring of other sensors if needed. A linear 500 μm-wide channel, containing six wells that were aligned with the ISFETs gates, was defined. The inner volume of the flow cell was 160 μL. This is the sum of the channel volume, from inlet to outlet, and the volume required to fill the ISFET and the RE reservoirs. An extra well was defined just after the channel inlet to host the RE. Commercial O-rings were used in the fluidic cell where the sensors were inserted, and consequently, as demonstrated in Figure 5.2b with a red dyed solution flow, fluid leakage was prevented. External tubing and a peristaltic pump were used to drive the solutions inside the channel. The assembly is depicted in Figure 5.2c.

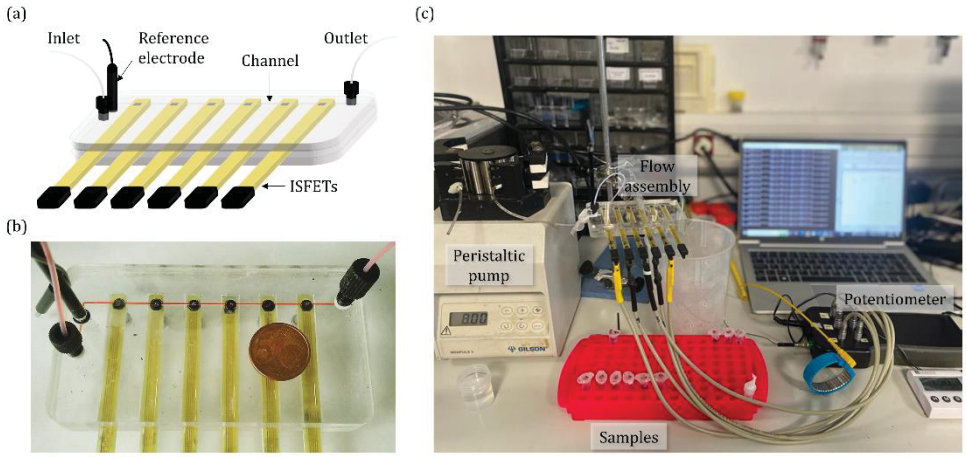

Figure 5.2. Set-up for sweat samples analysis in the flow system. (a) Illustration of the PMMA flow assembly for ISFET's sweat analysis. (b) Picture of the flow assembly when a dyed solution was pumped through six ISFET. (c) Picture of the whole set-up for sweat samples analysis with ISFETs in the flow system.

5.2.2. Sweat sample collection for ISFETs validation

Sweat samples were collected from a subject during four indoor cycling sessions scheduled in different days at the *Swiss Olympic Medical Center* of the Lausanne University Hospital (CHUV). Each session was divided into 3 phases with different effort levels, each one lasting 20 min. The sessions were part of a study approved in September, the 13th, 2019 by the Ethical Commission of the Canton of Vaud, Switzerland (Protocol No. 2019_01235), and therefore they were performed in accordance with the ethical standards laid down in the 1964 Declaration of Helsinki. The subject was fully informed of the nature and risks of the study, and was free to withdraw at any stage of the study.

The sweat samples collection methodology applied was based on the syringe method described by Baker et al. [26]. Medical gauzes were used to collect the sweat directly from the skin of the subject's upper chest. Gauzes were covered with PET films to avoid evaporation and removed after each phase in order to extract the sweat from the gauze using a syringe. The sweat samples had a volume of 600 µl, on average. Each sweat sample was divided

into two equal aliquots, one analysed by the ion chromatography (IC) reference method at CHUV laboratories and the other one to be sent to our institute and analysed with our set-up and the LAQUAtwin commercial ISEs. Samples were stored in sealed tubes at -20°C until use. The different steps performed for the sample collection are represented in the pictures in Figure 5.3**¡Error! No se encuentra el origen de la referencia.**.

Figure 5.3. Images from sweat sample collection.

5.2.3. Sweat sample analysis

Sweat samples were systematically injected into the flow platform, following a predefined sequence. Firstly, samples were pumped for 120 seconds and measurements were carried out. Next, a 15-second air flow, followed by a 30-second water flow was applied to clean the channel. Finally, another 15-second air flow was applied. This sequential procedure was implemented to ensure that no sample dilution by the intercalated cleaning step took place and thus consistent and controlled conditions during the experimental measurements were applied.

Sensors were previously calibrated in the artificial sweat solutions within the range of analyte concentrations, mentioned in Section 3.1. The ion concentration and pH determined using ISFETs in the sweat samples were compared with the ones obtained by IC and LAQUAtwin commercial ISEs.

For ISFETs validation and commercial ISEs characterization, IC was selected as the gold standard method. Bland-Altman plots [97] were used to estimate the limits of agreement, which were computed as the mean difference of the values obtained by the two methods ± 1.96 times the standard deviation. This was the interval in which 95% of measurement differences were expected to fall. Data points lying outside these limits of agreement were excluded. Then, to express the accuracy of both the commercial ISE and ISFET sensor analytical data, the correlation between the obtained results with both approaches and the IC reference method was studied using scatter plots. If the results were not statistically different at a set level of significance, linear regressions comparing both methods should yield a straight line showing a slope and intercept close to one and zero, respectively. CIs have been calculated to evaluate the data dispersion and sample size. It serves as a powerful tool for summarizing data, providing insight into the likely true value and the proximity of the measured data to that value.

5.3. RESULTS AND DISCUSSION

5.3.1. Flow system evaluation

The flow system performance, described in section 5.2.1, was optimized to ensure that no chemical or electrical interferences among the integrated sensors occurred in order to prevent any errors or bias in the quantification of the different target analytes. The initial step involved determining the optimal flow rate. For that, a Na^+ ISFET integrated in the flow cell was used to record variations in the potential signals recorded when different calibration solutions were pumped at 0.3, 0.5 and 0.8 mL min^{-1} flow rates. The recorded signals were evaluated considering the time for signal stabilization, the sensitivity to NaCl concentration changes, and the linearity within the studied concentration range. The recordings are illustrated in

Figure 5.4a. Remarkably, no significant differences were observed in the detection time and signal stability at the flow rates studied. However, the sensor exhibited the highest sensitivity (59.0 mV dec^{-1}) and the coefficient of determination R^2 >0.9999 when working at 0.5 mL min^{-1}. Then, this flow rate was selected for all the further studies.

Then, the signal stabilization or baseline was studied by injecting artificial sweat solutions. Figure 5.4b shows that the baseline achieved for the first replicate was different to that of the following ones, which stabilized at similar potential values. This behaviour was also observed in tests with real sweat samples. Moreover, it can be observed that the transient signal appeared more pronounced for the first and second replicates. Then, the response reached a stable value in just a few seconds. These results indicate that the membrane needed some time for conditioning in the sample and that the observed temporal drift of -0.085 mV min^{-1} was then considered to be negligible.

Finally, the sample renewal and sensor cleaning were evaluated by studying the reversibility of the signal. An artificial sweat solution spiked with 1 mM NaCl was pumped before and after carrying out three calibration solutions and analysing five sweat samples (Figure 5.4b). The potential recorded in the mentioned solution was -728.9 ± 1.2 mV, demonstrating the excellent sensor response reversibility.

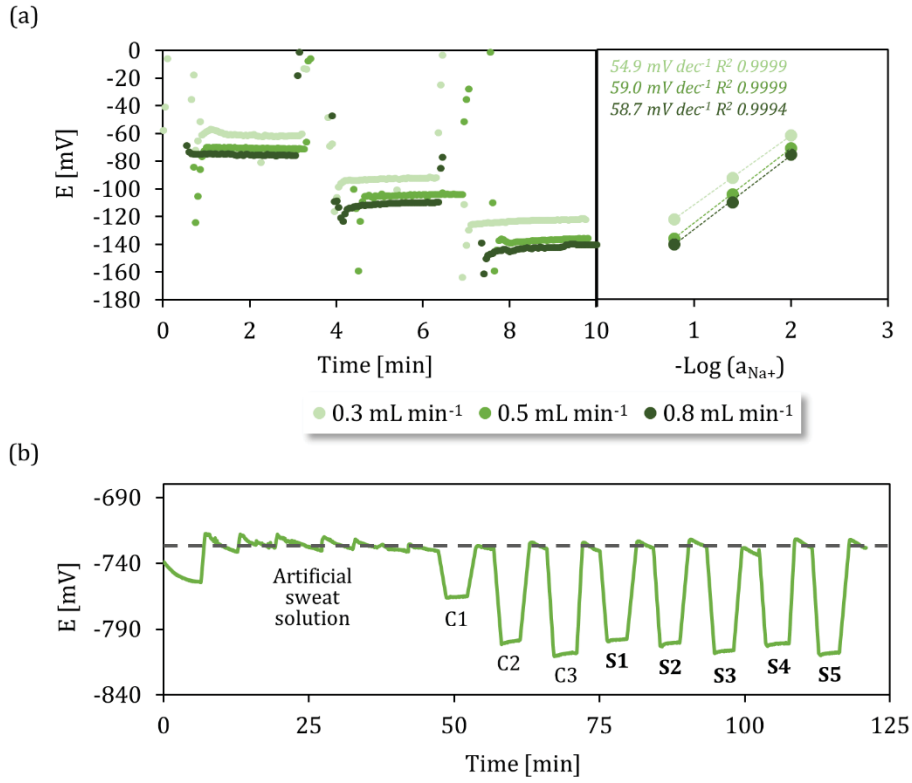

Figure 5.4. (a) Recording of the output signal of Na^+ ISFET when injecting three calibration solutions and the calibration curves obtained. (b) Recording of the output signal of Na^+ ISFET for repetitive additions of artificial sweat solution to study the stabilization time and subsequent injection of three calibration solutions and five sweat samples.

5.3.2. Sweat samples analysis

pH, Na^+, K^+ and Cl^- ISFETs were calibrated in artificial sweat solutions under flow conditions (Figure 5.5a). Subsequently, low volume sweat samples (~ 300 µL), obtained as described in section 5.2.2 and previously analysed by IC, were injected in our system to record the sensor response to the different target analytes. In parallel, the same sweat samples were analysed with the commercial LAQUAtwin ISEs. Values obtained with these sensors were in parts per million (ppm) and were converted into mM concentrations for comparative purposes.

It should be noted that the highly ionic content of the samples would contribute to a high ionic force, and thus, to deviations in the activity coefficients from the Debye-Hückel's equation from the ideal $\gamma_{+-}=1$. As detailed in section 3.1, our approach meticulously aimed to formulate a solution closely resembling the ionic content of sweat. Then, although the activity coefficient of sweat samples was unknown, our calibration procedure allowed us to generate calibration curves without needing to convert concentrations to activities and apply them directly to the potential measurements in sweat samples. From the interpolation, concentration values were obtained and they could be directly compared with the concentrations determined using IC and ISEs methods. Additionally, for Na^+ ISFETs determination the concentrations were calculated using both Nernst and Nikolsky-Eisenman to consider the K^+ ion contribution to the sensor signal.

Figure 5.5b displays the pH and concentration values obtained for each target analyte with each analytical technique in the chronological order of measurement.. For pH determination, the ISFET values could only be compared to those of the ISEs. Also, Cl^- ISE sensors are not commercially available by HORIBA so that a comparative study for Cl^- analysis was not feasible. Regarding pH, Na^+ and K^+ concentration values, some similarities in the trends between the different techniques could be observed. Furthermore, it should be noted that the samples analysis was performed continuously for a period of more than two hours, and temporal drift potential contribution was not observed in pH, Na^+ and K^+ determination, being that one of the limitations of ISFETs sweat sensing. However, a more thorough analysis was necessary to draw meaningful conclusions. When analysing Cl^-, the Cl^- concentrations measured tend to increase in the order of the sample analysis, evidencing that there may be a cumulative effect of Cl^- ions in the ISFET membrane or the presence of an interfering anion in sweat. This behaviour is in contradiction with the trend observed in the Na^+ concentration values

measured. This phenomenon has been previously reported in the literature (Ref??).

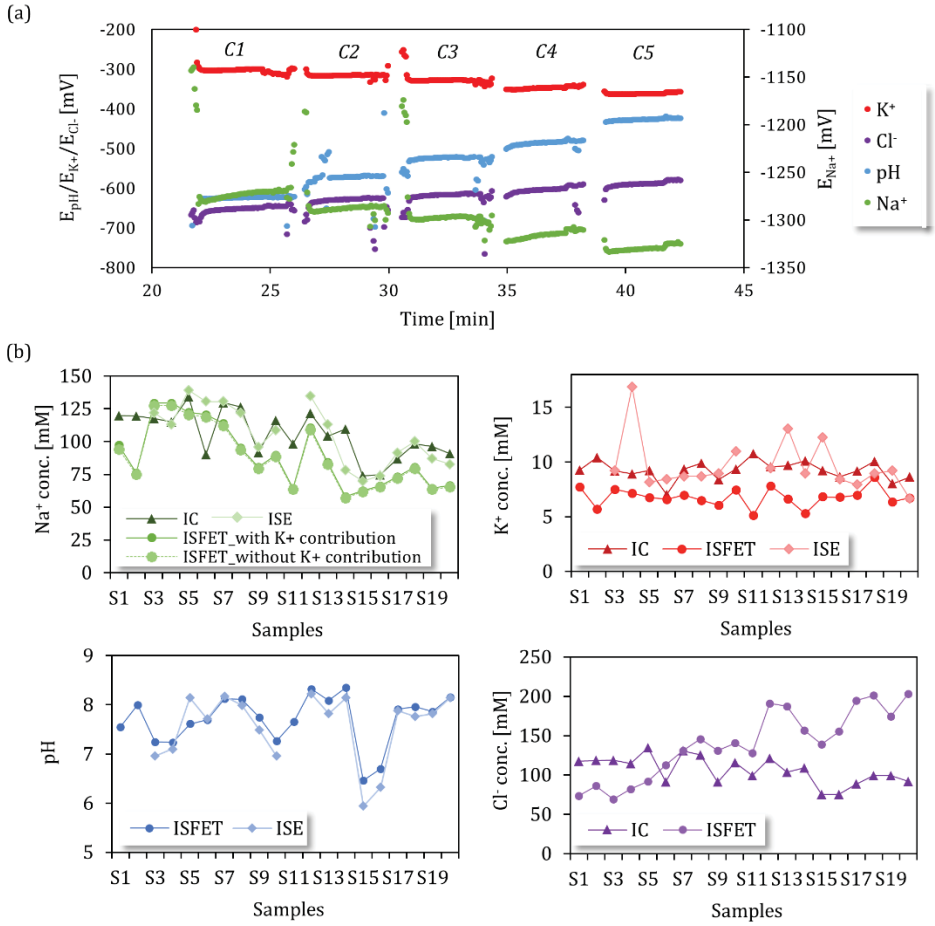

Figure 5.5. (a) Recording of the output signal of pH, Na^+, K^+, and Cl^- ISFETs during the calibration. (b) pH, Na^+, K^+, and Cl^- determination in 20 sweat samples using three different techniques: IC, commercial ISEs and ISFETs.

Bland-Altman plots were initially used to visualize the data of the sweat analysis and identify outliers [97]. These plots illustrated the relative differences in the analysis of each sample ISFETs, taking IC and commercial ISEs concentration values as references, plotted against the mean concentration obtained with the compared methods. An example of such plots is shown in Figure 5.6a, which displays the results of the Na^+ concentration values obtained with IC and Na^+ ISFET, considering the

influence of K^+ interference. Any data point lying outside the limits of agreement (LOA) at 95% confidence interval were excluded from the analysis. As an example, in Figure 5.6a sample S6 data was removed.

Following the exclusion of outliers, the refined dataset was represented in scatter plots to identify possible proportional and systematic measurement errors and assess the agreement between the methods. As explained in the Introduction, IC was used as the reference method for this analysis. Nevertheless, we also compared the ISFET determination with well-validated commercial ISE's, whose performance is close to our sensor devices, with the aim of evaluating the potential impact of the type of technique on the sweat target analyte detection.

For Na^+ determination, our initial objective was to assess the potential impact of K^+ interference on the accuracy of Na^+ concentration determination in sweat samples. We compared values obtained from the interpolation in the Nernst equation (without considering K^+ contribution) and in the Nikolsky-Eisenman equation (factoring in K^+ contribution, utilizing a $K_{Na,K}^{pot}$ of 0.0695). The relative error calculated without K^+ contribution was 1.34% larger than the one calculated with K^+ contribution. Consequently, Na^+ determination in sweat samples demonstrated greater accuracy when employing the Nikolsky-Eisenman equation, utilizing Na^+ concentration values derived from this calculation for subsequent evaluations. Na^+ sensing results are represented in Figure 5.6b. The linear regressions derived from comparing the concentrations obtained with the ISFET sensors with those of the IC and ISE methods revealed slopes near 1 and intercepts close to 0, thus demonstrating strong correlations between the different analytical approaches. Despite some dispersion in the values, the coefficients of determination remained consistently high, with $R^2 > 0.9$ in both comparisons. While the level of correlation with both methods appeared to be similar, there was a marginally better correlation observed with the ISE values, attributed to the inherent nature of the detection technique.

The assessment of the accuracy of analytical values obtained with the ISFET sensors revealed the presence of a systematic bias, as evidenced by CIs that did not include 0: 95% CI = -11.03 – -25.07% with respect to IC and 95% CI = -14.25 – -20.87% with respect to ISE. That resulted in average relative errors of -18.05% and -17.56%, respectively. The presence of this bias suggested a matrix effect that was not initially detected during the sensor characterization in artificial sweat. This effect might be attributed to the lipid-rich content present in the samples, which would affect the hydrophobic nature of the selective membrane [98–100]. These substances can permeate into the polymeric membranes, changing its properties, and reducing the sensitivity towards Na^+ ions.

The results of the analysis of K^+ is depicted in **¡Error! No se encuentra el origen de la referencia.**. In this case, the concentration values obtained were within such a narrow range that we could not validate the ISFETs performance by linear regression fitting. Despite this, as in Na^+ sensing, a systematic bias was evident when comparing the values to those obtained from IC and ISE methods, resulting in average relative errors of -24.57% and 20.76%, respectively. Given the systematic nature of the error observed for both Na^+ and K^+ target analytes, a correction of the bias would significantly improve the accuracy of their determination using our sensors.

pH ISFET detection was directly compared to that obtained with commercial ISE (Figure 5.6d). A strong correlation was observed, with a slope close to 1, an intercept close to 0, and a coefficient of determination of 0.936. It should be noted that our ISFETs did not require a selective membrane to detect pH changes, as the transducer was intrinsically sensitive to them, Therefore, the bias observed in Na^+ and K^+ sensing, probably caused by sweat matrix effects, as pointed out above, was not present in the pH measurements. This supported the theory that the interaction between lipidic compounds in sweat and the polymeric matrix could contribute to the systematic error found in the Na^+ and K^+ ISFET responses.

Finally, the data from Cl^- ISFET was represented in the scatter plot in Figure 5.6e. It became clear that the ISFET could not provide accurate measurements of Cl^- ion content. In light of these findings, the Cl^- ISFET sensor was excluded from the final selection of sensors to be integrated into the wearable patch.

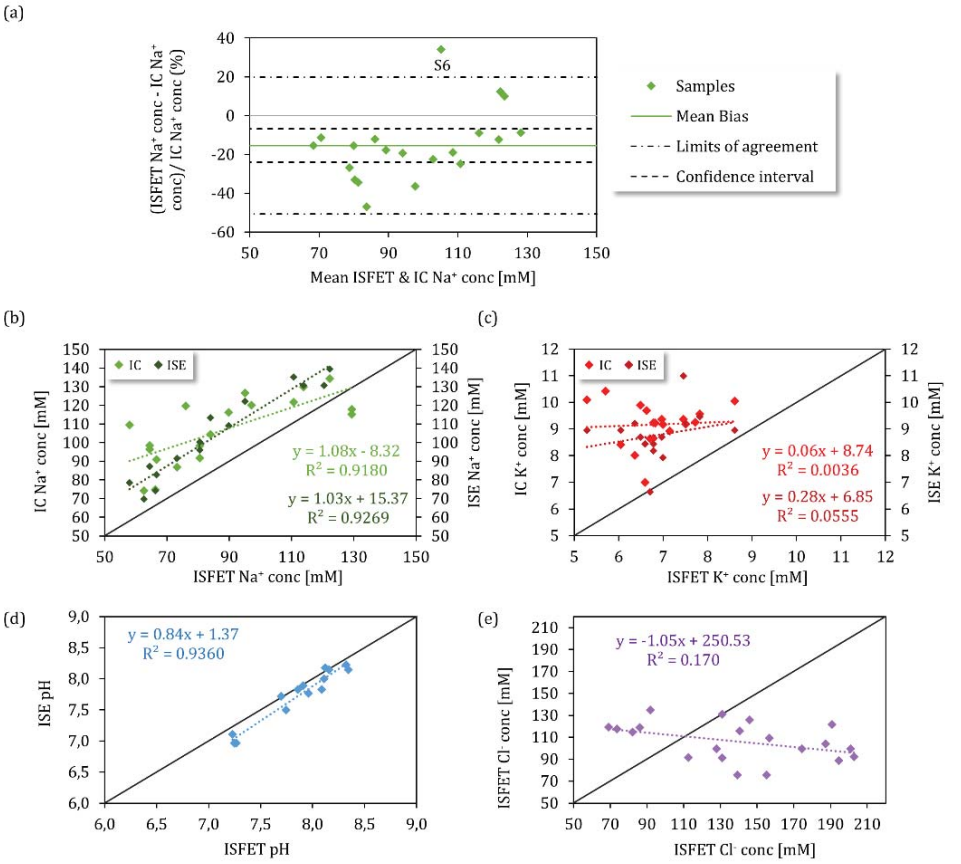

Figure 5.6. Scatter plots for showing the correlations between ISFETs, commercial ISEs and IC determination for (a) Na^+, (b) K^+. (c) pH and (d) Cl^-, following Pearson regression.

5.4. Conclusions

The performance of the previously developed and characterized pH, Na^+, K^+, and Cl^- ISFETs has been assessed in sweat samples under flow

conditions. ISFETs have been rarely tested in biofluids, probably due to their limitations regarding the integration into comfortable wearable platforms for continuous monitoring of ions. The continuous determination of ions in samples under flow revealed the potential of pH, Na^+, and K^+ ISFETs in the real-time continuous monitoring of biomarkers for long-periods of time, without being affected by temporal drift or degradation of the sensitivity. Conversely, Cl^- ISFET drift contribution prevented its accurate sensing, so the sensor was discarded for its integration in the patch, being its physiological information redundant when Na^+ concentration changes are monitored. Overall, the pH, Na^+ and K^+ biomarkers could be monitored in sweat samples, taking into account matrix effect contribution due to the ion-selective polymer nature, that is systematically present across the samples, and that could be corrected with machine learning algorithms.

Moreover, Na^+ ISFETs determination results in sweat samples under flow conditions were published in Publication 5**.**

6 DEVELOPMENT OF A PATCH-LIKE WEARABLE PLATFORM

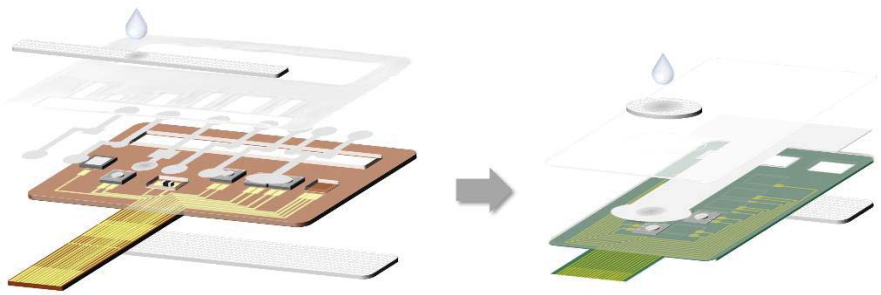

Figure 6.1. Graphical abstract illustrating all the elements integrated into the two versions of a path-like wearable platform for sweat monitoring.

6.1. INTRODUCTION

In this chapter, the development and characterization of the patch-like wearable platform is described. Since pH, Na^+ and K^+ ISFETs were validated in sweat samples, as it was described in Chapter 5, they were chosen to be incorporated into the wearable patch for sweat monitoring. Besides the previously mentioned ISFETs, a solid-state RE and a fluidic structure were integrated.

The fabrication of the patch elements and its validation under laboratory conditions are described hereinafter.

6.1.1. Solid-state reference electrode

The deployment of potentiometric devices such as ISEs or ISFETs in novel applications remains limited due to the lack of robust miniaturized reference electrodes. The traditional REs contain an internal reference solution that requires regular maintenance and a vertical working position [101,102]. Moreover, the potential leakage of the filling solution contaminates the samples. Therefore, the pursuit of a novel, reliable, stable and low-cost miniaturized reference electrode is imperative to enable the potentiometric measurement with ISEs and ISFETs.

Our first option was the development of a REFET. The miniaturization of reference electrodes has several limitations that would be skipped with the use of an ISFET, already miniaturized, modified in order to be insensitive to changes in the media. Hence, considerable effort has been devoted over the years to minimize the pH sensitivity of an ISFET to attain an ultimate sensitivity of zero, thereby achieving a perfect REFET. [40] Many attempts to develop a REFET have been carried out covering the ISFET's gate with a membrane insensitive to ions. The first publication of this method dates back to Matsuo, who applied a parylene film onto the Si_3N_4 gate of an ISFET [103]. Despite the reduction in pH sensitivity, the stability of the potential was not achieved, possibly attributed to the existence of pinholes within this extremely thin layer. As a result, alternative membranes, typically thicker layers, have been deposited in attempts to address this issue[104]. In this work, we choose polyHEMA-based hydrogels, as their capacity to eliminate the ISFET's pH sensitivity has already been reported [82,105].

The following option was the miniaturization of the conventional reference electrode. As mentioned before, it involves multiple considerations, including the reduction of all its components, including metals, salts, filling solutions, and interfaces. Aspects such as potential drift, liquid junction effects, and solution concentrations assume significance and

can potentially mask accurate results if not carefully controlled. Therefore, constructing such electrodes necessitates careful attention to several critical factors [106]:

1. High exchange current densities are essential for the reference electrodes, ensuring they are non-polarizable, meaning their potential is challenging to change.
2. The reproducibility of potentials across all electrodes is crucial.
3. Potential drift, caused by filling solution effusion or electrode coating degradation, needs to be minimized throughout the device's operational duration.

Several challenges arise during the process of miniaturization, with a significant issue being the rapid dissolution of small electrode volumes such as Ag/AgCl, resulting in relatively short lifetimes. The most usual fabrication techniques employed in the deposition of electroactive layers are thin-film deposition, electroplating, screen-printing, ink-jet printing, fluid dispensing, drop-casting, ion-exchange reaction and electrochemical coating. [107]

The final step in reference electrode design entails substituting the liquid reference solution chamber and its interface by employing alternative materials capable of performing similar functions. These materials encompass porous substances, gels, or membranes, serving to fulfil identical purposes in the electrode system. [107]

Among the different possible combinations, we focused on the use of an Ag/AgCl ink and a polymer membrane. The most common membranes are made of agar, PVB, polyvinyl chloride (PVC), and ionic-liquid-doped PVC [108]. Notably, PVB membranes have gained substantial traction in recent years, supported by several studies that have showcased their suitability in different substrates [29,46,109–111].

6.1.2. Capillary-based fluidic structure

The patch should integrate a fluidic structure designed to continuously deliver excreted sweat to the sensors on the platform in real time. Given the microliter-scale sample volume, employing microchannels and external components such as pumps and valves would be necessary. Instead, using materials that operate via capillary action, the design and optimization of a microfluidic structure would be more straightforward, since external pumping wouldn't be necessary. These materials, though potentially disposable, are easy to fabricate, and cost-effective.

In the following review [112], mentioned as Publication 2, we highlighted the main advantages and limitations associated with combining capillary-driven fluidics with solid-state sensors. Our analysis extensively examined approaches from the past decade in this field, shedding light on their effectiveness and scope.

6.2. Experimental Section

The designed patches for on-body sweat monitoring include pH, Na^+, and K^+ ISFETs, together with a temperature sensor. Additionally, the integration of a solid-state RE into the patch was essential for conducting potentiometric measurements. Initially, the development of a modified ISFET device non-sensitive to changes in the surrounding media (REFET), was explored for its role as the RE. This involved the deposition of a tailor-made hydrogel membrane on the gate ISFET that maintained the electrical properties of the device while eliminating its chemical responsiveness to pH. However, this approach was later discarded, and a solid-state Ag/AgCl RE coated with a PVB hydrogel membrane was developed on a Pt thin-film electrode chip to be integrated into the patch-like device. Details regarding the fabrication processes of both approaches are presented in this section.

Furthermore, this section provides comprehensive descriptions of several patch designs, fluidic structures, and assessment of different employed materials. The suitable analytical performance of the wearable patch incorporating all the previously mentioned components is eventually described.

6.2.1. Formulations of the hydrogels for the development of a REFET

To transform an ISFET device into a REFET, the development of a hydrogel exhibiting adequate wettability and conductivity was imperative. Polyhydroxyethyl methacrylate (polyHEMA) was selected due to its previous successful application in ISFETs, as documented in existing literature [105,113,114]. Prior studies indicated that, when utilized as an intermediate layer, polyHEMA did not compromise the performance of ISFETs and it effectively mitigated their sensitivity to pH changes. Additionally, the possibility of covalent anchoring of polyHEMA on the surface of the Si_3N_4 ISFET gate was already demonstrated [82]. The cocktail composition of the polyHEMA hydrogel is given in **¡Error! No se encuentra el origen de la referencia.**, and was selected based on previous reported formulations [82,115]. The monomer was firstly mixed with EG under stirring for 2 min. Then, EGDMA and DMPA were successively added also under stirring. The mixture was then homogenized in an ultrasonic bath for 15 min.

Table 1. Composition of the polyHEMA prepolymeric mixture.

Components	**Proportion (wt/wt %)**
HEMA	56
EG	38
EGDMA	5
DMPA	1

It was reported that the hydrogel viscosity was improved when 40% (w/w) of KCl solution was introduced following the mixing of the organic components, mentioned above, and that a 100 μm-thick coating ensured practically no response to pH [82]. As there could be potential leaching of the KCl from the hydrogel into the sample, an initial formulation was devised that replaced the electrolyte solution with a solution including other similar ions that would not interfere with the pH, Na^+, K^+ or Cl^- measurements. Thus, the first formulation prepared consisted of polyHEMA containing 40% (w/w) of a 0.1 M $Mg(NO_3)_2$ aqueous solution. Further formulations were evaluated where the electrolyte solution was substituted by polyelectrolytes, aiming to enhance the stability of the hydrogel while keeping its conductivity. Among the several existing polyelectrolytes, polyMETAC polycation, and polyAMPs polyanion, were selected. Both of them previously showed promising performances in the syntheses of conducting polymer gels [116,117]. The formulations tested and their respective proportions were as follows:

- Poly($HEMA_{80}$-co-$METAC_{20}$)
- Poly($HEMA_{60}$-co-$METAC_{20}$-co-$pAMPS_{20}$)
- Poly($HEMA_{70}$-co-$METAC_{15}$-co-$pAMPS_{15}$)
- Poly($HEMA_{80}$-co-$METAC_{10}$-co-$pAMPS_{10}$)

For the hydrogel deposition, the same methodology as in the production of the Cl^- ISFET sensor, described in section 3.2, was followed.

6.2.2. Fabrication of the integrated Ag/AgCl/PVB reference electrode

A 1 mm^2 Pt thin-film electrode defined on a 3x3.5 mm^2 silicon chip was employed as the base substrate for the manufacture of the integrated RE. A film of Ag/AgCl ink was deposited by digital material dispensing fully covering the Pt electrode surface area and then cured for 1 hour at 150°C. Figure 6.2a and Figure 6.2b illustrate the Ag/AgCl ink deposition and the final appearance of the pseudo-RE. The chips were encapsulated in the patch-like

substrate described below and a squared PSA frame was laser-cut and attached around the electrode (Figure 6.2c).

A PVB polymer solution was prepared, based on [109,110], by mixing 50.1 mg NaCl, previously dried in the oven and ground, and 79.12 mg PVB in 1 mL methanol, followed by sonication at 37 kHz for 30 minutes. Subsequently, a certain volume of PVB prepolymer solution was drop-casted within the frame area (Figure 6.2d). The process was repeated three times, leaving 1 hour between each step, to achieve a layer with an adequate thickness. Finally, it was left to dry for at least 12 hours in a chemical fume hood. The Ag/Ag/PVB RE final appearance is shown in Figure 6.2e. The electrode was conditioned in a 3M KCl solution overnight, before use.

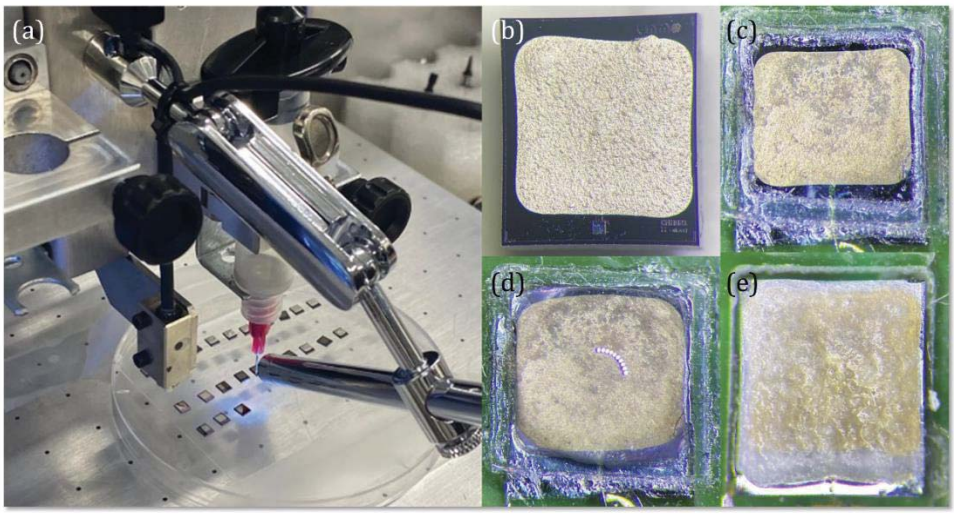

Figure 6.2. (a) Digital material dispensing process of an Ag/AgCl ink on top of the Pt thin-film electrodes. (b) Cured Ag/AgCl layer. (c) Ag/AgCl pseudo-reference electrode encapsulated in the patch with the PSA frame around. (d) Drop-casted prepolymer PVB mixture within the PSA frame and (e) final appearance of the RE once the PVB was polymerized.

6.2.3. Fabrication of the wearable patch

The patch-like platforms consisted of rectangular flexible PCBs fabricated on 0.1 mm-thick PI. The contact areas for fixing and wire bonding the different chips, the electrical tracks and the contact pads were defined. 18

µm-thick electrical copper tracks coated with a thin gold layer on the contacts and pads for wire-bonding, were inkjet-printed. The platforms were produced at the clean room facilities of the *École Polytechnique Fédérale* of Lausanne (EPFL, Neuchâtel, Switzerland). To easily align the chips on the flexible substrate, a 0.5 mm-thick PMMA layer having an ARclear 8932EE silicone adhesive on one face, was patterned by a CO_2-laser cutter and attached to the substrate.

Two designs were fabricated and tested. These designs shared similar dimensions but featured different sensor distributions across the platform. The first design measured 2.5 cm x 5 cm, with contact pads for a zero insertion force (ZIF) connector extending from the longer side, as depicted in Figure 6.3a. The second design measured 2.5 cm x 4.0 cm, and its contact pads were positioned on the shorter side (Figure 6.3b). The sweat evacuation area, which is exposed to the air, exhibited variations between the two designs. In the second design, this area incorporated three smaller windows as opposed to a single large one, primarily to enhance the stability and retention of the sink pad. Both platforms were designed to encapsulate a temperature sensor and pH, Na^+, and K^+ ISFETs. Parameters such as conductivity, lactate, and glucose sensors were initially considered to be integrated into the patch. Preliminary encouraging results were obtained during their development and testing. However, it was eventually decided to exclude them from further consideration, based on the finding that they did not appear to show a clear role or relevance as sweat biomarkers in the context of sports-related health issues.

The bare ISFETs (without selective membrane) and Pt thin-film electrode chips already containing the Ag/AgCl ink layer mentioned above, were fixed to the substrate using a specific glueing process and wire-bonded to the contact pads of the PI substrate. The temperature sensor was fixed to the substrate and connected to the pad with a conductive resin. Then, the wire-bondings and electrical tracks of the chips and substrate were coated to

isolate them from the environment. Different coatings were tested to find the best one in terms of water resistance, adhesion and stiffness, once cured. The main limitation when used for our purposes was the curation temperature, which should be below 80°C to avoid damaging the materials used to fabricate the patch and also the pre-encapsulation layer of the ISFETs. The coatings tested were epoxy resin EPO TEK® H70-E2, epoxy resin Delo-duopox® CR8021, and silicone coating Dowsil™ 3140 RTV.

Figure 6.3c illustrates a wire-bonded chip on the wearable platform and the appearance of the cured coatings.

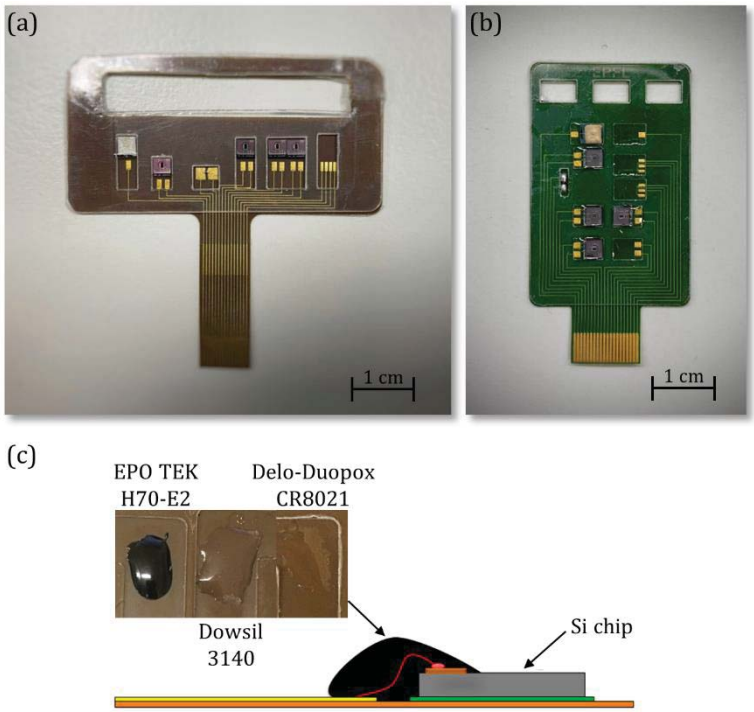

Figure 6.3. Images of the first (a) and second (b) designs of the patch-like platforms intended for wearable applications. (c) Cross-section view of an encapsulated chip in the wearable platform and the different coatings studied.

The fluidic component is a critical element of the wearable patch. Its purpose is to ensure an efficient and uniform capillarity flow of sweat from the collection area to the sensor surface, and ending at the sink pad. In this work, we opted for fibre-based materials because of their ease of patterning,

efficient wicking capability, and rapid flow rates, among other benefits described in section 6.1.2. The fluidic components were patterned with a CO_2-laser cutter. A variety of materials were evaluated with this purpose: Whatman® standard filter papers (grades 1, 4 and 6, corresponding to 0.180, 0.205, and 0.180 mm-thick, respectively), sterile medical gauze pads, and 0.5 mm-thick PE/PP and 0.6 mm-thick PE hydrophilic flat sheets.

During the evaluation of the fluidic performance of some materials, the application of a fixed pressure onto the fluidics became necessary to ensure close contact between the fluidic component and the sensors. To address this, two types of PMMA structures were fabricated. Both structures comprised two PMMA layers sandwiching the patch. One design utilized two PMMA clamps on either side (Figure 6.4a), while the other one integrated neodymium disk magnets to keep the different layers tightly together (Figure 6.4b). All PMMA components were patterned using a CO_2-laser system. Additionally, a PDMS gasket was implemented around the sweat collection pad to prevent any leakage. To fabricate the gasket, PMMA moulds of varying thicknesses were designed in order to choose the gasket with the appropriate thickness to get a leakage-free collection pad area. A mixture of silicone elastomer and curing agent in a 10:1 ratio was prepared. Air bubbles introduced during mixing were eliminated by placing the solution in a vacuum desiccator. Subsequently, the mixture was poured into the moulds and cured on a hot plate at 80°C for 30 minutes.

Finally, an ARcare 90445 double-sided medical-grade adhesive was used to tightly fix the microfluidic components to the PCB substrate and ensure efficient compatible adhesion of the wearable patch to the skin.

A cross-section scheme in Figure 6.4c displays the different layers of the wearable platform in contact with the skin. The ARcare 90445 double-sided adhesive ensured that sweat secreted beneath the collection pad could be absorbed without any seepage. Once the collection pad reached saturation, the sweat would be drawn through the fluidic channel positioned over the

sensors via capillary action. Finally, it would reach the sink pad, designed made of a material with a high absorption capacity and open to the air to facilitate sweat evaporation.

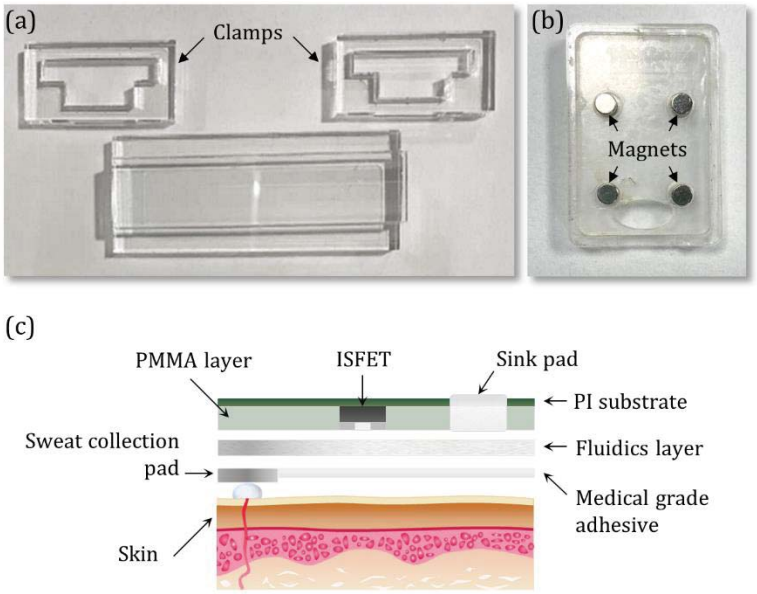

Figure 6.4. Pictures of the PMMA structures designed to apply a uniform pressure over the fluidics, using clamps (a) and disk magnets (b). (c) Cross-section diagram of the layers comprising the structure of the patch when placed on the skin

6.2.4. Evaluation of the patch performance

The individual characterization of the different ISFET sensors was already described in Chapter 4. Here, we focus on the characterization of quality parameters for REFET and the Ag/AgCl/PVB RE developed for carrying out robust potentiometric measurements with the sensors once integrated into the patch-like device. This characterization included the verification of the correct encapsulation of the chips onto the flexible PCB, the evaluation of the connection and signal stability provided by the newly developed in-house

readout electronics (described in section 3.4.5), and the assessment of the material fluidic properties and fluidic design structure.

The REFET and the Ag/AgCl/PVB RE were individually encapsulated in PCB strips to facilitate these studies. The final selected electrode was integrated into the patch and further characterized by drop-coating and eventually using the capillary-driven fluidic set-up. Both experimental set-ups are represented in Figure 6.5a and Figure 6.5b, respectively.

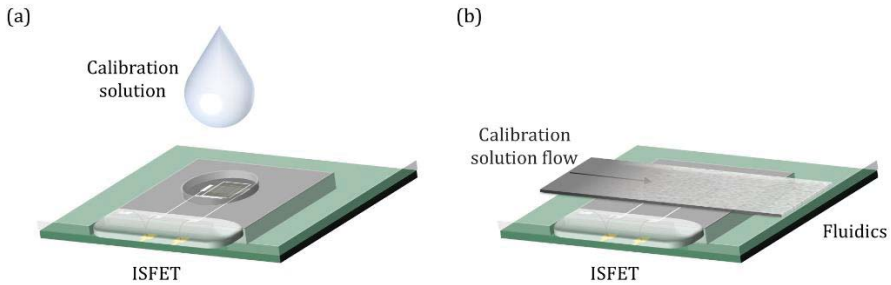

Figure 6.5. Experimental set-up used to evaluate the sensors integrated into the patch with calibration solutions on drop (a) or driven through the capillary-based fluidics (b).

6.2.4.1. Characterization of the REFET

The assessment of the REFET sensitivity to pH was carried out by performing calibrations in universal pH buffer solutions ranging from pH 4 to 9, and in an acid buffer solution basified with additions of a concentrated TRIS solution in a range of pH 4 to 9.9. The potentials were recorded against a commercial RE using the ISFET-meter (section 3.4.1). Furthermore, the sensitivity to Na^+, K^+, Cl^- and NO_3^- ions was evaluated by calibrating the REFETs in NaCl and KNO_3 solutions at concentrations of 1, 10 and 100 mM.

The REFET stability in aqueous solutions was assessed by immersing the sensors in a pH 7 buffer solution for 48 hours. Their physical appearance was examined under an optical stereo microscope.

6.2.4.2. Characterization of the Ag/AgCl/PVB reference electrode

The Pt thin-film electrode surface was cleaned by applying 15 cyclic voltammetric scans from -2.2 V to 0.3 V in a 0.1M KNO_3 solution. Then the Ag/AgCl film was deposited to produce a pseudo-RE, which was tested by recording the potentials of pH, Na^+, K^+ and Cl^- ISFET sensors against it. The pseudo-RE showed a response to changes in Cl^- concentration, and therefore solutions free of Cl^- were employed in all the sensors' calibrations. The solutions used in this assessment included a pH universal buffer spiked with TRIS to set the pH in the range of 4 – 9, as well as $NaNO_3$ and KNO_3 solutions with concentrations in the range of 1-100 mM. The performance of the ISFET sensors against the developed RE was compared with those responses recorded against a commercial Dri-Ref RE.

After this study, the PVB layer was cast on the Ag/AgCl layer, as described above, and the performance of the resulting RE was assessed in solutions containing the most relevant ions found in sweat. As previously discussed in section 6.1, the developed RE was required to meet specific criteria related to providing a consistent and stable potential regardless of changes in the measuring sample composition. In order to assess it, OCP measurements were conducted using an Autolab potentiostat (section 3.4.4) in electrolyte and artificial sweat solutions, both of which contain Cl^- ions. The Ag/AgCl/PVB modified electrode was employed as WE against a double-junction commercial RE. To determine the number of PVB layers necessary to neglect the Ag/AgCl sensitivity to Cl^- ions, OCP measurements were performed with three REs without PVB, after depositing one PVB layer, and after depositing three PVB layers. The OCPs were recorded in 10 – 100 mM NaCl solutions.

The thickness of the Ag/AgCl layer and the three PVB layers was measured by producing RE electrode dummies prepared by just coating half the area of the thin-film Pt electrode. The thicknesses of both components were visualized with a confocal microscope.

The RE working stability was assessed by recording the OCP signals for one hour with three Ag/AgCl/PVB RE against a Dri-Ref RE, in an artificial sweat solution, aiming to mimic the real conditions of work. The noise signal was calculated as the variation of the potential of consecutive data points (dE/dt).

Finally, the potential stability of the RE in the presence of varying concentrations of Na^+, K^+ and Cl^- ions was evaluated. The OCP signal of three RE was recorded for four minutes while immersed in the five artificial sweat solutions spiked with TRIS, NaCl and KNO_3 (C1-C5 compositions described in 3.1).

6.2.4.3. Selection of a coating for the sensors' encapsulation in the patch

As detailed in section 6.2.3, various coatings for sensor encapsulation on the chosen flexible PI substrate, were tested with regard to their curing conditions, mechanical strength, and water permeability. Silicone coating Dowsil™ 3140 RTV and epoxy resins EPO TEK® H70-E2, and Delo-duopox® CR8021 were cured on small pieces of the PI material. Epoxy H70-E2 was cured at 80°C for 1.5 hours while epoxy CR8021 was cured at room temperature for 48 hours, times at which the manufacturer indicated that the materials achieved 95% of their final strength. The silicone was cured at room temperature for 24 hours, time at which the manufacturer stated that the material attained 90% of its full physical properties. Their appearance and strength were examined both before and after being immersed in a 1 mM KNO_3 solution for 5 hours. Then, the coating that showed the best properties was used to encapsulate four chips on the PI substrates. The chosen chips were conventional Au thin-film electrodes, due to their simplicity of encapsulation, since they required a single wire-bonding, and the previously reported high analytical performance reproducibility [118]. The suitability of the coatings for sensor encapsulation was assessed by recording CVs from 0

to 0.4 V, at 100 mV s^{-1} in calibration solutions containing 0.1 – 1 mM FcMeOH in KNO_3 0.1M. A Pt wire and a 2 mm diameter Dri-Ref RE were used as CE and RE, respectively.

6.2.4.4. Evaluation of the multi-channel readout electronics

A new multi-channel readout system was custom-made at our laboratories for wearable application, as described in section 3.4.5. The electronics performance was assessed using the second patch-like device architecture, in which three pH ISFETs, a temperature sensor and a Pt thin-film electrode were previously encapsulated. During the test the potential between the pH ISFET sensors and a commercial RE was recorded in universal pH buffer solutions at pH 4, 7 and 10. The sampling frequency and the quality of the signal in terms of stability and noise were analysed.

6.2.4.5. Selection of the fluidics design and material

Various materials were studied to be used as fluidic components to drive the sweat over the sensors. Properties such as mechanical strength, flow uniformity, flow rate, capacity and sample renewal were evaluated.

Preliminary evaluations of fluidic materials were conducted before their integration into the patch. These tests involved the uncontrolled flow of blue- and red-dyed DI water solutions through these materials to assess their capillary behaviour in terms of wettability and flow rate. Materials showing promising performance were further examined on patches integrating Na^+ ISFET sensors, in order to test the possible variation of the sensor signal compared to that measured in batch conditions. Then, the fluidic materials were used in the calibration of other sensor devices with either stock solutions or artificial sweat solutions. In some tests the flow rate was settled at the inlet by controlling the time of each drop delivered, but also with a

syringe pump when required. Eventual tests were carried out in real sweat samples so that any matrix effect could be taken into consideration.

6.3. Results and Discussion

The key findings attained during the fabrication and characterization of the patch and its different components, including the potential REFET, the Ag/AgCl/PVB integrated RE, the multi-channel readout electronics, and the fluidic elements.

6.3.1. Preliminary tests for the development of a REFET

The purpose of this part of the research was to formulate a hydrogel that, upon deposition on a pH ISFET gate, made the device non-sensitive to pH, thus enabling its operation as a reference electrode for ISFETs potentiometric measurements. Such a device is called REFET. This formulation aimed to meet the specified requirements for REs outlined in section 6.1. The use of a REFET instead of a traditional solid-state reference electrode would mitigate drift effects since both devices utilized in the potentiometric measurement would share the same temporal drift. Furthermore, it would streamline the future development of an electronic chip comprising both the sensor devices and the readout electronics.

Hydrogels based on polyHEMA were prepared as described in section 6.2.1. According to the literature, the polymer is hydrophilic and mechanically robust when polymerized. It can be easily adhered to ISFET Si_3N_4 gate and its capacity for stabilizing the potential recorded while inhibiting the pH sensitivity has previously been demonstrated. It is also compatible with the ISFET manufacturing process. Some hydrogel formulations based on polyHEMA were studied. The criteria for defining the

optimal formulation were: a) High water retention; b) Minimum swelling; and c) Minimum sensitivity to the analytes present in sweat. The initially studied formulation consisted of a polyHEMA mixture containing 40% (w/w) of a 0.1 M $Mg(NO_3)_2$ solution. The first assessment aimed to test the membrane capacity to block pH recognition sites in the ISFET gate. The potential between the device and a commercial RE was recorded in universal pH buffer solutions ranging from pH 4 to 9, both with (w/) and without (w/o) the hydrogel. A noticeable decrease in sensitivity to pH changes was observed after depositing the polyHEMA layers, as illustrated in Figure 6.6a. The ISFET sensitivity to pH was reduced from 54.4 to 6.8 mV pH^{-1}. However, following its use, the polymer experienced a significant volume decrease due to the leaching of the electrolyte solution. Adjusting the aqueous fraction proved ineffective, as a high proportion of polyHEMA decreased membrane hydrophilicity, hindering the solution penetration, whereas an excess of the aqueous solution resulted in significant hydrogel volume loss. Consequently, the incorporation of aqueous solutions into the polyHEMA matrix was deemed impractical, prompting the exploration of alternative compounds.

Polyelectrolytes were considered, as their hydrophobic nature could enhance hydrogel stability. polyMETAC was chosen based on the previous experience of other groups [117]. Several formulations with varying proportions of the copolymer were prepared at the POLYMAT Basque Center for Macromolecular Design and Engineering (Spain). They found that the formulation that exhibited minimal swelling when immersed in electrolyte solutions was poly($HEMA_{80}$-$METAC_{20}$). This mixture was deposited and photocured on three pH ISFETs, resulting in completely flat, uniform, and transparent cured hydrogels (Figure 6.6b). Subsequent examination of the device sensitivities to pH indicated a significant decrease in sensitivity following the hydrogel deposition. The average pH sensitivity dropped from 51.7 ± 0.3 mV pH^{-1} to -1.2 ± 0.5 mV pH^{-1}, as demonstrated in Figure 6.6c. Importantly, the hydrogel retained its appearance after use and was stable

rendering it as a promising candidate for the REFET device. However, when sensitivity to other ions was assessed, the REFETs did not maintain a stable potential. Specifically, in NaCl and KNO_3 calibrations, the sensor displayed negative sensitivities of -53.9 and -64.3 mV dec^{-1}, respectively (Figure 6.6d). This behaviour suggested that the REFET devices were responding to changes in Cl^- and NO_3^- concentrations. This observation may be attributed to the presence of quaternary ammonium groups within polyMETAC that act as ionic recognition compounds for the mentioned anions. A similar salt response has previously been observed in other polymers containing quaternary ammonium groups [119–121].

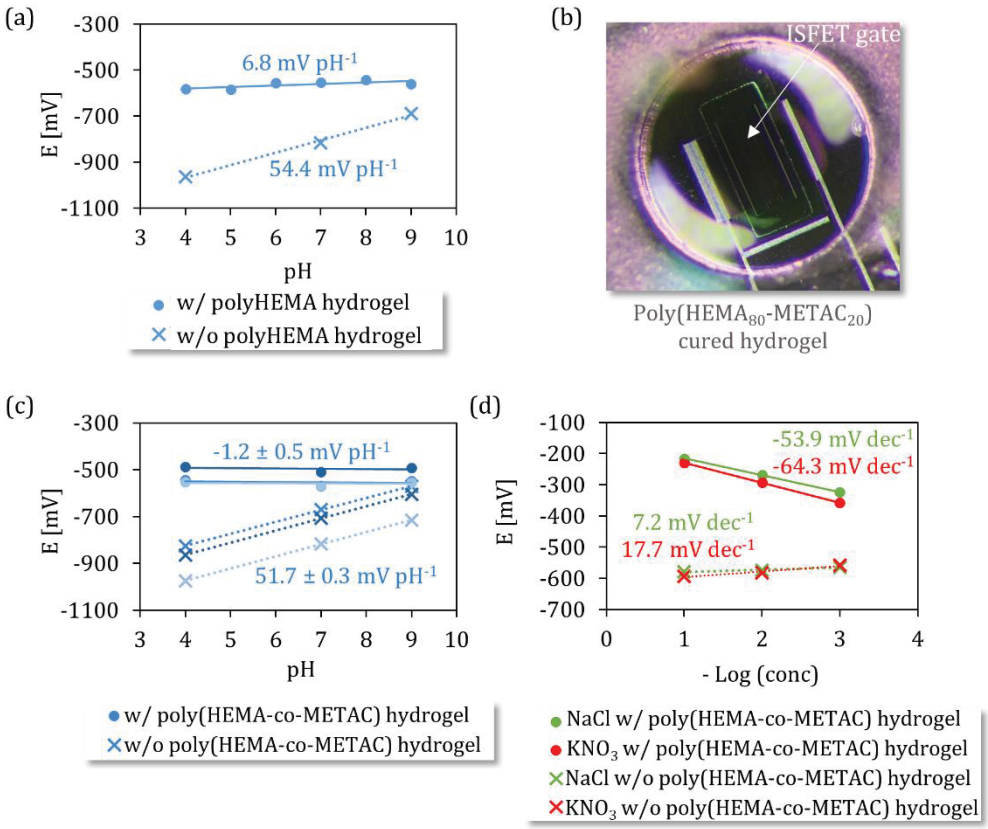

Figure 6.6. (a) Calibration curves of a pH ISFET coated with polyHEMA hydrogel containing 40% $Mg(NO_3)_2$ 0.1M, in universal pH buffer solutions (pH 4, 7 and 9). (b) Image of a cured poly($HEMA_{80}$-$METAC_{20}$) hydrogel on a pH ISFET. Calibration curves of pH ISFETs with poly($HEMA_{80}$/$METAC_{20}$) hydrogels in universal pH buffer solutions (pH 4, 7 and 9) (c) and in 1, 10, 100 mM NaCl and KNO_3 solutions (d).

To counterbalance the positive charges associated with polyMETAC, polyAMPS anionic polymer was introduced into the formulations. This led to the development of three new compositions at POLYMAT, which combined METAC and AMPS, and that are outlined in section 6.2.1. Their electrochemical characterization in buffer of different pHs revealed that the formulations inhibited the ISFET device sensitivity to pH, providing values of -0.1 ± 7.6 mV pH^{-1} (Figure 6.7a). However, they were still sensitive to Cl^- and NO_3^- concentration changes, yielding average slopes of -33.3 ± 4.7 mV dec^{-1} and -41.6 ± 0.8 mV dec^{-1}, respectively (Figure 6.7b). Moreover, as depicted in Figure 6.7c, the photocured polymers exhibited a visually homogeneous appearance. However, when immersed in a pH 7 buffer solution for 48 hours, substantial swelling occurred, resulting in a wrinkled and irregular surface. Consequently, none of these formulations proved suitable for the production of a robust REFET device and further exploration of alternative mixtures would be required.

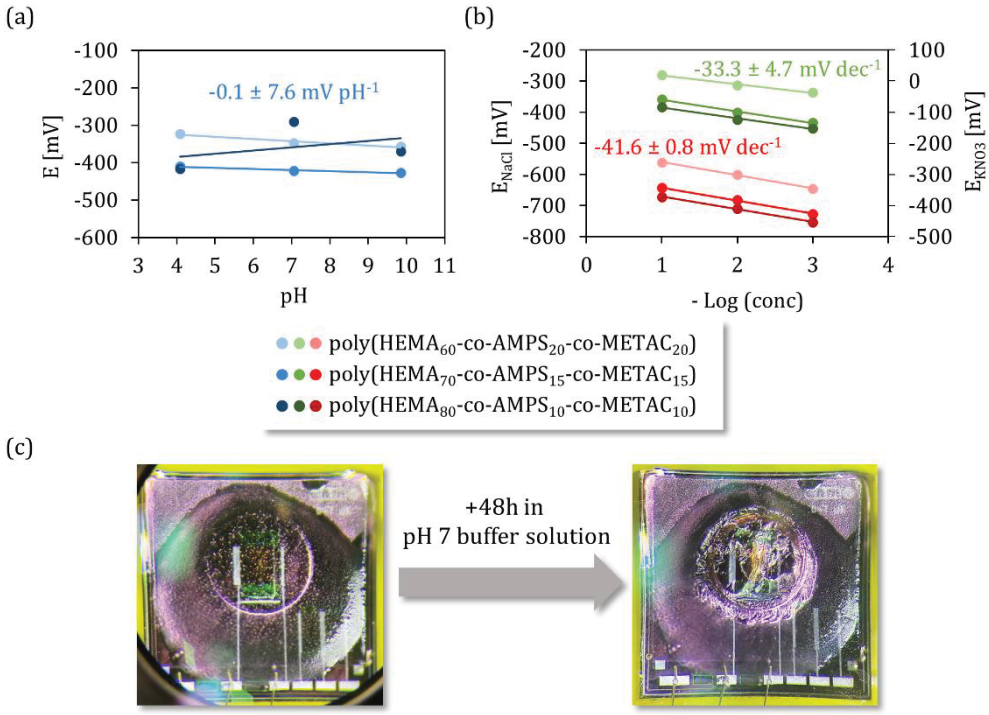

Figure 6.7. Calibration curves of pH ISFETs with poly(HEMA-co-AMPS-co-METAC) hydrogels in a TRIS spiked acid buffer solution (pH 4, 7 and 9.9) (a) and in 1, 10, 100 mM NaCl and KNO_3 solutions (b). (c) Images of a poly(HEMA-co-AMPS-co-METAC) hydrogel on an ISFET gate before and after being immersed in a pH 7 buffer solution for 48 hours.

6.3.2. Development of an integrated reference electrode

A reference electrode was developed and optimized to fulfil the requirements for real-time continuous monitoring of sweat using the wearable platform. As previously detailed in section 6.2.2, a Pt thin-film electrode was employed as the substrate, onto which Ag/AgCl and PVB polymeric layers were deposited.

6.3.2.1. Characterization of Ag/AgCl ink

The electrochemical performance of a Pt thin film-electrode modified with a layer of Ag/AgCl ink was evaluated. For that, the potentiometric

responses of pH, Na^+ and K^+ ISFETs against the RE were recorded and overlapped with those of the ISFET sensor devices against a commercial RE. The resulting calibrations are depicted in Figure 6.8a. The differences observed in the sensitivities of the pH, Na^+ and K^+ ISFET sensors extracted from both calibrations were minimal, varying only by 1.3, 5.7 and 2.9 mV dec^{-1}, respectively. By contrast, an average potential difference of 185.2 ± 9.4 mV was observed between both reference electrodes. This increment did not pose any difficulties to the ISFET sensor' potentiometric detection capabilities.

However, it is crucial to note that this pseudo-RE, in its existing state, would be susceptible to interference from Cl^- ions, which are known to disrupt the Ag/AgCl redox equilibrium [122]. Consequently, it would be unsuitable for monitoring biomarkers in sweat, which is known to have a variable concentration of Cl^- ions throughout a sports session. To mitigate this issue, an extra layer of polymeric material was required for the RE optimal performance.

6.3.2.2. Characterization of the Ag/AgCl/PVB reference electrode

The development of a polymeric membrane to be integrated into the Ag/AgCl pseudo-RE characterized in the previous section is a critical step as the membrane should fulfil the following requirements: a) to act as a barrier to avoid the sensitivity to Cl^- ions; b) to avoid Cl^- leaching from the reference electrode; c) to allow the electronic transfer between the solution and the Pt surface; and d) to keep its chemical and mechanical properties throughout the exercise performance.

We chose to formulate a PVB prepolymer solution that could be conveniently applied and cured at room temperature over the Ag/AgCl layer. Earlier studies already showcased its effectiveness in solid-state reference electrodes [109,110]. The fabrication of the membrane was tailored to meet the previously mentioned requirements of our device. To

do so, OCP measurements were carried out against a commercial RE, both before and after depositing one and three PVB layers. The changes in the potentials recorded in solutions ranging from 10 to 100 mM NaCl were examined. As depicted in Figure 6.8b, the responses of the REs to Cl^- ions without the PVB layer exhibited Nernstian behaviour, as expected, with an average slope of -56.8 ± 3.0 mV $(\text{Log } a_{Cl^-})^{-1}$. Notably, the responses decreased significantly upon deposition of a single PVB layer, resulting in sensitivity to Cl^- of -9.5 ± 5.0 mV $(\text{Log } a_{Cl^-})^{-1}$ (N=3). With three PVB layers, the RE exhibited no discernible responses to changes in Cl^- concentration. From these results, it was concluded that three PVB layers were adequate to avoid the electrode sensitivity to Cl^- ions.

The resulting thicknesses of the Ag/AgCl layer and the three PVB layers were characterized with a confocal microscope. As shown in Figure 6.8c, they were 45 μm and 55 μm, respectively.

Once the adequate PVB membrane thickness to prevent sensitivity to Cl- ions was defined, the RE working stability was evaluated. OCP signals were recorded with three Ag/AgCl/PVB REs against a commercial RE in an artificial sweat solution for one hour. The recordings and the noise signals are plotted in Figure 6.8d. The variation of potential overtime was 0.19 ± 0.09 mV min^{-1} (N=3), with an average noise (dE/dt) of ± 0.045 ± 0.01 mV s^{-1} (N=3). A variation of approximately 10 mV within one hour should not significantly affect the determination of the target analytes during the exercise performance. Preventively, calibrations before and after the session were planned to be performed in order to account for the impact of RE and ISFET sensor drift over time. Moreover, the low noise levels detected could be neglected and thus we could anticipate that the wearable device would produce robust concentration values for the different target analytes.

An experiment to assess the stability of the RE in artificial sweat solutions spiked with increasing amounts of TRIS, NaCl and KNO_3 was carried out. As shown in Figure 6.8e, the OCP signals of three REs in these solutions

exhibited an average standard deviation of ± 0.97 ± 0.62 mV (N=3). This test eventually confirmed that the electrode potential would remain stable regardless of the target analyte concentrations being measured. It could be concluded that the optimized Ag/AgCl/PVB RE was suitable for our application.

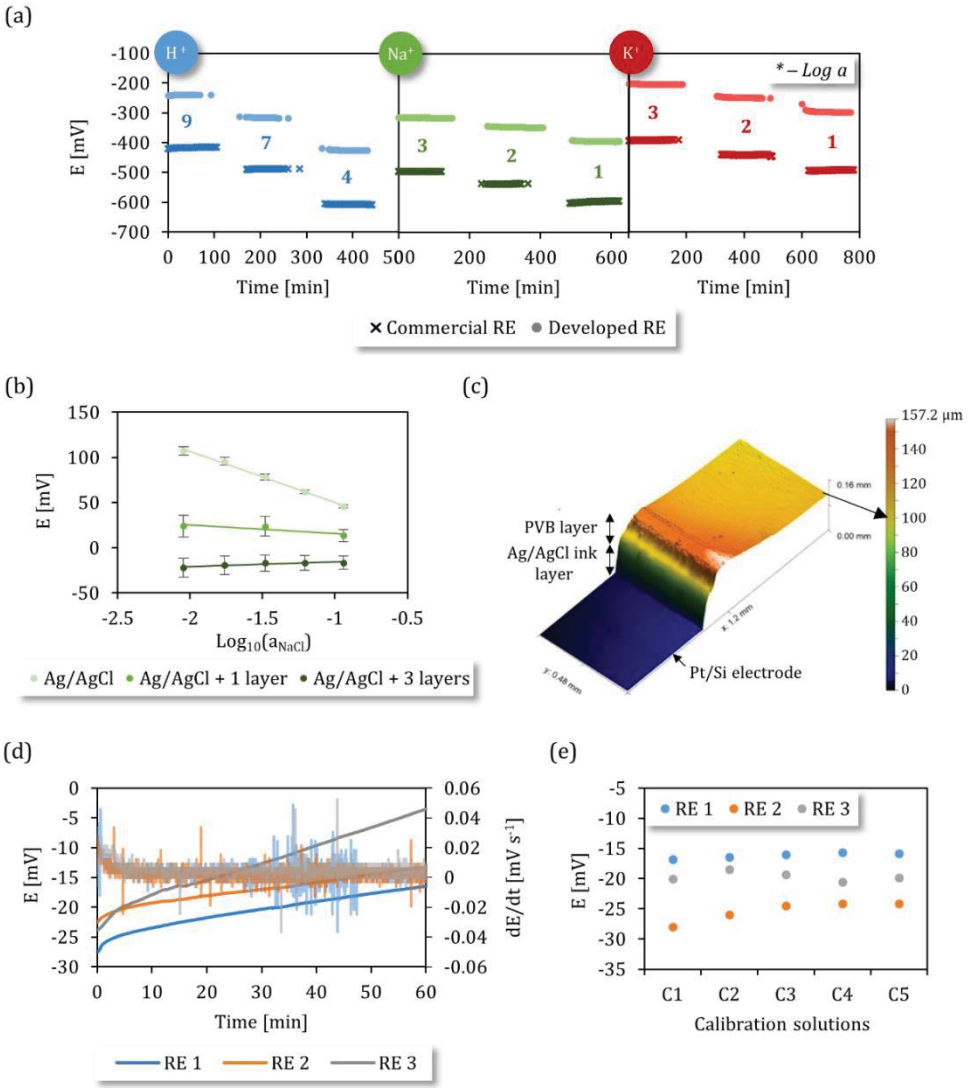

Figure 6.8. (a) pH, Na^+ and K^+ ISFETs calibration using a commercial RE and the pseudo-RE developed. (b) Calibration curves of the RE without, with one, and with three PVB layers in NaCl solutions. (d) Confocal image of the different layers, labelled with the thickness, that constitute the Ag/AgCl/PVB RE. Potential drift and noise of the developed RE recorded in artificial sweat solution for 1 hour. (e)

Potentials reached after 4 minutes in five calibration solutions prepared in artificial sweat.

6.3.3. Evaluation of the sensors encapsulated in the wearable patch

The new wearable patches developed in this thesis also required the development of a new process for sensor encapsulation onto the flexible substrate. The encapsulation comprises the fixation of the chip on the substrate, the wire bonding between the chip contact pads and electrical tracks of the substrate, and the final coating of the wires and electrical parts of the patch. To protect the chips, the applied coatings must meet some requirements such as good electrical isolation, chemical resistance, and mechanical robustness. In addition and for our specific application, this coating must be cured at low temperatures due to the thermal limitations shown by the materials used for the patch and the encapsulation layer of the chip. Therefore, three different coatings were tested and compared. As described in section 6.2.3, the coatings were silicone 3140, epoxy H70E-2, and epoxy CR8021. All of them showed the same appearance before and after their immersion in 1 mM KNO_3 solution for 5 h. Then, the mechanical properties were assessed. Epoxy H70E-2 displayed rigidity and hardness, potentially leading to a slight risk of delamination due to inadequate conformity with the skin. By contrast, epoxy CR8021 and silicone coatings showed to be more flexible, being thus more suitable for our wearable device. Lastly, the level of adhesion was a critical factor in assessing the suitability of the coatings. Epoxy H70E-2 and the silicone were found to be easily detachable, while epoxy CR8021 exhibited superior adherence. Therefore, epoxy CR8021 was the best coating for fixing and protecting the chip connections and patch electrical parts of our device.

The feasibility of this encapsulation coating was tested by performing electrochemical measurements. The selected coating was applied for encapsulating four Au thin-film electrode chips onto four different flexible PI

substrates. CV analyses were conducted in five calibration solutions containing 0.10, 0.25, 0.50, 0.75 and 1 mM FcMeOH in KNO_3 0.1M, employing a three-electrode configuration (as depicted in Figure 6.9a). The maximum faradaic current values corresponding to the oxidation peaks (I_{ox}) of the $FcMeOH^+$ were extracted from the CV curves (Figure 6.9b). The mean current and corresponding standard deviation of the response of the four electrodes were calculated and represented against FcMeOH concentrations, as displayed in Figure 6.9c. These data exhibited standard deviations below $1.8 \cdot 10^{-7}$ A, indicating a good reproducibility between sensors, and a linear relationship with an average regression coefficient of 0.9983. Finally, the electrodes were immersed in a 1 mM FcMeOH solution for 2 hours and tested again to show that the electrodes still kept a suitable voltammetric signal. From these results, we could conclude that the epoxy CR8021 was adequate for the encapsulation of the sensors in the PI-based wearable platform.

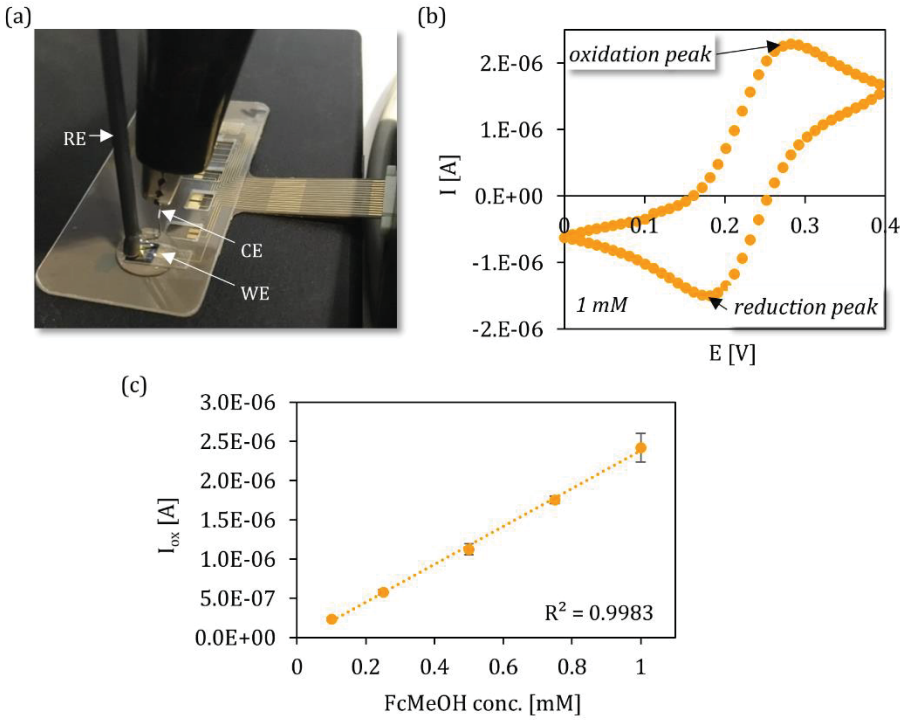

Figure 6.9. (a) Picture of the amperometric measurement set-up on the patch to test the feasibility of the coating procedure: Au/Si thin-film electrode as WE, Dri-Ref as RE, and Pt wire as CE. (b) Example of a CV curve recorded in a 1 mM FcMeOH solution.

(c) Calibration curve representing the mean and standard deviation values as error bars of the I_{ox} registered by four Au electrodes.

6.3.4. Validation of the multi-channel readout electronics

A compact and lightweight multi-channel readout system was developed to be incorporated to the final wearable patch system. This was tailored designed and manufactured by the ICAS group at the IMB-CNM. The details are thoroughly explained in section 3.4.5. An image of the electronic PCB is illustrated in Figure 3.4. It allowed continuous real-time monitoring of the target analytes, and the collected data was visualized on a laptop. To establish electrical connectivity between the pads on the flexible PI substrate and the readout PCB, it was imperative to select a connector that could withstand the vibrations and movements resulting from the subject's physical activities while also offering easy reversibility for patch replacement. Among the different types of connectors, the ZIF connector was selected taking into account its user-friendly insertion and removal process that required minimal force. Furthermore, ZIF connectors are the same time highly robust fitting very well with our application.

The performance of the readout electronics was evaluated by connecting it to a patch-like platform containing three pH ISFETs, a Pt thin-film electrode chip, such as the one used for manufacturing the RE, and a temperature sensor, and recording the ISFETs potentials in pH buffer solutions. The recordings are shown in Figure 6.10a. They exhibited the following characteristics:

- ISFETs' data was read sequentially, taking an approximate total time of 7.4 seconds for each round, corresponding to the measurement frequency.
- The sensors' reading resolution was set at 0.1 units.
- The signal average noise closely matched the electronics resolution, this being within ±0.5 mV or 0.1°C between consecutive data points.

- Unfortunately, the amperometric measurement could not be recorded because of electronic interference with the ISFET potentiometric measurements.

The potential signal from the three ISFETs was stable, yielding an average pH sensitivity of 46.5 ± 0.5 mV pH^{-1}. This achieved pH sensitivity was as expected, considering that the measurements were conducted before the removal of the native SiO_2 layer formed at the ISFET gate, and that was previously described in section 3.2. From these results, we could state that the readout electronics operated properly. However, it should be mentioned that after the use of the electronics with several patch changes, the ZIF connector got degraded and experienced slackening, leading to a loss of electrical contact. In an attempt to avoid this drawback, the ZIF connector was mounted onto a flexible extension of the readout electronics that was linked between the patch and the readout PCB. A scheme of this and a picture of the whole device when implementing this element are depicted in Figure 6.10b and Figure 6.10c, respectively. This approach avoided the need to open the ZIF connector at the readout PCB when exchanging patches. Instead, the flexible extension could be replaced when its ZIF connector showed signs of slackening, ultimately saving both time and resources.

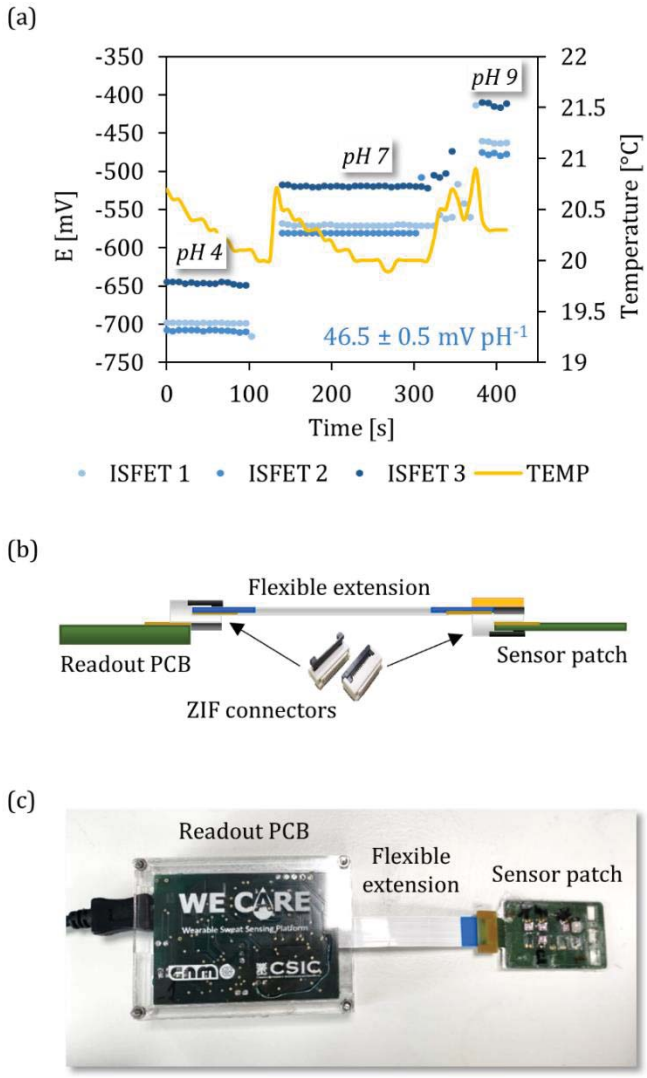

Figure 6.10. (a) Patch sensors' recordings using the readout PCB. (b) Schematic cross-view of the flexible extension that connects the sensor patch with the readout PCB. (c) Picture of the wearable device, including the sensor patch, the flexible extension and the readout PCB.

6.3.5. Optimization of fluidic structure design

To enable continuous monitoring of the target analytes over extended periods of time, it is essential to incorporate fluidic components within the wearable devices that are as simple as possible and do not need any external actuator for solution pumping and driving. For this, paper-like materials

were chosen due to their capacity to enable fluid flow through capillary action. These components should facilitate efficient sweat transportation to the sensor areas, ensuring rapid and consistent sweat delivery, as well as effective sweat replenishment. For this, our main aim was the design of fluidic structures small enough to drive the low-volume sweat sample flows that were expected, so that the sensor response times were as short as possible. For this, several fluidic structures were designed and tested, which also impacted the design of the final PI flexible base substrate of the wearable patch-like device.

The first fluidic structure was designed to cover all the sensors packaged in the firstly produced wearable platform, which was described in section 6.2.3. Several designs were studied and the selected fluidic architecture is depicted in Figure 6.11a. It consisted of three structures comprising a first sweat collection pad in contact with the skin (40.5 x 4.0 mm), the microfluidic channels in contact with the sensors and an absorbent pad (40.5 x 7.8 mm) that facilitates continuous transport and removal of sweat once it has flown over the sensors. The intermediate microfluidic structure was defined for each sensor chip, each one showing a particular structure depending on the sensor geometry. All channels showed a width of 1 mm, which is the minimum resolution that could be reproducibly patterned with the CO_2-laser cutter. Wider structures were defined on the areas contacting the sensors, that is 2-mm diameter circled areas for the ISFETs, 2x2 mm^2 area for the reference electrode, and 3x2.5 mm^2 area for the temperature sensor. Additionally, a 1 mm-diameter circled pad of the same material used for the channel was adhered to fill the encapsulating window in the pH ISFET, defined for the deposition of the membranes of ion-selective membranes (Figure 6.11b). This pad enabled the sweat solution flowing on the channel to more easily reach the pH ISFET sensor area, also avoiding dead volumes where the sweat could accumulate and hinder its renovation during the device monitoring performance.

This design was first tested with artificial sweat without controlling the flow rate. We could observe a non-uniform flow distribution across the channels due to variations in their lengths and geometries, as clearly illustrated in Figure 6.11c. Such discrepancies in fluid flow times to reach the different sensor areas would make the simultaneous real-time detection of the target analytes rather complicated. To further assess this drawback, an average sweat flow rate of 1.5 μL cm^{-2} min^{-1} that could be expected during physical exercise [21] was applied using a patch containing just Na^+ ISFET sensors encapsulated in the different sensor areas defined on the flexible substrate. Artificial sweat solutions containing 1 mM and 10 mM Na^+ concentrations were injected. The potential recordings are shown in Figure 6.11d. The initial solution required approximately 13, 18 and 20 min to reach the first, third and second sensors, respectively. An additional 5-min time was necessary for the sensor potentials to stabilize. The second solution injected after 20 minutes took a similar time to reach the sensors and attain stable potential values. This observation not only confirmed the effective contact between the fluidic components and the sensors, as evident in the nearly Nernstian potential change, but also indicated that the current design and patch configuration had to be redesigned to eliminate non-uniform flow rates. Finally, we considered that the detection time was too prolonged for real-time applications, prompting the need for adjustments to facilitate faster solution access to the sensors.

A second fluidic structure was then developed as is shown in section 6.2.3. A simple fluidic design was sought and for that, a vertical arrangement of the sensors all of them aligned with the sweat flow direction was produced. This design consisted of an oval-shaped pad for sweat collection in contact with the skin (d1 5.5 mm, d2 11.0 mm), a 6.4 mm wide T-shaped microfluidic channel in contact with the sensors, and a sink pad (22.7 x 7.9 mm) attached at the end of the fluidic structure that facilitated the continuous transport and removal of sweat flowing through the sensors. The design of the T-shaped

fluidic structure is depicted in Figure 6.11e. When testing this configuration approach under non-controlled flow, it could be seen that the solution was driven along the channel uniformly (Figure 6.11f). In a second test, using the same flow rate as above, expected during exercise performance, it took 20 minutes for the solution to reach the sink pad. Despite addressing the flow uniformity issue, the sensor detection times were long, this being mainly related to the width of the T-shaped channel.

Since the patch configuration could not be further condensed, alternative methods to accelerate the sweat flow were explored. The wettability of the material played a key role in the flow rate, prompting the examination of other materials for potential improvements.

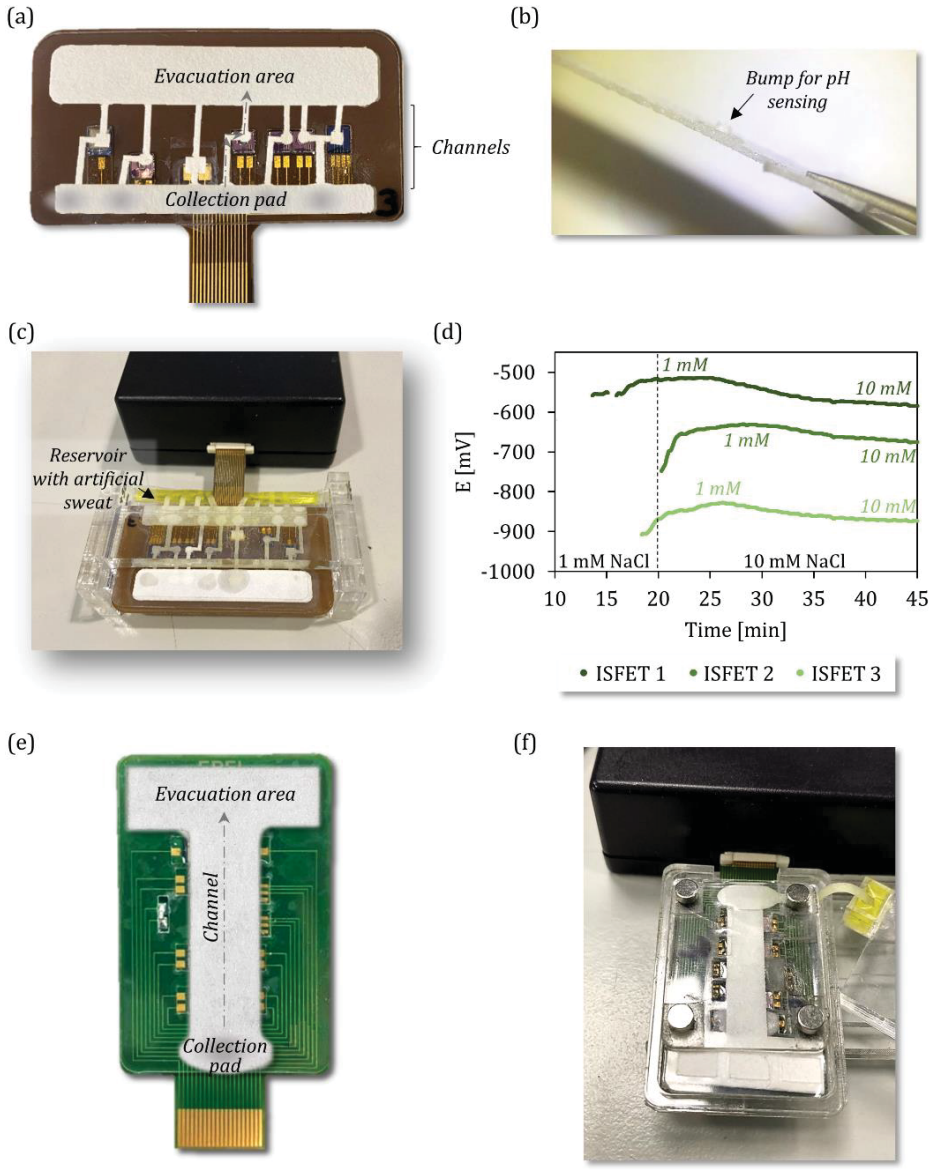

Figure 6.11. (a) Picture of the first capillary-based fluidic design for wearable applications. (b) Optical microscope image of the bump adhered to the microfluidic channel for pH ISFET sensing. (c) Picture of the patch with the first fluidics after driving artificial sweat from the collection to the evacuation area with uncontrolled flow. (d) Potential recordings of three Na^+ ISFETs encapsulated in the patch, when 1 mM and 10 mM NaCl artificial sweat solutions where driven through the fluidic layer of the first design. (e) Picture of the second capillary-based fluidics design for wearable applications. (f) Picture of the patch with the second fluidics driving artificial sweat from the collection to the evacuation area with uncontrolled flow

6.3.6. Evaluation of materials to produce the fluidic components

Filter papers have been widely used in wearable applications, as highlighted in the Introduction. Among the different types, Whatman filter paper grade 1 was first selected in this work due to its low cost, hydrophilic nature, availability, biocompatibility, homogeneity and proven wicking properties. Furthermore, previous studies have demonstrated its effectiveness in electrochemical paper-based devices [123–127]. However, as explained before, the delivered flow rate proved insufficient for real-time on-body sweat monitoring. Consequently, alternative filter papers were subjected to testing.

A wicking study was conducted using medium-slow (Whatman grade 6), medium-fast (Whatman grade 1), and fast (Whatman grade 4) filter papers. They were cut into a rectangular shape measuring 2.85 cm x 0.85 cm, and an adhesive was placed covering the central area, akin to the final patch structure. Red and blue dyed solutions were dropped onto rectangular areas, with a flow rate of 1.5 $\mu L\ cm^{-2}\ min^{-1}$.

The images documenting each minute of the test are shown in Figure 6.12**¡Error! No se encuentra el origen de la referencia.**. The solution linear speeds were 0.37 $cm\ min^{-1}$ for grade 1, 0.42 $cm\ min^{-1}$ for grade 4, and 0.35 $cm\ min^{-1}$ for grade 6. The results were aligned with the manufacturer's specified speeds, with the Whatman grade 4 exhibiting the highest speed. Although the linear speeds differed slightly, significant consequences arose when another solution was introduced. For grades 1 and 6, the solution flowed more rapidly through the adhesive material than the paper, hindering sample renewal. Conversely, grade 4 paper material demonstrated uniform sample renewal with a small diffusion front. Consequently, the Whatman grade 4 filter paper was selected.

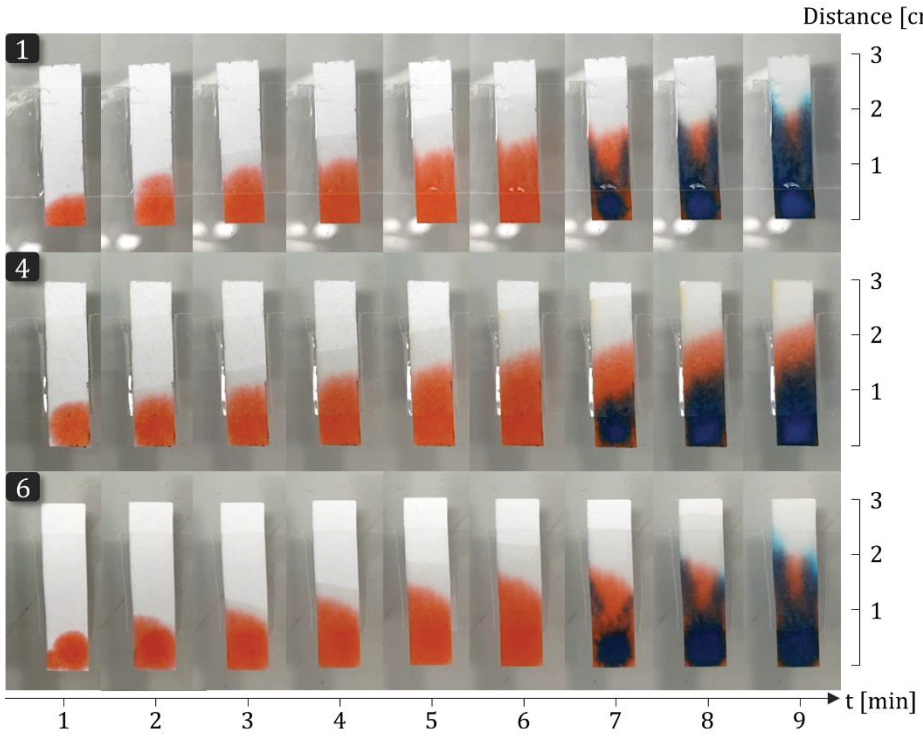

Figure 6.12. Images of the three filter papers (Whatman grades 1, 4 and 6) when adding red- and blue-dyed solutions at 1.5 μL cm^{-2} min^{-1} flow rate.

During the evaluation of the filter paper-based fluidics design, achieving a consistently optimal pressure above the channel was crucial for ensuring a uniform solution flow over all the sensors. To address this requirement, two types of PMMA structures were fabricated. In the first structure, the optimal pressure was determined by adjusting the height of the clamps, while in the second structure, various distributions, sizes, and strengths of neodymium disk magnets were tested. Details and images of the structures can be found in section 6.2.3. The speed of wicking for the Whatman filter grade 4 was assessed by measuring the time taken for solutions to flow through the fluidic design. As illustrated in Figure 6.13a, at its maximum flow rate, the solution took 18 minutes to flow along the whole channel area when starting from a dry state, and an additional 26 minutes when beginning from a wet state.

The effective transport of ions from the fluidic elements to the ISFET sensing area was assessed using the same setup as in the previous test. The

potential signal of three Na^+ ISFETs was recorded and Nernstian slopes were achievable during the transition from diluted NaCl solutions to more concentrated ones, as evidenced in Figure 6.13b. However, a hysteresis effect was noted when shifting from concentrated to diluted solutions. The average difference in sensitivity between both calibrations was 37.7 ± 10.6%. Upon detailed analysis, it was found that the potential variation for the 1 mM solution was twice as much as that for the 10 mM solution, averaging 43.9 mV and 22.9 mV of difference, respectively. This disparity contrasts significantly with the average changes of 3.2 mV determined for Na^+ ISFET during previous sensor characterizations using sensor strip encapsulation, described in section 4.3.2. These effects suggest, that the incorporation of fluidics negatively impacted the sensor performance. Presumably, the filter paper appeared to accumulate salts, as indicated by the previous test where the red-coloured area was not entirely replaced by the blue one, and a partial overlapping of both colours was observed (Figure 6.12). This accumulation likely led to an overestimation of sample concentrations, as ions from the prior solution remained on the sensor area when the new solution reached it.

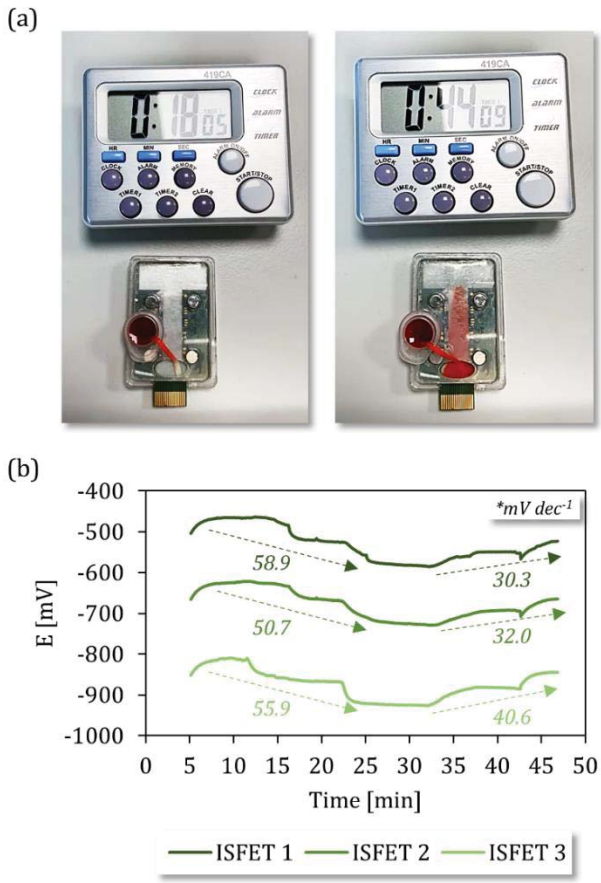

Figure 6.13. (a) Pictures of the wicking test conducted using Whatman filter grade 4 as the substrate of the fluidic structure: when the first solution had passed over all the sensors (*left*), and when the second solution did (*right*). (b) Potential recordings of three Na+ ISFETs integrated into the device with the fluidics and a PMMA structure during calibration. The sensitivities calculated for increasing and decreasing concentrations are pointed out.

While the device demonstrated functionality in its current form, the necessity of using a PMMA structure gives stiffness to the platform, and one of the initial objectives was to achieve a flexible design for better adaptation to the skin. Furthermore, from the last test, we observed a gradual and incomplete sample renewal, which could potentially result in the overestimation of target analyte concentrations. Hence, we explored alternative materials. We sought materials that should fulfil the following requirements:

- Consistent, continuous, and intimate contact between the fluidics and the sensors, achieved without the necessity of external pressure.
- Times below 18 min for the solution to reach the end of the fluidic dry channel, and below 26 minutes when the channel was fully wet.
- Uniformly fast and complete sample renewal.

PE and PE/PP-based fibre sheets emerged as potential materials for this purpose. As outlined in section 6.2.3, the PE fibre sheet was slightly thicker and denser than the PE/PP variant. For this reason, it was selected for the collection and sink pads. Otherwise, the PE/PP fibre sheet was specifically patterned for the T-shaped fluidic design. Their fluidic capabilities were assessed following similar tests as those described above. First, blue- and red-dyed DI water solutions were driven at their maximum flow rate through the PE/PP material cut into the T-shaped channel. As illustrated in Figure 6.14a and Figure 6.14b, it took 1 minute and 50 seconds and 2 minutes and 45 seconds to completely cover the dry and wet main channel, respectively. The material demonstrated a high wicking speed, and therefore its suitability for real-time sweat monitoring.

Moreover, the suitability of the PE material as a substrate for the collection and sink pads was assessed based on its hydrophilicity and absorption capacity. When a blue-dyed solution was dropped on it, immediate absorption was observed (Figure 6.14c), demonstrating its high hydrophilicity. Subsequently, a 1 cm^2 PE sample was saturated with real sweat and weighed. It absorbed 266 g, equivalent to an absorption capacity of 250 $\mu L\ cm^{-2}$. Notably, this is twice the absorption capacity of the sterile gauze pads that were provisionally utilized, which were reported to have an absorption capacity of 120 $\mu L\ cm^{-2}$ in blood [128]. Hence, PE material proved to be useful as a collection pad, and potentially as a sink pad. Furthermore, the drying rate of the material was calculated to determine if evaporation would significantly contribute to sweat evacuation from the sink pad during an exercise session. A 1 cm^2 portion of PE soaked in sweat was heated at 30°C,

akin to the skin temperature during exercise performance, as depicted in Figure 6.14d. The pad was periodically weighed every 5 minutes. The saturated pad reached a maximum evaporation rate of 6.1 μL min^{-1}. Considering the reported sweat rate during exercise performance being around 1.5 μL cm^{-2} min^{-1}, and with our collection pad area measuring 0.48 cm^2, the sweat collection rate was estimated to be around 0.7 μL min^{-1}. Therefore, the evaporation rate contribution would be adequate to keep a constant flow rate during the whole exercise test without reaching saturation of the fluidic component and in turn avoiding sweat overflow outside the wearable device.

Following these tests, the PE and PE/PP-based fibre sheets emerged as a potential alternative to the filter papers tested before. Then, other tests were planned in order to assess the fulfilment of the previously outlined requirements.

Firstly, the necessity of external pressure to maintain uniform, continuous and effective contact between the fluidics and the sensors was evaluated. The performance of a patch with the new fluidic components and the integrated RE was compared with that of the same patch without fluidics and using an external RE. The calibration curves for pH, Na^+, and K^+ ISFETs in both situations are depicted in Figure 6.14e. Notably, the calibration curves are overlapped, showing sensitivity differences of 0.03, 1.00, and 1.66 mV dec^{-1} for pH, Na^+, and K^+ ISFETs, respectively. This indicated efficient ion transfer from the fluidics to the ISFETs gate without the need for a PMMA structure for applying external pressure as described above.

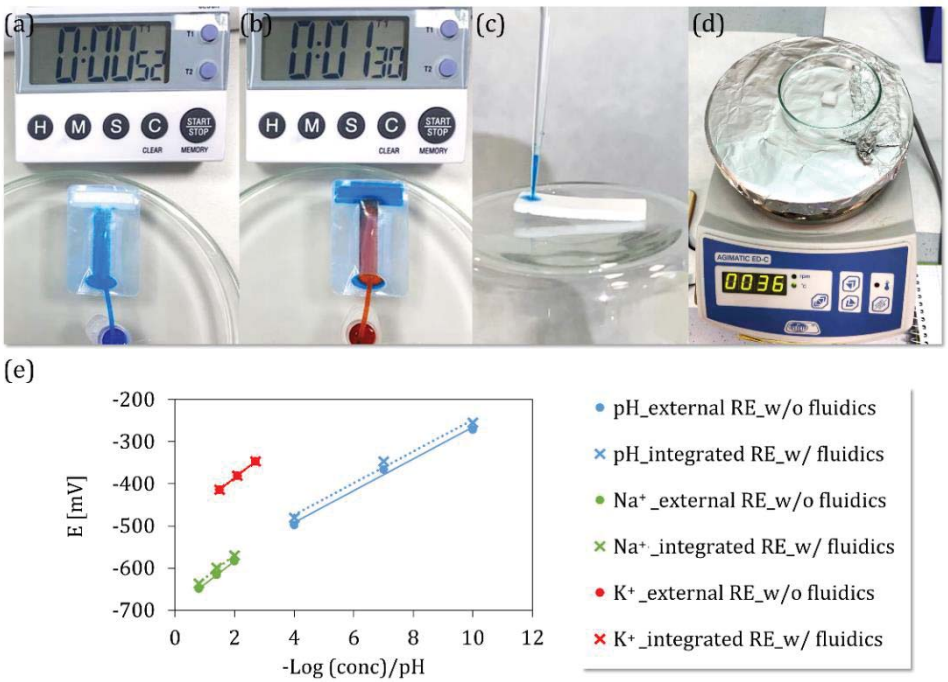

Figure 6.14. Pictures of the wicking test conducted using PE/PP material as substrate of the fluidic structure: when the first solution had passed over all the sensors (a), and when the second solution did (b). (c) Picture to demonstrate the hydrophilicity of PE material. (d) Picture of the 1 cm^2 PE pad saturated with sweat, being dried at skin's temperature. (e) Calibration curves obtained for pH, Na^+, and K^+ ISFETs integrated into the patch following two procedures: using an external RE and covering the sensors with a drop of solution (without (w/o) fluidics), and using the integrated RE and driving the solutions through the fluidics layer (with (w/) fluidics).

Using the PE/PP fluidic material in the T-shaped fluidic design, the sample renewal and the reversibility of the signal were assessed. The device was evaluated at a high flow rate of 100 µL min^{-1} using a syringe pump to replicate the continuous secretion of sweat, and positioned vertically, as would be on an athlete's back. The setup is illustrated in Figure 6.15a. Three calibration solutions (C1, C3 and C5, described in section 3.1) were successively pumped through the system, and the most diluted solution was injected at the end of the calibration. From the test results, depicted in Figure 6.15b, the following conclusions were drawn:

- Solutions were continuously driven in real-time, displaying negligible delay at the high flow rate.
- Abrupt potential changes between solutions indicated a small dilution front.
- Stable signals were observed throughout the test, regardless of the amount of solution injected and the wearable device's vertical orientation.
- No leakage or transport through the adhesive occurred when the fluidic components were saturated, meaning that the evaporation rate at the sink pad effectively removed the excess of sweat once it flowed into the system.
- Nernstian sensitivities were achieved for all the three ISFETs.
- The recorded signal was reversible, presenting potential differences between the diluted solution injected at the beginning and at the end of the calibration of 6.0, 11.9 and 1.0 mV for pH, Na^+ and K^+ ISFET sensors, respectively.

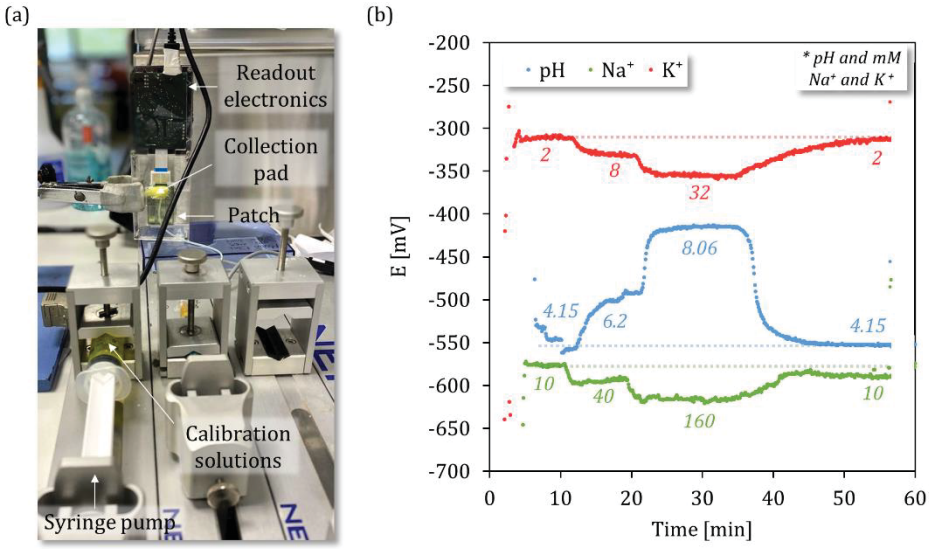

Figure 6.15. (a) Image of the set-up for the sensors reversibility test using T-shaped PE/PP material. (b) Potential recordings of pH, Na^+, and K^+ ISFETs integrated in the device with the fluidics, when artificial sweat solutions with different ion contents were sequentially pumped.

Finally, a real sweat sample was employed to test the matrix effect on the fluidic material, in order to discard the possibility of drawing erroneous conclusions as properties such as the particle size or the density may differ from the artificial sweat solutions previously used. The test started by coating the main channel and the collection pad with blue dye to visualize the fluid flow. Subsequently, a real sweat sample was manually dropped into the collection pad at a controlled flow rate of 20 μL min^{-1}. In parallel, the temperature, pH, Na^+ and K^+ sensors integrated in the patch were recording the respective signals. Figure 6.16 presents both the recordings and images of the patch at the beginning of the sweat flow and when the sensors detected a change. During the initial 2.5 minutes, the channel remained consistently and uniformly blue while the sensors' signals were stable. Between minutes 2.5 and 7, the blue colour in the main channel slightly diminished, and the voltage slowly changed, suggesting the arrival of the sweat sample to the sensors. After 7 minutes, the sweat overpowered the blue dye, and the signals stabilized, reaching over 97% of the stable value by the end of the recording. These findings suggested that, at a flow rate of 20 μL min^{-1}, the sweat sample could reach the sensors approximately after 7 minutes of absorption in a saturated fluidic channel.

These results demonstrated the potential application of the proposed wearable device configuration for real-time monitoring of the selected target analytes in sweat.

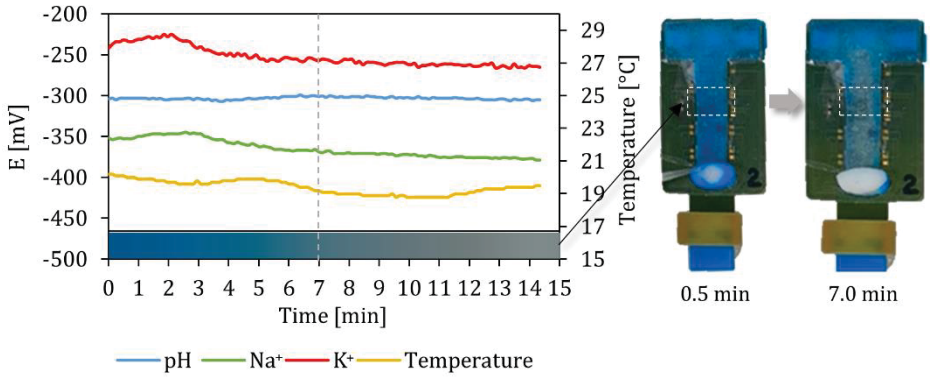

Figure 6.16. Recording of sensors' signals and pictures of the PP/PE microfluidic component in the patch soaked with blue-dyed DI along the time the sweat was advancing.

6.4. CONCLUSIONS

The results shown in this chapter demonstrate the capabilities of the wearable patch developed. This is the first time a wearable-like patch with ISFET-based sensors was developed in our group and it is also the unique patch described in the literature containing three ISFET-based sensors for measuring three different target analytes, a solid-state RE, a temperature sensor and a fluidic component based on a capillary-driven material with enhanced fluidic properties over more conventional filter paper materials reported before.

After a thorough optimization of the different elements of the patch, that is patch design, sensor packaging, connections with the tailor-made readout electronics and fluidic design and material, an optimal device was delivered and ready to be tested on the body.

Moreover, the steps comprising the development of the patch and a brief characterization were published in Publication 4 and Publication 6.

7 EVALUATION OF THE WEARABLE PROTOTYPE ON-BODY

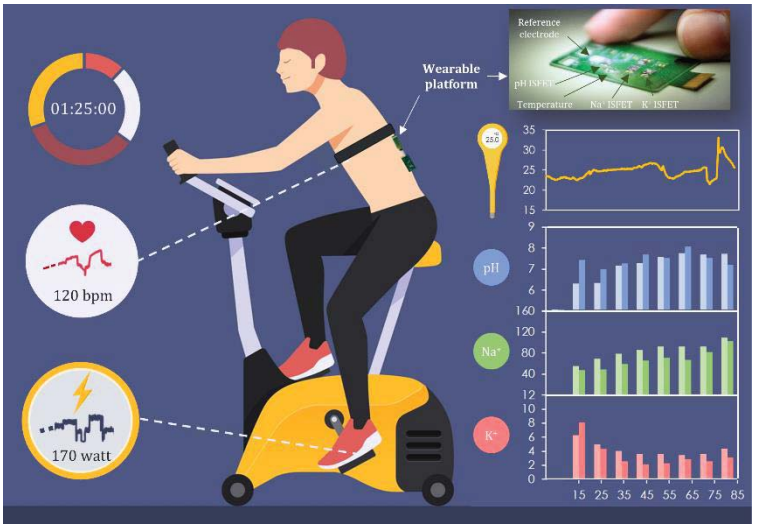

Figure 7. 1. Graphical abstract of the evaluation of the wearable prototype on-body.

7.1. INTRODUCTION

Throughout this thesis, various sensors have been explored for their potential application in sweat analysis. Given the reported studies in sports medicine and our project partners' research, we thought that Na^+ and K^+ biomarkers could be related to hydration status. However, the mechanisms

driving ion secretion in sweat during exercise remain unclear, primarily due to limited experimental tests in this area, which lacks reliable techniques for in-situ monitoring of the ionic content of excreted sweat. To address this gap, clinicians designed a clinical study comprising one subject and ten sessions. Previous research regarding the correlation between hydration status and sweat biomarkers during physical exercise frequently involved multiple participants, each conducting only one or two sessions [129,130]. Yet, it is widely recognized that the variability in biomarkers, such as sweat Na^+ concentration, can be substantial among individuals [131]. These studies primarily focused on inter-subject variability of biomarkers, while intra-subject variability during exercise is more crucial in the context of devising personalized hydration strategies for athletes. Hence, the clinical study conducted in the CHUV introduces a novelty by examining the relationships between various factors and biomarkers without considering inter-subject variability.

The data collected by the CHUV partners throughout the study has been analyzed to study the influence of various factors such as the intensity and the day of the exercise performance, the location of the patch or the hydration status in the concentrations of Na^+ and K^+ in sweat. This analysis involved the utilization of inferential statistical methods. CIs have been calculated to evaluate the data bias.

More complex inferential analyses often involve multiple samples and aim to establish relationships between patient populations or treatment groups. In clinical trials, a common practice is hypothesis testing for significance using p-values between groups. Each comparison assesses the probability of observed results occurring by chance, indicating the likelihood of differences between groups. Among them, parametric statistics such as *t*-test and ANOVA were employed in this work, which are those statistical tests that assume the data approximately follows a normal distribution. Further information about the previous statistical tests can be found in [132].

An additional statistical method utilized for conducting multiple comparisons was the Tukey honestly significant difference test. This method evaluates all possible pairwise comparisons among means. It proves valuable in identifying the most significant difference among a set of means derived from the same population.[133]

Once defined the best part of the body to test the wearable patch, this was tested on-body during several sessions. During the sessions, sweat's pH, Na^+, and K^+ concentrations, skin temperature, heart rate, and bike power were registered. The data collected from physical sensors could be useful for the prediction of parameters using machine learning algorithms.

Few works demonstrate sweat's on-body testing with ISFETs integrated in wearable platforms. Table x summarizes the state-of-the-art regarding wearable ISFET sensing.

In this chapter, the main results of the on-body sessions are explained and discussed.

7.2. EXPERIMENTAL SECTION

This section describes the clinical tests performed with trained subjects to collect sweat samples and to validate the developed wearable patch, described in Chapter 6, and the methodology followed to interpret the results from the tests. During the tests, the commercial LAQUAtwin ISEs (section 3.4.3), the custom-made readout electronics (section 3.4.5) and artificial sweat calibration solutions (section 3.1) were employed.

7.2.1. Sweat sample collection and on-body tests

Exercise sessions were organized depending on the tests required at the different stages of the project. The sessions were always performed in a laboratory at the *Swiss Olympic Medical Center* of the CHUV. Each subject rode on a stationary cycle ergometer (CycleOps Pro 400, CycleOps, Madison, USA) equipped with Assioma Favero power meter pedals (Favero Electronics SRL,

Arcade TV, Italy), which allowed the power output control [134] without cooling fans. The subjects were fully informed of the nature and risks of the study and were free to withdraw at any stage of the study.

Before the on-body testing of the wearable prototype, we wanted to determine which factors could produce errors in the measurement or cause physiological alterations in the concentrations of secreted sweat biomarkers. A study involving ten exercise sessions performed by a healthy, highly trained male volunteer was planned with this purpose. This was part of the study approved by the ethical commission of the Canton of Vaud, Switzerland (Protocol No. 2019_01235), described in Section 5.2.2. Each session was divided into three phases, each one lasting 20 minutes. The three phases were performed at a maximal aerobic power that did not exceed 55 % (MAP), being the MAP a measurement of the maximal amount of oxygen that the body can use to produce energy and that represents the upper limit of aerobic exercise tolerance. Sweat samples from different parts of the body were collected after each phase. The methodology for the sample collection was the same as the one described in section 5.2.2. Sweat samples were carefully labelled regarding the day/session of collection (S), degree of effort (E) and the position where the absorbent was placed (P). The codification used for each sample is schematized in Figure 7.2. The total number of samples collected during a single session was 33 (one sample per each of the 3 effort stages and 11 body positions).

Among the ten sessions carried out, the odd sessions were performed without hydration (NH), whereas the even sessions were performed with hydration (H). During H sessions, the subject was asked to drink a total of 1 L of water. To allow for gastric emptying, right at the beginning of each phase and 10 min later, the subject drank 0.2 L for E1 and E2, and 0.1 L for E3.

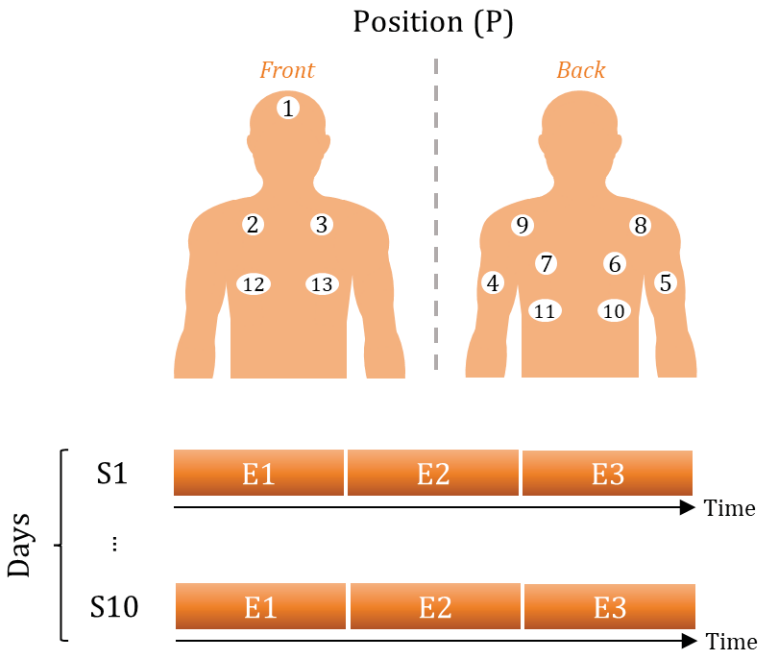

Figure 7.2. Scheme of the codification used for each sweat sample related to the part of the body sweat was collected the session, and the session effort stage.

Once validated the wearable device and determined the factors that could contribute to changes in biomarker concentrations, sessions for on-body evaluation of the patch were planned. They were performed in compliance with the protocol that was approved on May 10th 2021 by the ethical commission of the Canton of Vaud, Switzerland (Protocol No. 2019_01235), and therefore performed in accordance with the ethical standards laid down in the 1964 Declaration of Helsinki. Healthy, highly trained volunteers were recruited to participate in the study by cycling on the stationary cycle ergometer. Apart from the equipment stated above, heart rate (HR) was also recorded continuously with a sampling rate of 1 Hz using a smartwatch (Garmin, Fenix 5S) and an HR belt (H7, Polar Electro OY, Kempele, Finland) throughout the session. The sessions monitored with the patch lasted 75 min and consisted of a warm-up and three different intensity phases (E1 40%, E2 50% and E3 70% cycling power). Between sessions E2 and E3, the subjects

rested and left the bike. Sweat samples were collected from the back at different times (first sample at 15 min and the following ones every 10 min) following the same methodology as in section 5.2.2.

The results shown below were mainly gathered during the final session, where several difficulties found in the previous sessions had been worked out. During this session, a trained male conducted a cycling session, adhering to the previously outlined protocol. Additionally, upon concluding the session, supplementary tests were conducted to assess the impact of environmental temperature variations, extending the experimental duration by an extra 10 minutes. Initially, a fan was positioned to direct air towards the participant's back. Subsequently, this setup was replaced by a heater to observe the influence of altered thermal conditions.

7.2.2. Sweat analysis and results interpretation

A prospective study was carried out that included the real-time measurement of the different target analytes with the wearable device and the collection of sweat samples. These were further analysed at CHUV laboratories using the LAQUAtwin commercial sensor devices for pH, Na^+ and K^+, with the aim to establish reference concentration values, detect trends and correlations in variations of the target analyte concentrations and validate the wearable device developed in this work.

To interpret and understand the results, statistical tests were employed:

- *t*-Student test for paired samples. This statistical test was used to determine if there was a significant difference between the mean values of two related groups. By computing the t-statistic value, it assessed whether the mean values of paired observations were significantly different from each other.
- Mixed model analysis of variance or ANOVA test. This test allows simultaneous comparison of more than two sets of data based on the identification and estimation of the sources of variation (factors)

influencing the experimental results. This test was used to assess whether the mean values of the groups were significantly different from each other. Different variants were employed depending on the purpose: One-factor ANOVA, two-factors without replicates, and two-factors with replicates.

- Tukey's honest significance test. This is a single-step multiple comparison procedure and statistical test. It was used after determining that the mean values of the groups were significantly different from each other, to find which groups had a major weight on that difference.

To determine the accuracy of the data collected with the on-body wearable platform, correlations between ISFET sensor measurements and ISE measurements were established in scatter plots. If the results were not statistically different at 95% significance level, linear regression comparing both methods should yield a straight line showing a slope close to 1 and an intercept close to zero, with a regression coefficient higher than 0.99. Additionally, the presence of a systematic bias was assessed by the encompassing of 0 in the CI.

7.3. RESULTS AND DISCUSSION

7.3.1. Factors affecting an athlete's sweat composition

Sweat samples were collected to assess the influence of parameters such as the collection body part, day of the session, effort intensity of the stage and hydration status in Na^+ and K^+ concentration values. The concentration values produced by these samples are detailed in Table A.1 in Annex 1. Statistical analyses were performed using Student's t-test and ANOVA test, where the significance level was set at $\alpha = 0.05$.

First, the influence of the position of the absorbent collection pad was studied. Data was segregated based on the body area where samples were

collected. After averaging results across effort stages and sessions, a notable 20% variation was observed in the concentrations of each target analyte. This variation was closely examined to determine the optimal location for the sweat patch.

Comparative analysis using the paired *t*-test on Na^+ and K^+ concentrations collected from symmetrical positions on the body revealed no significant differences (t_{calc} 0.99 < t_{crit} 2.13 for both Na^+ and K^+). Consequently, the data from these symmetric positions could be combined.

A one-way ANOVA was employed using sessions and efforts as replicates to examine whether the positioning of the patch contributed to variances in Na^+ and K^+ concentrations. The F-statistic and the corresponding F-critical values obtained from both analyses are outlined in Table 7.1. The higher F-statistic values in comparison to the F-critical values enabled the rejection of the null hypothesis, suggesting that distinct Na^+ and K^+ concentrations were identified depending on the placement of the absorbent patch.

Table 7.1. ANOVA test results from the comparison of the data classified based on its origin, determined by three factors (position of the absorbent, session, and effort phase).

	Na^+ conc			K^+ conc		
	F_{calc}	**F_{crit}**	**Significant?**	**F_{calc}**	**F_{crit}**	**Significant?**
One-way ANOVA using sessions as replicates:						
Position	**20.24**	2.39	Yes	**29.69**	2.39	Yes
One-way ANOVA using effort phases as replicates:						
Position	**23.11**	3.11	Yes	**25.42**	3.11	Yes

To determine the most suitable patch location for on-body testing and ensure the acquisition of reliable information regarding the athlete's physiological state, a post-hoc test was conducted. Tukey's honest significance test was applied to the dataset, utilizing both sessions and efforts as replicates. Table 7.2 displays the mean concentration absolute differences ($|\hat{x}_1-\hat{x}_2|$) and the corresponding T_{crit} values derived from these tests (T_{crit}_S and T_{crit}_E). From these results, it could be confirmed that nearly all the

samples compared with the ones collected from the torso or the arms indicated significant differences in both Na^+ and K^+ concentration means. To visually depict the variations among body areas, the mean concentrations from different parts were represented in Figure 7.3a and Figure 7.3b. The connecting segments in the figures indicated significantly different groups, with their lengths reflecting the magnitude of differences observed. Notably, all pairs exhibiting significant differences had torso and arms regions in common, being their mean values highly related with large segments to the other mean values. In conclusion, the samples collected from the torso and arms did not accurately represent whole-body sweat. This effect may be related to poor adhesion, likely attributed to hair presence and potential sweat contamination. Thus, these areas were discarded for on-body testing.

The samples from other locations, including front, upper back, scapula and lower back, exhibited similar concentration values for Na^+ and K^+ target analytes. A closer examination revealed that the variability among the samples, quantified as the standard deviation, was notably lower for the lower back samples. Furthermore, high sweat rates were observed in this location (0.85 ± 0.41 mg cm^{-2}) [18]. Therefore, the lower back was selected as the preferred location for conducting on-body prototype tests.

Table 7.2. Results from Tukey's honest significance test applied to identify which specific pairs of body parts exhibit significantly different sweat sample Na^+ and K^+ concentrations.

	Na^+ conc				K^+ conc			
Pair	$\lvert\hat{x}_1 - \hat{x}_2\rvert$	T_{crit_S}	T_{crit_E}	**Significant?**	$\lvert\hat{x}_1 - \hat{x}_2\rvert$	T_{crit_S}	T_{crit_E}	**Significant?**
Front (P1) & Torso (P2-P3)	**14.0**	8.8	9.4	Yes	**1.8**	0.8	1.0	Yes
Front (P1) & Arms (P4-P5)	**14.5**	8.8	9.4	Yes	**1.4**	0.8	1.0	Yes
Front (P1) & Upper back (P6-P7)	0.6	**8.8**	**9.4**	No	0.4	**0.8**	**1.0**	No
Front (P1) & Scapula (P8-P9)	3.5	**8.8**	**9.4**	No	0.4	**0.8**	**1.0**	No
Front (P1) & Lower back (P10-P11)	7.1	**8.8**	**9.4**	No	0.7	**0.8**	**1.0**	No

Torso (P2-P3) & Arms (P4-P5)	**28.5**	8.8	9.4	Yes	0.4	**0.8**	**1.0**	No
Torso (P2-P3) & Upper back (P6-P7)	**13.4**	8.8	9.4	Yes	**2.2**	0.8	1.0	Yes
Torso (P2-P3) & Scapula (P8-P9)	**17.5**	8.8	9.4	Yes	**2.2**	0.8	1.0	Yes
Torso (P2-P3) & Lower back (P10-P11)	**21.1**	8.8	9.4	Yes	**2.5**	0.8	1.0	Yes
Arms (P4-P5) & Upper back (P6-P7)	**15.1**	8.8	9.4	Yes	**1.8**	0.8	1.0	Yes
Arms (P4-P5) & Scapula (P8-P9)	**11.0**	8.8	9.4	Yes	**1.9**	0.8	1.0	Yes
Arms (P4-P5) & Lower back (P10-P11)	7.3	**8.8**	**9.4**	No	**2.1**	0.8	1.0	Yes
Upper back (P6-P7) & Scapula (P8-P9)	4.1	**8.8**	**9.4**	No	0.0	**0.8**	**1.0**	No
Upper back (P6-P7) & Lower back (P10-P11)	7.8	**8.8**	**9.4**	No	0.2	**0.8**	**1.0**	No
Scapula (P8-P9) & Lower back (P10-P11)	3.6	**8.8**	**9.4**	No	0.0	**0.8**	**1.0**	No

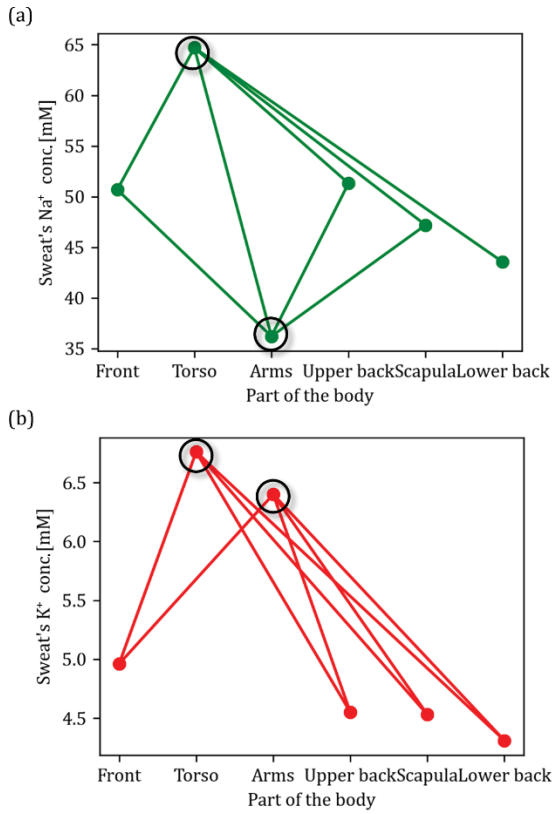

Figure 7.3. Average Na^+ (a) and K^+ (b) concentration values in sweat collected from different sessions and effort stages, grouped into the parts of the body from which they were extracted, with significant differences represented using segments (95% confidence).

Next, the dataset excluding sweat data from the arms and torso was sorted based on the sessions and effort phases. The mean concentrations of Na^+ and K^+ are visualized in Figure 7.4a and Figure 7.4b. Both Na^+ and K^+ had notable day-to-day variability. Factors such as hydration levels, the intensity of the exercise, environmental conditions or dietary intake may have a significant impact on sweat content [28]. On the other hand, while there was no considerable variability in Na^+ concentration among the different effort stages, there was a noticeable decrease in K^+ concentration during certain sessions. Despite that some trends could be distinguished, the influence of the session day and the effort phase on the target analyte was statistically assessed using a two-way ANOVA. The specific values of the F-statistic and

their corresponding F-critical values are detailed in Table 7.3**¡Error! No se encuentra el origen de la referencia.**.

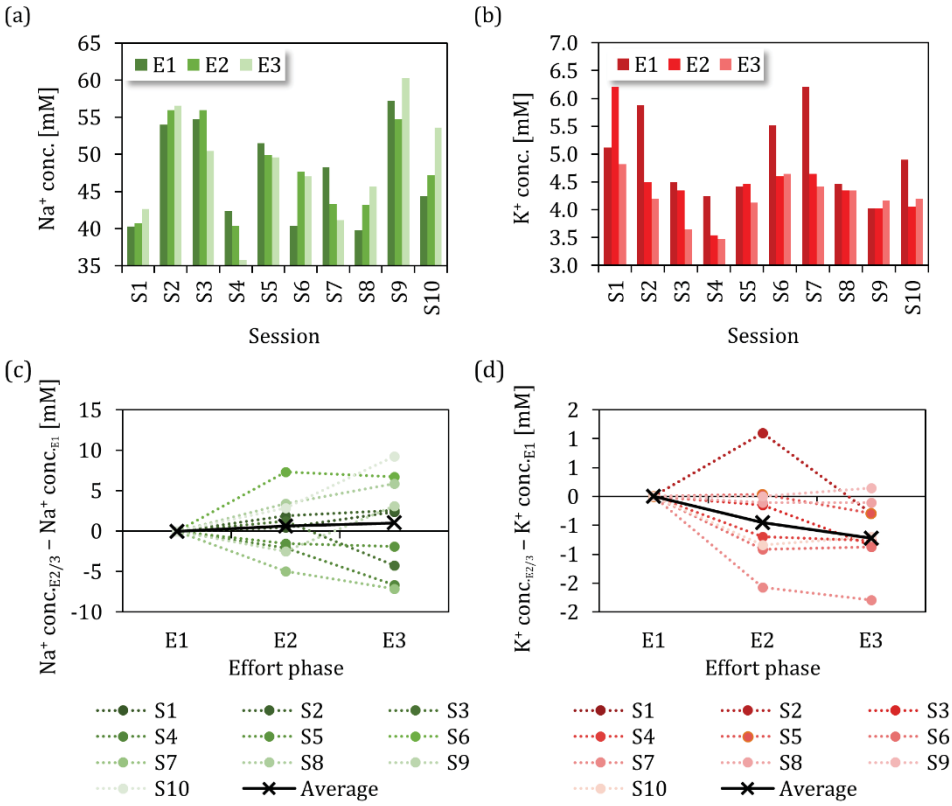

Figure 7.4. Average Na^+ (a) and K^+ (b) concentration values in sweat collected from different parts of the body, grouped by sessions and effort stages. Na^+ (c) and K^+ (d) concentration changes respect E1 for the ten sessions.

Table 7.3. ANOVA test results from the comparison of the data classified based con the day of the session and the effort phase when the samples were collected.

	Na^+ conc			K^+ conc		
	F_{calc}	**F_{crit}**	**Significant?**	**F_{calc}**	**F_{crit}**	**Significant?**
Two-way ANOVA using parts of the body as replicates after removing torso and arms data:						
Session	**9.60**	1.99	Yes	**14.25**	1.99	Yes
Effort phase	0.09	**3.10**	No	**23.12**	3.10	Yes

The results revealed significant variations in the concentrations of both target analytes across different days or sessions, as anticipated from Figure 7.4a and Figure 7.4b. This information was useful to avoid seeking reproducibility across days during the on-body tests. Additionally, discernible differences were observed in the concentrations related to the impact of different effort phases. While Na^+ concentration displayed relatively consistent behaviour throughout the session phases, K^+ concentration exhibited significant variations. Upon calculating the differences between phases E2 and E3 in comparison to E1, it was observed that the average variation in Na^+ concentration along the session was slightly positive, whereas for K^+ concentration, it was notably negative. These trends are depicted in Figure 7.4c and Figure 7.4d, indicating an anticipated pattern in the prototype on-body tests.

Finally, the sessions were categorized into hydrated and non-hydrated sessions. To understand the potential influence of an athlete's hydration level on the concentrations of Na^+ and K^+ in sweat, the data from each specific session, aggregated from symmetric body positions, was subjected to two-way ANOVA analysis. The factors evaluated were the hydration status and the effort phase. The F-statistic and corresponding F-critical values are outlined in Table 7.4. Again, a distinct behaviour was observed in Na^+ and K^+ concentrations. The hydration status appeared to significantly impact Na^+ concentration, suggesting its potential use as a biomarker for assessing an athlete's hydration status. This finding was highly remarkable as it brought us to a close step in accomplishing our objectives with the developed wearable platform. By contrast, the K^+ concentration was hardly affected in spite of showing in the previous analysis that the K^+ levels were notably influenced by the effort phase.

Table 7.4. ANOVA test results from the comparison of the data classified based on the hydration status and the effort phase when the samples were collected.

	Na^+ conc			K^+ conc		
	F_{calc}	**F_{crit}**	**Significant?**	**F_{calc}**	**F_{crit}**	**Significant?**
Two-way ANOVA using sessions and symmetric parts of the body as replicates after removing torso and arms data:						
Hydration status	**5.13**	3.92	Yes	1.69	**3.92**	No
Effort phase	0.06	**3.08**	No	**9.57**	3.08	Yes

To visualize data distribution from both hydrated and non-hydrated sessions, the box plots in Figure 7.5a and Figure 7.5b were employed. These boxes illustrated the interquartile range, enclosing 50% of the data points around the median. Analysing Na^+ concentrations, the box plots for hydrated sessions demonstrated smaller boxes, suggesting lower data dispersion. Moreover, they revealed a discernible positive trend across the sessions, consistent with our previous observations. This trend could imply a direct association between Na^+ concentration and fluid loss. In contrast, non-hydrated sessions did not exhibit a clear trend. As a result, the reported correlation between fluid loss and Na^+ concentration appears could be identified in hydrated sessions but lacked sufficient weight to be statistically significant.

When studying the K^+ concentration boxplot, again the hydrated values showed less dispersion. However, in this case, we observed a decrease in the concentration in both the hydrated and non-hydrated sessions. Further investigation was conducted during on-body tests.

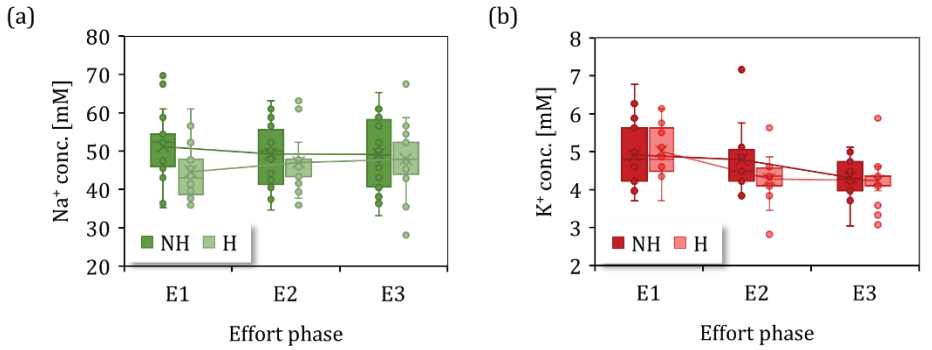

Figure 7.5. Box plots of the Na^+ (a) and K^+ (b) concentrations during hydrated (H) and non-hydrated (NH) sessions. Each data point corresponds to a part of the body (averaging symmetric positions) during a specific session. The data distribution is shown in quartiles around the median values, which are denoted by crosses. The lower and upper limits of the boxes indicate the first and third quartiles of the data. The whiskers represent the lower 25% of scores and the upper 25% of scores. Any data points located outside the whiskers of the box plots are considered outliers. Additionally, segments connect the average values of each type of session (H and NH) in each effort phase.

7.3.1. On-body evaluation of the wearable patch-like device

Volunteers conducted several sessions following the protocol outlined in section 7.2.1 to validate the developed wearable prototype (Figure 7.6a). During the prototype testing, we encountered some issues that needed to be solved for optimal device performance.

Throughout the sessions, we consistently observed sudden random fluctuations in potential signals, impeding the conversion of these signals into meaningful concentration values. An illustrative example is provided in Figure 7.6b. The sources of this undesirable noise were all from external conditions and varied, yet we could detect and eliminate them across the sessions. These sources were the following:

- *Sweat in the ZIF connection (Figure 7.6c)*: The gold contacts in both the patch and ZIF connector became damp, disrupting the electrical signal. This issue was mitigated by covering the connection with impermeable tape.

- *Loosening of the USB C-type connector due to movement (Figure 7.6d)*: The metal connection became slack, resulting in a weak link to the laptop. This problem was addressed by securing it with tape.
- *Electronic interference from other devices (Figure 7.6e)*: Differences in the electrical grounding of other devices placed on the athlete's body altered the potential signal recorded by our device. Identification and subsequent shutdown of these interfering devices resolved this issue.
- *Saturation of the sink pad with sweat (Figure 7.6f)*: The insufficient evaporation rates led to the accumulation of sweat, saturating the microfluidic components. The PE sink pad proved insufficient in absorbing all the accumulated sweat, which surpassed the expected levels based on reported information about the exercise-induced sweat rate [21]. Consequently, in addressing the saturation problem with the sink pad, research efforts were conducted to explore alternative materials to replace PE.

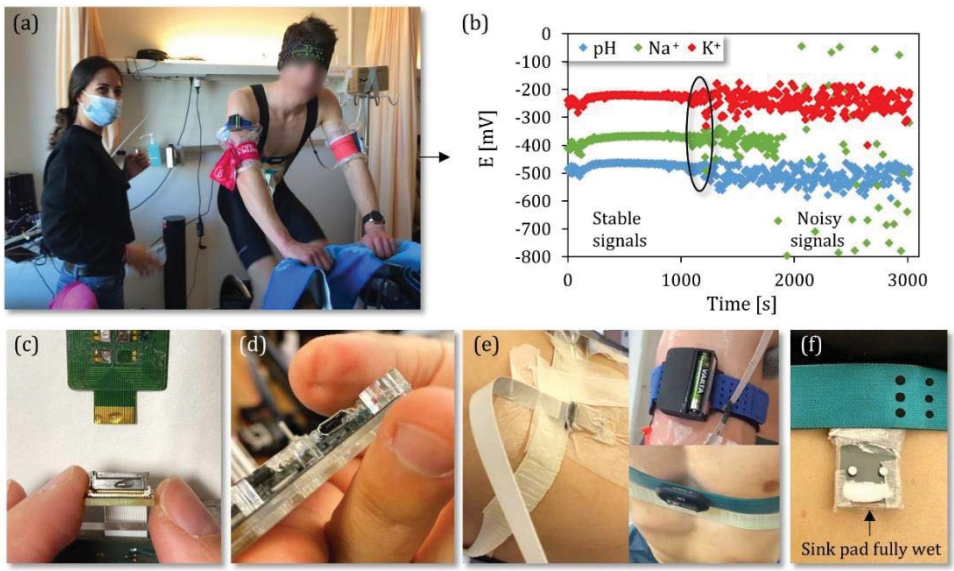

Figure 7.6. (a) Image of an exercise session for patch's on-body tests. (b) Potential recordings from pH, Na^+ and K^+ ISFETs during an on-body test, indicating when the signal started fluctuating due to external interference. (c) Sweat drops in the ZIF connection from readout electronics to the patch. (d) Loosen USB C-type connector. (e) Devices located on the athlete's body that could interfere electronically with our

device's signal. (f) Wearable patch located at the back with microfluidic components saturated with sweat.

We found a material capable of absorbing large quantities of sweat. That was the superabsorbent sodium polyacrylate (SAP). SAP was evaluated as an absorbent for sweat evacuation. It was firstly tested by placing a small amount (1 g) inside a tea bag (Figure 7.7a) and immersing it in an artificial sweat solution for 1 hour (Figure 7.7b). The powder exhibited a remarkable absorption capacity, being able to absorb up to 10 times its volume and 45 times its weight, as illustrated in (Figure 7.7c).

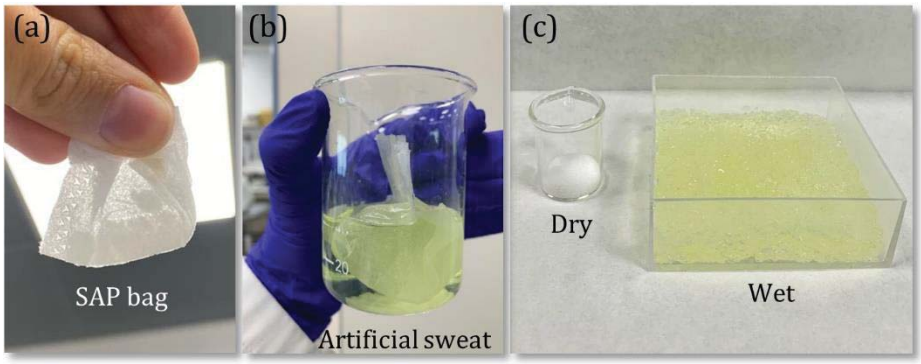

Figure 7.7. (a) Image of the small amount of SAP (1 g) inside a tea bag. (b) Image of the tea bag immersed in artificial sweat solution. (c) SAP powder before and after its immersion in artificial sweat solution.

After solving all issues, the patch was tested on-body for 85 minutes of cycling session with increasing exercise intensity, as described in section 7.2.1. Before the application on the subject's back, the integrated sensors were calibrated with three calibration solutions prepared in artificial sweat. The sensors were calibrated again after each session. ISFET sensors potentials were recorded during the session, and discrete concentration values were computed via interpolation using the post-session calibration plots. Moreover, collected sweat samples were analysed with the commercial LAQUAtwin commercial ISEs.

The wearable patch provided measurements at a 10-s frequency. As illustrated in Figure 7.8, this allowed us to monitor fluctuations in pH, as well

as Na^+ and K^+ concentrations throughout the session. By contrast, the measurements obtained from commercial ISEs represented the cumulative sweat content collected every ten minutes. To validate the performance of the wearable device, we followed two methods:

- A comparison between the ISE measurements and the discrete concentration values extracted from the ISFET sensor recordings with the wearable patch selected to match the time of sweat sample collection.
- A comparison between the ISE measurements and the mean concentration values obtained with the ISFET sensors in the patch during the 5 minutes before the sweat sample collection. The mean concentration values are depicted in Figure 7.8 as bars.

In order to quantitatively compare the methods, the relative differences in their determinations were calculated using the values provided by the ISEs as the reference. The percentage errors resulting from the use of both discrete and mean ISFET concentrations are depicted in Figure 7.9. The mean percentage error across the samples, referred to as bias, together with the CIs, are represented as lines in the plot for each biomarker.

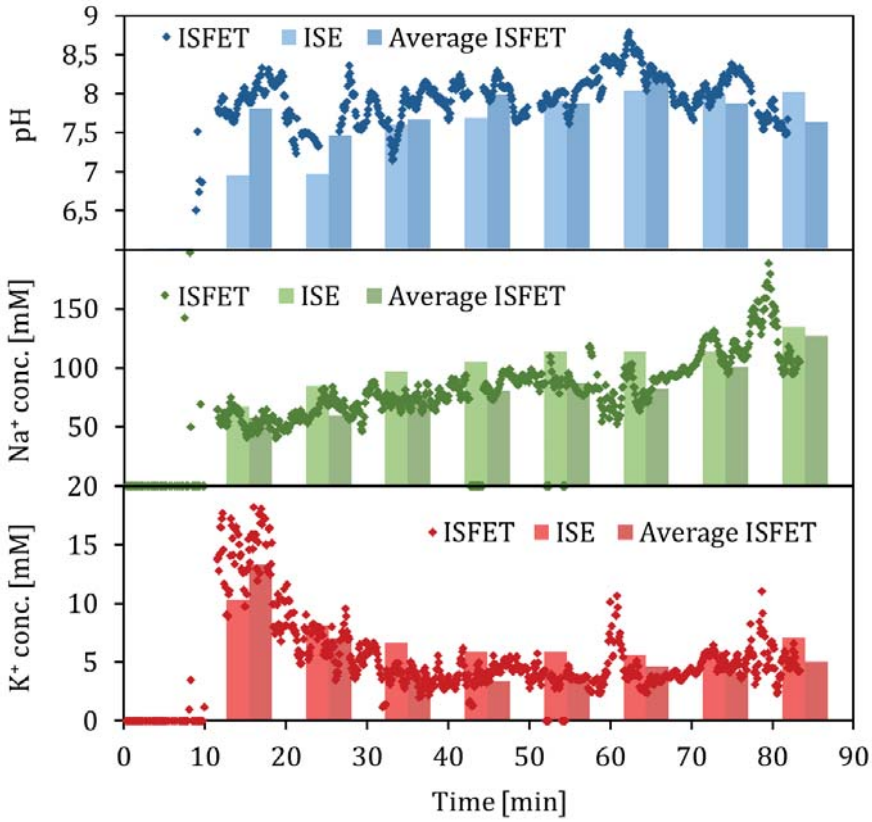

Figure 7.8. pH and Na^+ and K^+ concentration values acquired during the session through three distinct methods: discrete values derived from each recorded potential value using ISFETs, values computed by averaging ISFETs data collected over the 5 minutes before sample collection, and values obtained from commercial ISEs through sweat sample determinations collected every 10 minutes.

Upon examining the pH results, we noted low relative errors, most of them < 10%. Average percentage errors as small as 3.5% and 2.6% were calculated from discrete and averaged ISFET values, respectively. As both of them included the 0 value within the 95% CIs (-2.4 – 9.3% for discrete and -2.0 – 7.2% for average values), we could conclude that the ISFETs determination was not biased. Regarding the comparison between both methods, although the average errors showed a close similarity, differences in precision were visible. The errors derived from discrete values exhibited

some variability, while the majority of errors from averaged data fell within the established confidence interval.

The comparative study carried out in the measurement of Na^+ concentrations provided similar conclusions to the ones obtained in the ISFET validation in sweat samples, previously described in section 5.3.2. The calculated mean relative errors were -17.3% for discrete values and -20.3% for averaged values, and the 95% CIs fell below 0 (-31.7 – -2.9% for discrete and -27.4 – 13.1% for average values), indicating the presence of systematic errors. In this scenario, and unlike measurements performed for the other biomarkers, the averaged data exhibited a higher relative error. The subsequent analysis confirmed this behaviour.

Finally, K^+ ISFET's concentrations exhibited mean biases of -24.7% using discrete values and -21.1% using averaged data. Once more, the 95% CIs did not encompass 0 (-37.8 – -11.6% for discrete and -39.6 – 2.6% for average values), indicating a bias in the K^+ determination.

As previously described in section 5.3.2, the systematic error observed in Na^+ and K^+ determinations was likely attributable to the matrix interference with the ion-selective polymeric membranes. This could be solved by a deep study of the membrane composition optimizing the polymer or can be treated by machine learning tools and neuronal networks, correcting the signal after training.

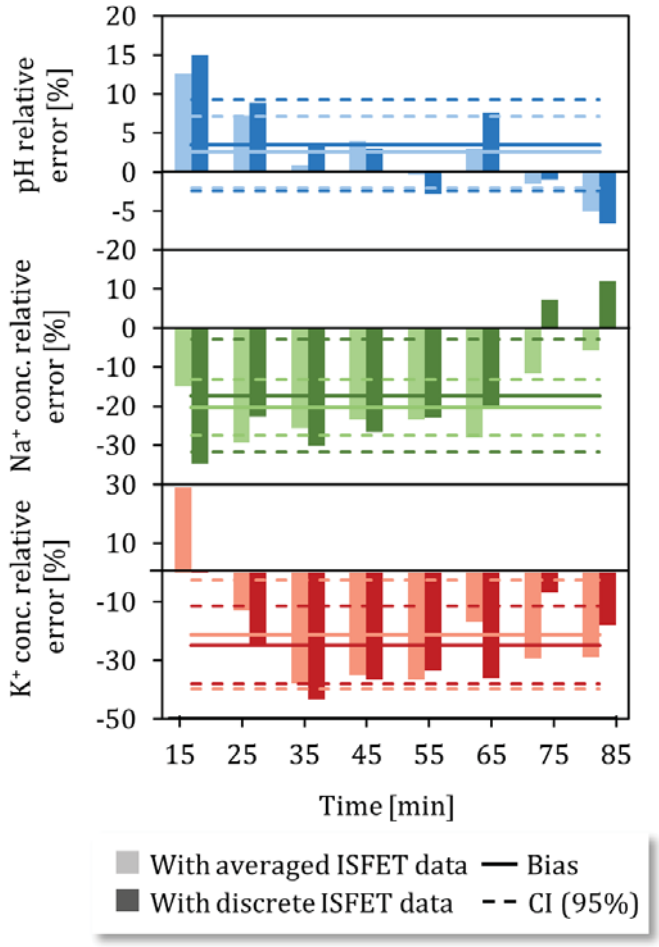

Figure 7.9. Relative errors in pH, Na^+ and K+ concentrations determined from the recorded potentials of the ISFET sensors at the instant when the sample collection pad was taken from the back and the average of the data recorded by ISFETs over the 5-minute time span before sample collection.

Data from both comparisons was also represented in scatter plots to quantify the degree of correlation between the two potentiometric methods. The plots are depicted in Figure 7.10. Upon comparing the pH results with the reference values acquired from the commercial ISEs, a modest correlation was apparent in the averaged data (R^2 0.2738). In contrast, discrete data exhibited a lack of correlation with the ISEs (R^2 0.0598), in accordance with the previously observed dispersion (Figure

7.10a). Given the narrow pH range in sweat samples (pH 7-8.5) and the limited number of samples, even a slight dispersion in the data significantly impacted the regression parameters. Hence, the significance of the correlation magnitude was deemed of lower relevance compared to the relative error when assessing the pH ISFET applicability in on-body measurements.

The Na^+ ISFET sensor data exhibited a strong correlation with the ISE data, as can be observed in Figure 7.10b. However, the presence of the systematic bias mentioned above was evident from the regression curve's intercept, significantly deviating from 0. Although a higher correlation of the ISE data with the ISFET averaged data was obtained than that with the ISFETs discrete values, a higher relative error was observed in the former. This behaviour can be elucidated by examining the scatter plot, revealing that the increased dispersion in discrete values resulted in a calculated lower average error. Upon calculating the relative error with absolute differences, we obtained absolute relative errors of 22.1% for discrete values and 20.3% for averaged values. Consequently, despite the higher bias observed with the averaged values, they exhibited greater precision and a better correlation with the ISE measurements.

K^+ determination was also assessed, displaying a notably improved correlation with the reference values compared to that studied in the off-body validation discussed in section 5.3.2 (Figure 7.10c). Notably, the concentrations estimated with the ISFET sensors found in sweat samples encompassed a broader range than those analysed in the flow system (3.9 – 13.9 mM > 6 — 8.6 mM), thereby mitigating the impact of dispersion on the Pearson correlation. Regarding the ISFET data, while discrete values attained a more robust linear regression, mean concentration data exhibited a strong correlation with the ISE measurements, as indicated by Pearson correlation.

In summary, by averaging the concentration values of the different biomarkers obtained from the ISFET sensor recordings during the 5 minutes before sampling, we attained stronger correlations with the concentration values estimated with the commercial ISEs. This is consistent with the fact that the ISE measurements were performed with samples that combined all the sweat excreted during 5 minutes before collection. Additionally, the on-body performance of the wearable patch-like platform was validated, enabling the quantification of pH, Na^+, and K^+ concentrations in situ with accuracies of 2.6%, -20.3%, and -21.1%, respectively.

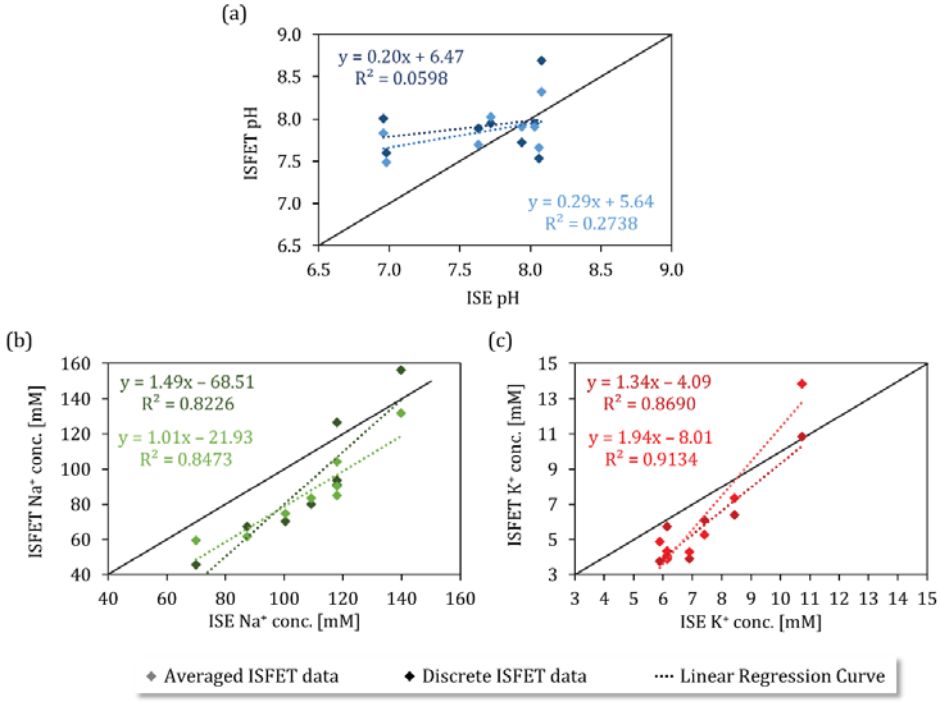

Figure 7.10. Scatter plots showing the correlations between discrete and averaged values obtained from ISFETs monitoring and discrete values from ISEs determination for (a) pH, (b) Na^+, and (c) K^+ concentrations, following Pearson regressions.

Following the validation of the ISFET sensor performance integrated into the wearable device, we could state that our approach enables the analysis of the biomarker concentration trends during the exercise session by recording signals with the integrated readout electronics with a 10-

second sampling rate. In contrast to the measurements carried out with the commercial ISEs, our device facilitated real-time detection of changes, being of potential use for anticipating and preventing in-field body injury.

The variations in sweat biomarkers' content throughout the session were examined hereafter. Figure 7.11 displays the interpolated concentration values, together with the recordings of the skin temperature, the cycling power and the heart rate across varying exercise intensities during the session. The moments where some external factors might have influenced the measurements, such as the subject getting off the bicycle or being exposed to a fan or a heater, have been tagged. This study was designed to prompt higher sweat rates throughout the session to establish correlations between sweat rate and the assessed biomarker concentrations. To achieve this, instead of maintaining a consistent intensity level throughout the session, as in prior on-body sessions, the bike power was incrementally adjusted from 40% MAP (E1) to 70% MAP (E3). The data gathered from this test was meticulously analysed. First, it was noted that the sensors started responding consistently after 12 minutes, during the warm-up period. This duration encompassed a phase when the athlete did not start sweating and the time delay was attributed to the capillary-based microfluidics. Subsequently, the pH and Na^+ sensor signals stabilized, and sweat was sampled to be analysed off-body using commercial ISEs. Initially, concentrations of 55 mM Na^+, 16.5 mM K^+, and a pH of 7.9 were calculated. A higher K^+ concentration than the expected one was observed, potentially indicating skin contamination, a common occurrence reflected by unusually high K^+ concentrations (> 8 mM) [135]. At that juncture, the sample volume was minimal, making any electrolyte leached from the skin's stratum corneum disproportionately impactful on the sample ion concentration. The K^+ concentration reverted to typical concentration levels (2 – 8 mM) [136] during the warm-up stage.

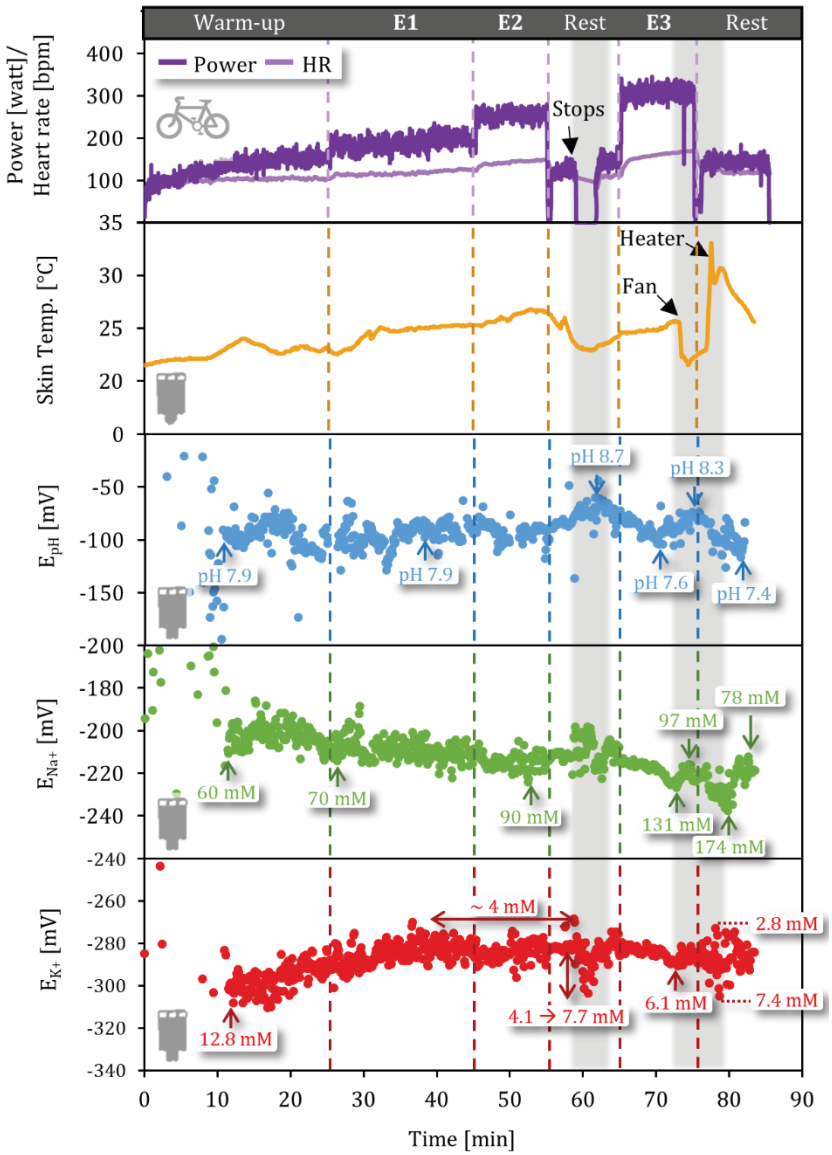

Figure 7.11. Testing with the wearable patch on an athlete during ergocycle exercise at different exercise intensities (warm-up, E1, E2, E3 and rest). Recordings include cycling power, heart rate, skin temperature and pH, Na^+ and K^+ ISFETs concentration values interpolated potential signals. Sweat biomarkers concentrations changes at different moments are labelled. Grey areas define time periods influenced by some external inputs.

During E1 and E2 stages, skin temperature rose from 23 to 26.8°C due to the power increase, while pH remained relatively constant. Once a substantial sweat rate was achieved (midway through E1), the K^+

concentration stabilized (~ 4 mM) until external conditions changed, as expected [137]. At that point, the pH also stabilized at a 7.9 value, indicating proper sample flow within the microfluidic component to reach the pH ISFET gate. Moreover, during E1 and E2 stages, Na^+ concentration steadily increased, from 70 to 90 mM Na^+, as the effort and sweat rate did. These results are in accordance with the extensively reported dependence of Na^+ concentration on sweat rate [9,21].

Between E2 and E3 stages, the subject stopped the exercise and got off the bicycle. This interruption was denoted by a decline in skin temperature (down to 22.9°C), an unsteady Na^+ signal fluctuating from 55 to 118 mM and a sudden increase in K^+ concentration that reached 10.5 mM. These fluctuations were believed to result from the stop of sweat flow, leading to a phenomenon akin to that observed at the initial stage of the monitoring. During that time, the pH increased to pH 8.7, contrary to the expected decrease due to the stop of the sweat flow, as described in [138]. This deviation might be linked to a delay in pH recording, possibly due to slow sweat diffusion in and out of the pH ISFET well. A subsequent decrease down to pH 7.7 was noticed right after, related to the stop in sweat production. Upon the beginning of the E3 stage, the Na^+ and K^+ ISFETs potential values returned to those recorded at the end of E2. Later, both values rose, reaching 131 mM Na^+ and 6.4 mM K^+ owing to the intensified cycling power and, consequently, the higher sweat rate. The pH sensor showed this increase when being in the middle of E3, shifting to 8.4.

At the end of E3, a fan was brought close to the subject to explore the impact of ambient temperature and evaporation on the sensor responses. This led to a sudden drop in temperature (down to 21.5°C), coinciding with a slight decrease in the concentrations of the target analytes. Next, the fan was replaced with a heater and the skin temperature rose up to 30.7°C. Although the ISFET sensor signals were noisier in this scenario, distinct increases in Na^+ and K^+ concentrations were evident, with sudden spikes of

180 mM and 11 mM, respectively. It is important to note that warmer conditions usually correspond to increased sweat rates and ion concentrations. However, existing studies suggest that skin temperature may also affect sweat composition, providing a potential explanation for the observed phenomena [136].

Finally, as the subject recovered from the exercise by cycling at a lower power, a decrease in skin temperature (25.6°C) was noted. Correspondingly, both pH and Na^+ concentration declined until pH 7.5 and 105 mM, respectively. By contrast, the K^+ concentration remained constant at around 4.2 mM, regardless of the sweat flow rate.

7.4. Conclusions

A clinical study was carried out to fully assess the day-to-day, effort intensity and collection position impact on the Na^+ and K^+ ion content in the exercise-induced sweat. The body sampling location and session day exhibited an important influence on the analytical measurements. The lower back was determined to be the body region most representative of whole-body sweat composition, exhibiting a notably high sweat rate. Additionally, variations in the ion content of sweat were noticed when the athlete experienced dehydration, resulting in more scattered data and less distinct trends.

The performance of the wearable patch-like device for on-body monitoring of the selected target analytes was evaluated. A comparison between the continuous data obtained from the sensors within the patch and the limited measurements taken from discrete samples gathered during the session revealed a gap in the information that could be achieved with batch measurements. This confirmed the necessity of the development of a platform able to monitor continuously the ions secreted in sweat during exercise performance. Overall, these results clearly show the potential of our

device for real-time analytical measurements and control of the body condition of an individual practising sports of different intensities in order to avoid potential body injury or other abnormal physiological conditions that may occur.

Some of the results from the on-body session were published in Publication 4 and Publication 6.

8 EXPLORING THE DEVELOPMENT OF A POTENTIOMETRIC CORTISOL APTASENSOR

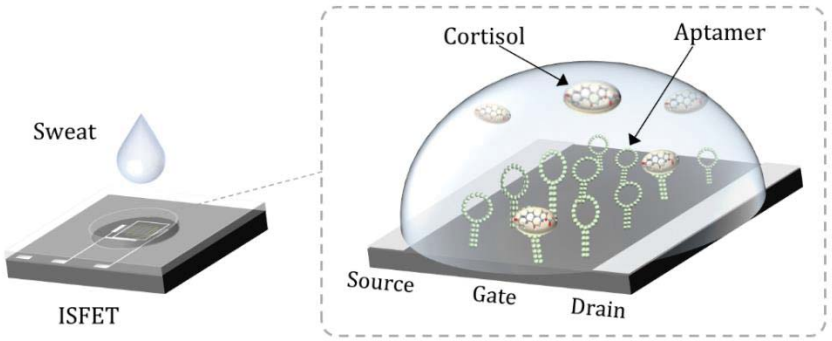

Figure 8.1. Graphical abstract of the preliminary aptaFET for sweat analysis.

8.1. INTRODUCTION

Cortisol, also known as the "stress hormone", is an attractive biomarker for sports medicine. Understanding cortisol fluctuations would help the evaluation of an athlete's recovery and adaptation to training loads, preventing overtraining and promoting optimal performance. Furthermore, persistently elevated cortisol levels could indicate overtraining syndrome or chronic fatigue in athletes, that could be prevented if monitored.[139]

Cortisol is present in various bodily fluids such as blood [140,141], sweat [142], saliva [143], and urine [144]. Its detection in sweat allows for noninvasive monitoring of stress levels. In human perspiration, physiological cortisol levels typically range from 8 to 140 ng/mL[145]. Traditional

methods for cortisol detection have encompassed a range of techniques, including chromatography coupled with mass spectrometry [142], enzyme-linked immunosorbent assay [146], chemiluminescence immunoassay [147], surface plasmon resonance [148], and quartz crystal microbalance [149]. Despite their high sensitivity, these approaches are constrained by their dependence on bulky, complex, and costly instrumentation, as well as the need for skilled personnel [150,151]. Biosensors utilizing FET technology have transformed these laboratory processes into a portable chip format, streamlining the electrical signalling of analyte levels [152].

Electrochemical immunoassays offer several advantages such as high sensitivity, minimal sample requirements, rapid analysis, portability, and cost-effectiveness [153,154], meeting the demands of point-of-care testing (POCT). While conventional methods rely on labels or electroactive indicators for sensitive electrochemical signals, which, although sensitive, involve several steps and can be time-consuming, label-free systems enable swift and straightforward detection. Some representative examples based on mechanical [155], optical [145], and electrical [156] transduction modes have been reported.

Most electrochemical detection approaches for cortisol rely on specific antigen-antibody recognition approaches [157,158]. More recently, aptamers, consisting of small single-stranded oligonucleotides (DNA or RNA) typically comprising 10–100 nucleotides, demonstrate high specificity and affinity for a wide range of target molecules. Aptamers offer distinct advantages over antibodies, including ease of in vitro synthesis using systematic evolution of ligands by exponential enrichment (SELEX), simple chemical modification, cost-effectiveness, and enhanced stability [159,160]. Consequently, aptamers have garnered attention in sensor development as promising recognition elements due to their favourable attributes compared to antibodies, featuring simple chemical synthesis, adaptability for introducing functional chemical groups, superior affinity and specificity,

compact size, high reproducibility, enhanced thermal stability, lack of immunogenicity, and cell-free synthetic production.

This chapter shows very preliminary results on the use of an aptamer for developing a potentiometric sensor on an ISFET device for the label-free selective detection of cortisol. Aptamer FET devices or apta-FETs previously reported and recently reviewed in [161], which made use of potentiometric transduction modes did not show clear responses to cortisol solutions. Here, an aptamer previously reported to bind to cortisol was immobilized on the gate of an ISFET in order to construct a potentiometric sensor device, whose performance was studied under different experimental conditions.

Interaction between cortisol and the aptamer leads to an accumulation of analyte molecules within the electrical double layer (EDL), thereby modulating the dielectric constant. This modulation occurs without an exchange of charges between the electrode and electrolyte, thus being nonfaradaic. The alterations in the interfacial properties due to the reorganization of ions at the EDL may modulate the I_{DS} of the ISFET. The change can be also translated into a change in V_{GS} by taking a fixed I_{DS}. The detection mechanism is schematised in Figure 8.2. However, the analyte interaction with the immobilized aptamer can only be detected when it takes place within the Debye length, which is the distance between the two charged layers in the interfacial charge separation between the electrolyte and the ISFET channel [162,163]. It is known the Debye length is highly influenced by the surface charge flux on the FET gate, which is related to the ionic content of the measuring solution environment [164].

Although the recent advancements hold significant promise for future wearable sensors in sweat analysis, there is not enough experimental data concerning cortisol aptaFETs that comprehensively elucidates their functioning. New experiments and crafting of theoretical models should be carried out to provide deeper insights and explanations for the observed experimental outcomes.[165]

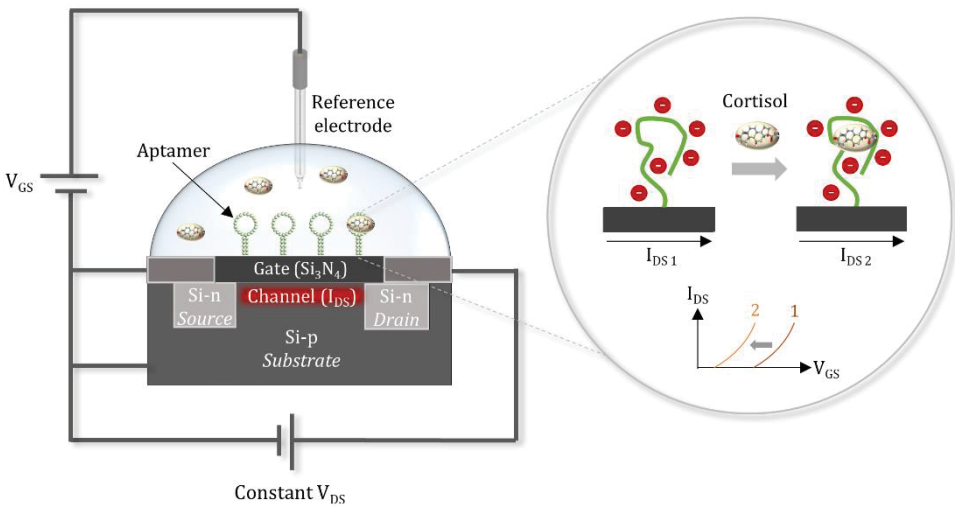

Figure 8.2. Schematic representation of the mechanism of detection of aptamer-modified ISFETs in the presence of cortisol molecules.

8.2. EXPERIMENTAL SECTION

8.2.1. ISFET bio-functionalization

The selected aptamer was used to functionalize the ISFET gate by a silanization process followed by a covalent anchoring step. For this, ISFET chips were thoroughly cleaned with absolute ethanol to remove possible contaminants and then dried under a N_2 stream. Afterwards, they were immersed in a 0.5 M NaOH aqueous solution for 20 min, followed by immersion in a 0.1 M HCl solution for 10 min and a final immersion in 0.5 M NaOH solution for 10 min, rising the chip in between with DI water in order to avoid solution contamination. A final rinsing step was carried out in 0.1 M HCl and DI water, followed by a drying step in an oven at 120 °C for 10 min [166]. Then, the cleaned surfaces were silanized by adding 10 µL of the TESUD ethanolic solution and leaving them untouched for 30 min at room temperature. Next, the surfaces were rinsed twice in absolute ethanol and dried in an oven at 100 °C for 1 h to dehydrate their surface completely, and

thus, induce the formation of stable siloxane bonds. Finally, in all cases, the substrates were rinsed with absolute ethanol and dried under a N_2 stream [57].

Subsequently, the silanized gate surfaces were incubated at 4 °C overnight with a drop of 100 μM cortisol aptamer solution followed by the rapid addition of the 5 μL of a 5 mM $NaBH_3CN$ solution in PBS. During the incubation, the TESUD and the aptamer get covalently bonded through the formation of an imine group. Next, the surfaces were rinsed once with 1 % BSA (w/v), before being rinsed twice with DI water. (based on [57,167]

The aptamer oligonucleotide sequence is purchased as a linear sequence to which the required secondary structure for target analyte recognition should be induced. For this, the functionalized chip was heated at 70 °C for 1 min and then cooled to room temperature by immersion in the cortisol binding buffer (CBB).

The thus-fabricated sensors were stored at 4 °C, until use. When being in use, they were kept under wet conditions in a PBS solution in between measurements to retain the aptamer secondary structure.

The steps involved in the ISFET modification with the aptamer are summarized in Figure 8.3.

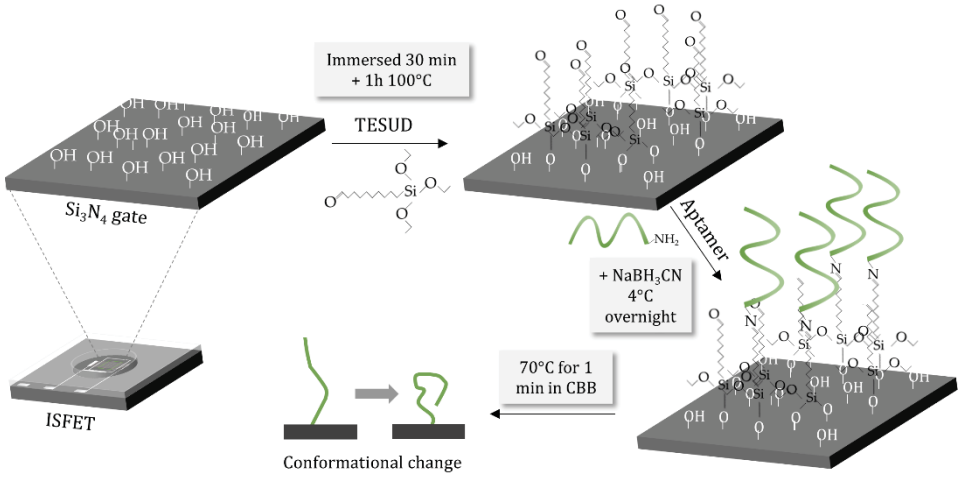

Figure 8.3. Schematic representation of the steps involved in the aptamer functionalization of the pH ISFET's gate.

8.2.2. Aptasensor characterization

Various tests were conducted to monitor the effectiveness of each step involved in the modification of the ISFET, the matrix effect, and to assess the aptasensor capacity to respond to changes in cortisol concentrations. When characterizing the electrical properties of the aptasensors, the I_{DS}-V_{GS} curves were recorded with the virtual ISFET meter (described in 3.4.2) in a range of V_{GS} from -1.5V to 1.5V, fixing the V_{DS} at 0.5V.

8.2.2.1. Surface silanization evaluation

Different protocols have previously been reported for TESUD silanization of Si_3N_4 surfaces [57,58]. Two treatments were compared with the two solutions mentioned in the previous section. During this process, the silanol groups of the TESUD silane condense with the silanol groups present at the ISFET gate, as outlined in 8.2.1. Upon dehydrating the surface by the thermal treatment mentioned above, stable siloxane groups were formed leaving the aldehyde reactive groups on the ISFET gate surface ready for bonding free primary amine groups present in the aptamer.

The effectiveness and homogeneity of the silanization were initially evaluated by immobilizing the TRITC-antibody conjugate and visualizing it by fluorescence microscopy. Primary amine groups of the antibody structure react with the aldehyde groups of the silane to produce an imine that is further stabilized by reduction with $NaBH_3CN$ to produce a stable secondary amine. The fluorophore group chosen to tag the antibody was TRITC, whose excitation ideally suits the 532-nm laser line of the fluorescence optical microscope available in our laboratories.

8.2.2.2. Evaluation of the aptamer immobilization

First, the successful immobilization of the aptamer sequences on the gate area of the ISFET was verified. As explained in section 8.1, the electrical characteristics of an ISFET can be altered due to the presence of charged molecules on its gate. Therefore, the $I_{DS} - V_{GS}$ curves of an ISFET were recorded before and after being silanized with TESUD, and after the aptamer immobilization. The test was performed in a PBS (x0.01) solution.

8.2.2.3. Characterization of the matrix ionic strength effect

As explained in section 8.1, the ionic strength of the buffer solution used for aptasensor measurements holds critical importance. To investigate the Debye-screening effect, an aptasensor's $I_{DS} - V_{GS}$ curve was recorded in solutions containing different electrolyte concentrations: PBS (x1), PBS (x0.1), PBS (x0.01), and PBS (x0.001).

8.2.2.4. Characterization of the aptasensor's sensitivity to cortisol

The aptasensor response to cortisol changes was assessed. Initially, the device's $I_{DS} - V_{GS}$ curve was recorded in the selected background solution (PBS (x0.01) spiked with 5 mM $MgCl_2$). Subsequently, it was placed in cortisol-spiked solutions containing concentrations ranging from 1 nM to 1

μM, these being within the reported cortisol levels in sweat (8 to 141 ng/mL, equivalent to 22 to 386 nM) [145]. After a 30-minute incubation, the sensor was thoroughly rinsed and placed in the measuring cell containing the background solution. $I_{DS} - V_{GS}$ curves in each cortisol-spiked solution were recorded.

8.3. Results and Discussion

8.3.1. Evaluation of the aptamer immobilization process

The aptamer molecule distribution on the sensor surface plays a critical role in the reproducible manufacturing of the sensor and analytical detection of the target analyte. Loosely packed aptamers may lead to poorly sensitive sensors. By contrast, densely packed aptamers can cause steric hindrance by not providing enough space to allow the aptamer to adopt the suitable 3D conformation while interacting with the target analyte, thus resulting in a reduced binding efficiency [168]. The aptamer functionalization degree on the ISFET gate mainly depended on the number of attached organosilane molecules, which was in turn related to the availability of hydroxyl groups at the gate surface. Then, activation of the sensor surface and silanization steps were key to optimize the aptamer density. The surface was initially functionalized with fluorescent antibody conjugates to easily visualize the degree of silane functionalization. The surface coverage was studied through fluorescence microscope imaging.

The composition of the first silanizing solution tested was 5% TESUD and 5% acetate buffer at pH 5.6. The fluorescence images obtained from the samples showed few fluorescent spots and a non-uniform distribution (Figure 8.4a). Some agglomerated molecules indicated this lack of surface homogeneous functionalization.

The following solution tested contained 20% TESUD and did not contain any aqueous buffer fraction. After treating different surfaces using these

conditions and visualizing them under the fluorescence microscope, we could conclude that this treatment provided a more effective silane functionalization showing a more uniform and denser TESUD coverage than the previous tested approach (Figure 8.4b).

ISFETs were then functionalized following this approach and checked under an optical microscope to ascertain that the silanization process did not affect the ISFET sensor packaging and that no agglomerations were visible on the ISFET gate surface (Figure 8.4c).

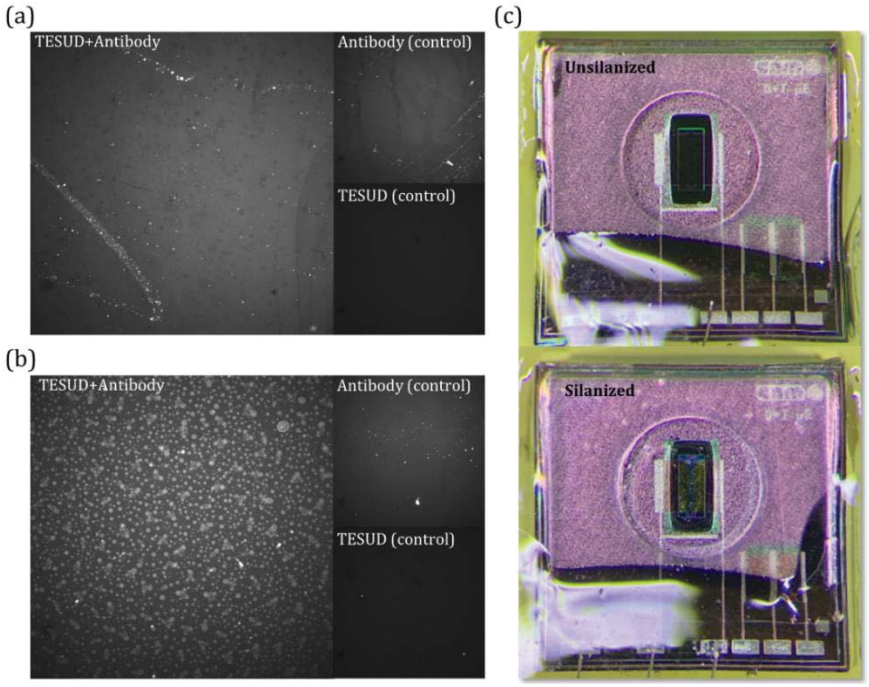

Figure 8.4. Fluorescence images of Si_3N_4 surfaces functionalized with TESUD (control), incubated in fluorescent antibody solution (control) and treated with both TESUD and fluorescent antibody, using two treatments: 5% TESUD + 5% acetate buffer (a) and 20% TESUD (b). (c) ISFET's gate before *(upper)* and after *(lower)* silanization with 20% TESUD.

8.3.2. Aptamer immobilization on ISFET surface

The introduction of highly negatively charged aptamer sequences onto the gate of an ISFET may induce alterations in its electrical properties.

Therefore, to assess the successful binding of the aptamers to the silanized gate surface, the I_{DS} – V_{GS} curve of an ISFET was recorded. As depicted in Figure 8.5, the ISFET I_{DS} showed a minor increase due to the TESUD deposition, but a substantial rise was produced upon functionalization with the aptamer. This discernible change indicates a notable modification of the charge distribution at the device gate due to the presence of the aptamer.

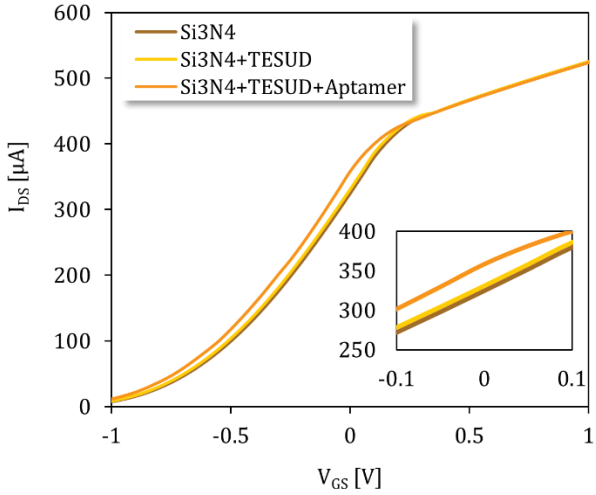

Figure 8.5. I_{DS} *vs* V_{GS} curves of an ISFET before and after the Si_3N_4 gate silanization with TESUD, and after the immobilization of the aptamer.

8.3.3. Debye-screening effect

In order to choose the appropriate buffer solution for cortisol sensing characterization, we must understand how the charges present in the solution interfere with the sensor performance. The different charged layers generated between the ISFET channel and the electrolyte solution are influenced by the ionic strength of the medium. Elevated ion concentrations can potentially result in the shielding of molecular charges away from the gate insulator, a phenomenon called the screening effect. Then, the selected buffer should keep the Debye length thick enough to effectively detect the interactions between the aptamer and the analyte. The detection mechanism

of ISFETs in biosensing applications is briefly explained in section 8.1 and further information can be found in previously reported works [169].

To study the dependence of the aptasensor response on the ionic strength, the I_{DS} was recorded as a function of V_{GS} in PBS(x1), PBS(x0.1), PBS(x0.01) and PBS(x0.001) solutions. In Figure 8.6, we observed a displacement of the V_{GS} toward lower gate voltages. This observed shift is a consequence of the potential gradient across the electrical double layer within the solution. As the ionic strength of the solution increases, the Debye length decreases, consequently amplifying the capacitance of the double layer and reducing the surface potential corresponding to a given surface charge. Consequently, the V_{GS} may shift towards lower gate voltages. The results are consistent with previously reported studies [162].

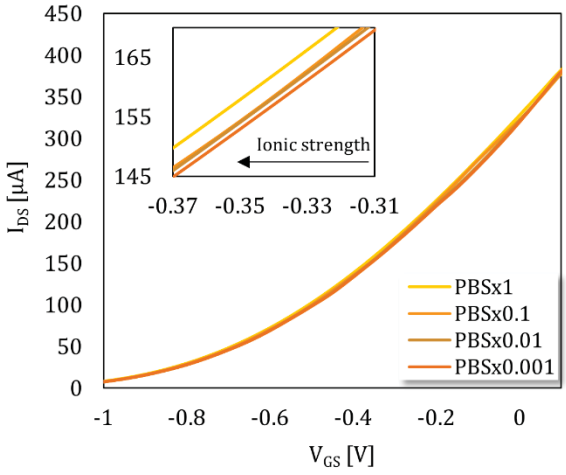

Figure 8.6. I_{DS} – V_{GS} curves of an aptamer-FET in PBS (x1), PBS (x0.1), PBS (x0.01), and PBS (x0.001) matrices.

Previous reports using aptamers in FET devices guaranteed the proper transistor's performance in PBS diluted by x0.01, where the Debye length was estaimated to be ~7.4 nm [162], so this was the chosen background solution. We also added 5 mM $MgCl_2$ concentration to stabilize the aptamer conformation, as the presence of divalent cations can improve the sensor sensitivity to the analyte, as previously reported [170].

8.3.4. Sensitivity to cortisol

The aptasensor response to cortisol was studied using three sensors incubated in the previously defined buffer solution containing cortisol concentrations from 1 nM to 1 μM. After each incubation, their I_{DS} vs V_{GS} curves were recorded in the buffer solution, following the steps outlined in section 8.2.2.3. As observed in Figure 8.7a, the curves shifted towards more negative V_{GS} values when the cortisol concentration increased in solution. Notably, the curves at 100 nM and 1 μM overlapped, which might be an indication of the sensor saturation at these high concentration values. The I_{DS} differences between the different cortisol-spiked solutions and the buffer solution were quantified at a fixed V_{GS} of 0.2V, within the linear range of response of the sensors. They are represented as a graph bar in Figure 8.7b. The saturation at 100 nM was observed in all three aptasensors. A clear relationship between I_{DS} and cortisol concentration is observed. To detect concentration changes exceeding 100 nM cortisol, optimization of the organosilane and aptamer deposition, with increased aptamer density but avoiding steric hindrance, would be necessary.

Finally, V_{GS} values were extracted from each curve at a fixed I_{DS} of 360 μA, within the linear regime performance of the aptasensors. The V_{GS} differences between the different cortisol-containing solutions and the buffer solution were calculated and represented in Figure 8.7c. A linear dependence between ΔV and the logarithm of cortisol concentration was observed within the range of 1 nM to 100 nM, corresponding to a sensitivity of 9.3 mV dec^{-1}, consistent with previously reported study using an aptamer extended gate FET device and a different aptamer [171] (Figure 8.7d).

The aptasensor reproducibility was evaluated based on the standard deviation of the sensitivity. The sensor differed in ± 1.06 mV dec^{-1}, equivalent to 11% of the average sensitivity.

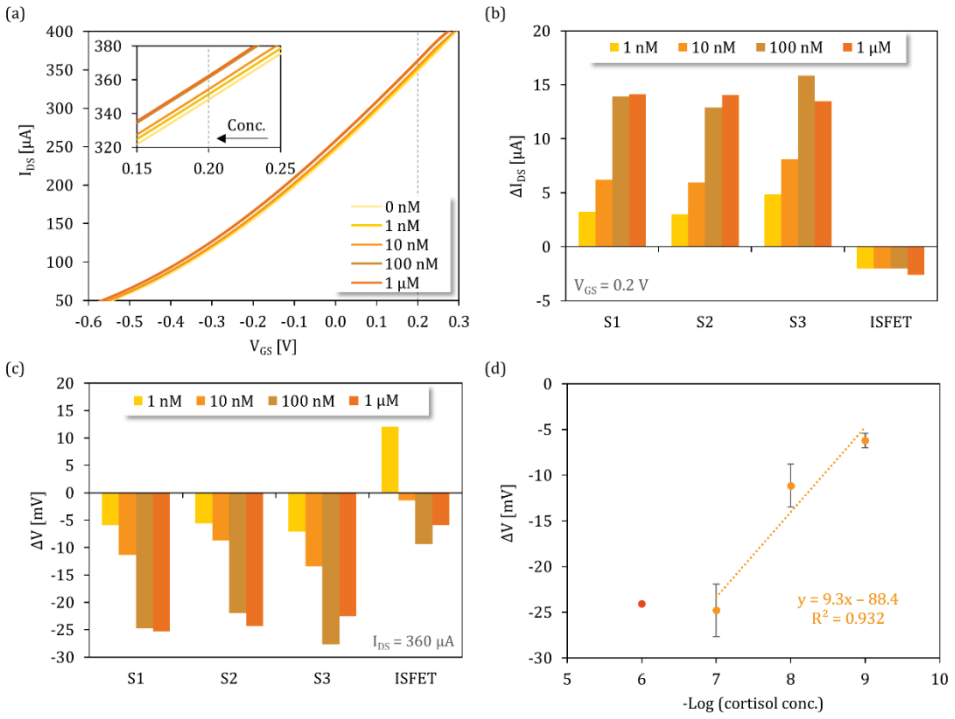

Figure 8.7. (a) I_{DS} vs V_{GS} curves of an aptamer-FET in a cortisol-free solution and 1 nM to 1 µM cortisol solutions. (b) I_{DS} differences between the cortisol-spiked solutions (1 nM – 1 µM) and the buffer solution at a fixed V_{GS} of 0.2 V. (c) V_{GS} differences between the cortisol-spiked solutions (1 nM – 1 µM) and the buffer solution at a fixed I_{DS} of 360 µA. (d) Linear calibration curve of the previous V_{GS} differences against the decades' changes in cortisol concentration.

8.4. CONCLUSIONS

The manufacturing of a potentiometric cortisol aptasensor with the ISFET devices used throughout this thesis work was carried out and characterized. The efficient covalent immobilization of the selected aptamer could be demonstrated. While some response profiles were recorded for different cortisol concentrations upon optimization of several analytical parameters that could affect the sensor performance, no concluding remarks could be set related to the suitability of this sensor configuration for the detection of cortisol in sweat samples. More studies will be required in this direction.

9 Conclusions and Perspectives

9.1. Conclusions

This Thesis has overcome several challenges in the application of ISFET sensors for sweat analysis and implementation in a flexible wearable platform.

1. **Development of (bio)chemical sensors**

   An important effort has been put on the fabrication of ISFET sensors for the detection of the most significative biomarkers present in human sweat, such are Na+, K+, pH, and Cl-. Several innovative technological approaches have been attained including the standardization of the deposition of an encapsulant layer at wafer level and silanization and deposition of membranes onto Si_3N_4 gate ISFETs. ISFET sensors have been manufactured and characterized in standard solutions, exhibiting Nernstian sensitivities, consistent repeatability and reproducibility, and long-term stability within the physiological concentration range in sweat. An in-depth study was carried out to define all the analytical performance characteristics of the Na^+ ISFET sensor, as it is the most relevant of all the studied sweat biomarker that provides direct information about the physiological status related

to hydration of an individual. A joint study carried out with UZH partner from the SNF project has been carried out to assess the applicability of neural networks to circumvent individual sensor calibrations. Furthermore, the development of an potentiometric aptasensor has been explored to show that ISFET devices could potentially be applied for the detection of this cortisol biomarker.

2. **Validation of the sensors for the real-time monitoring of biomarkers in sweat**

   A flow system has been developed that integrate up to XX ISFET sensors, enabling the rapid analysis of sweat samples used for sensor validations outside the wearable platform. Results have been compared with two reference methods. Although good correlations were observed, results revealed a matrix effect on Na^+ and K^+ ISFET sensor performance, which turned out to be more critical for the Cl^- ISFET sensor. A systematic bias was uniformly kept in the analysed samples, indicating a possible interference between the ion-selective polymeric matrices and the lipid-rich sweat content. Further work efforts will have to be invested to correct the bias in the collected data. A more erratic performance has been observed for the Cl- ISFET sensor making it not adequate for its integration in the wearable platform.

3. **Development of a solid-state reference electrode**

   The fabrication of a robust solid-state reference electrode has been key to develop the wearable platform. A thin-film Pt base electrode has been used onto which a Ag/AgCl/PVB layers were deposited. The novelty of this RE relied on the application of a PVB polymer coating that kept NaCl electrolyte on its matrix, preventing any leaching and thus maintaining a constant

potential. This RE demonstrated long-term potential stability, low drift and noise, and robustness. Its planarity allowed its easy implementation into the wearable prototype.

4. **Integration of ISFET sensors into wearable platforms**

   Two patch-like devices integrating the developed sensors have been fabricated and tested. A final design with comprising the sensors aligned on a compact semi-flexible platform was assessed for on body applications. A new encapsulation procedure has been optimized to integrate the chip sensors into the wearable platform. With that, the bonding and the protective layers were kept in perfect conditions after several months of use and stable potentials with a high sampling frequency were recorded, thanks to the use of a custom-made portable multichannel read-out electronics.

5. **Integration of a fluidic component and final design of the wearable prototype.**

   A fluidic component has been integrated in the wearable platform with the purpose of driving the low-volume sweat solutions by capillary action, avoiding dead volumes and ensuring the fast and complete renewal of the sweat from the sensor surfaces. This The fluidic component has been designed so that is required the minimum area to cover all the sensors on the wearable platform and has been made of a polymeric material that favoured rapid capillary action and thus fast uniform sweat flow and renewal to and from the sensor surfaces, respectively. The final wearable platform integrating sensors and paper-like fluidics has s shown to have the required flexibility to be well-

adhered to the skin, demonstrating adequate sweat collection and evaporation rates and thus avoiding sample contamination.

6. **Validation of the wearable prototype on-body and correlation of biomarkers changes with athlete's conditions**
   A clinical study has been performed to choose the best location of the patch in the body.Then, the patch has been used for the continuous monitoring of temperature, pH, and Na^+ and K^+ during a series of static bicycle sessions. An in-depth analysis of the recorded data has been carried out that show the good on-body performance of the integrated sensors compared to that of reference methods. .

From these results, we can conclude that this technological and analytical approach could be of potential use for real-time and non-invasive detection of different sweat biomarkers, greatly facilitating health monitoring of athletes during exercise performance.

Future work

Several hurdles found during the development of this work will require further study.

- **Sweat monitoring of Na^+ and K^+.** Results demonstrated a clear bias in the response of the ISFET sensors during sweat sample analysis compared with reference methods. This is likely to be related with the lipidic content of the sweat that is absorbed in the selective membranes of the sensors. Some alternative solutions could be the following:
  - Since it is a systematic bias, this could be corrected by using chemometric methods or machine learning algorithms. The

latter approach has been studied within the WeCare project and is currently being applied to the analytical data generated during this thesis work. A future paper describing this study is expected to be published in the near future.

  - The study of new membrane compositions regarding having a different polymer matrix to avoid the lipid negative- effect on the sensor performance.

- **Cortisol sensor:** Further tests should be performed in order to get more insight about the performance of the cortisol sensor and its ability to selectively and reversibly respond to concentration changes showing in turn with long-term stability. These are prerequisites for the sensor potential application in sweat cortisol monitoring.
- **On-body tests:** Further on-body tests should be performed to stablish correlations with the biomarkers in blood, and to reach a better understanding of the utility of monitoring sweat composition for carrying out reliable health individual assessment.

References

[1] D.R. Seshadri, M.L. Thom, E.R. Harlow, T.J. Gabbett, B.J. Geletka, J.J. Hsu, C.K. Drummond, D.M. Phelan, J.E. Voos, Wearable Technology and Analytics as a Complementary Toolkit to Optimize Workload and to Reduce Injury Burden, Front. Sport. Act. Living. 2 (2021) 630576. https://doi.org/10.3389/FSPOR.2020.630576/BIBTEX.

[2] T. Hew-Butler, M.H. Rosner, S. Fowkes-Godek, J.P. Dugas, M.D. Hoffman, D.P. Lewis, R.J. Maughan, K.C. Miller, S.J. Montain, N.J. Rehrer, W.O. Roberts, I.R. Rogers, A.J. Siegel, K.J. Stuempfle, J.M. Winger, J.G. Verbalis, Statement of the Third International Exercise-Associated Hyponatremia Consensus Development Conference, Carlsbad, California, 2015, Clin. J. Sport Med. 25 (2015) 303–320. https://doi.org/10.1097/JSM.0000000000000221.

[3] D.S. Yang, R. Ghaffari, J.A. Rogers, Sweat as a diagnostic biofluid, Science (80-.). 379 (2023) 760–761. https://doi.org/10.1126/SCIENCE.ABQ5916.

[4] J.A. Boulant, Hypothalamic mechanisms in thermoregulation, Fed. Proc. 40 (1981) 2843–50.

[5] M. Gleeson, Temperature regulation during exercise, Int. J. Sports Med. 19 (1998) S96–S99. https://doi.org/10.1055/S-2007-971967/BIB.

[6] M.N. Sawka, C.B. Wenger, Physiological Responses to Acute Exercise-Heat Stress, Hum. Perform. Physiol. Environ. Med. Terr. Extrem. (1988)

97–151.
http://oai.dtic.mil/oai/oai?verb=getRecord%7B&%7DmetadataPrefix=html%7B&%7Didentifier=ADA192606.

[7] C.B. Wenger, Heat of evaporation of sweat: thermodynamic considerations., Https://Doi.Org/10.1152/Jappl.1972.32.4.456. 32 (1972) 456–459. https://doi.org/10.1152/JAPPL.1972.32.4.456.

[8] M.N. Sawka, L.R. Leon, S.J. Montain, L.A. Sonna, Integrated Physiological Mechanisms of Exercise Performance, Adaptation, and Maladaptation to Heat Stress, Compr. Physiol. 1 (2011) 1883–1928. https://doi.org/10.1002/CPHY.C100082.

[9] K. Sato, The physiology, pharmacology, and biochemistry of the eccrine sweat gland., Rev. Physiol. Biochem. Pharmacol. 79 (1977) 51–131. https://doi.org/10.1007/BFB0037089.

[10] R.J. Maughan, Fluid and electrolyte loss and replacement in exercise, J. Sports Sci. 9 (1991) 117–142. https://doi.org/10.1080/02640419108729870.

[11] R.M. Berne, M.N. Levy, Physiology, in: 1998.

[12] K. Sato, F. Sato, Na+, K+, H+, Cl-, and Ca2+ concentrations in cystic fibrosis eccrine sweat in vivo and in vitro, J. Lab. Clin. Med. 115 (1990) 504–11.

[13] D.L. Costill, Sweating: Its composition and effects on body fluids, Ann. N. Y. Acad. Sci. 301 (1977) 160–174. https://doi.org/10.1111/J.1749-6632.1977.TB38195.X.

[14] P.M. Quinton, Effects of some ion transport inhibitors on secretion and reabsorption in intact and perfused single human sweat glands, Pflügers Arch. Eur. J. Physiol. 391 (1981) 309–313. https://doi.org/10.1007/BF00581513/METRICS.

[15] M.M. Ready, P.M. Quinton, Rapid regulation of electrolyte absorption in

sweat duct, J. Membr. Biol. 140 (1994) 57–67. https://doi.org/10.1038/438577a.

[16] M.J. Buono, R. Claros, T. DeBoer, J. Wong, Na+ secretion rate increases proportionally more than the Na+ reabsorption rate with increases in sweat rate, J. Appl. Physiol. 105 (2008) 1044–1048. https://doi.org/10.1152/JAPPLPHYSIOL.90503.2008/ASSET/IMAGES/LARGE/ZDG0090881480004.JPEG.

[17] L.B. Baker, J.R. Stofan, A.A. Hamilton, C.A. Horswill, Comparison of regional patch collection vs. whole body washdown for measuring sweat sodium and potassium loss during exercise, J. Appl. Physiol. 107 (2009) 887–895. https://doi.org/10.1152/JAPPLPHYSIOL.00197.2009/ASSET/IMAGES/LARGE/ZDG0080986760003.JPEG.

[18] M.J. Patterson, S.D.R. Galloway, M.A. Nimmo, Variations in regional sweat composition in normal human males, Exp. Physiol. 85 (2000) 869–875. https://doi.org/10.1111/J.1469-445X.2000.02058.X.

[19] D.B. Dill, F.G. Hall, W. Van Beaumont, Sweat chloride concentration: sweat rate, metabolic rate, skin temperature, and age., J. Appl. Physiol. 21 (1966) 99–106. https://doi.org/10.1152/JAPPL.1966.21.1.99.

[20] M. Bariya, H.Y.Y. Nyein, A. Javey, Wearable sweat sensors, Nat. Electron. 1 (2018) 160–171. https://doi.org/10.1038/s41928-018-0043-y.

[21] Z. Sonner, E. Wilder, J. Heikenfeld, G. Kasting, F. Beyette, D. Swaile, F. Sherman, J. Joyce, J. Hagen, N. Kelley-Loughnane, R. Naik, The microfluidics of the eccrine sweat gland, including biomarker partitioning, transport, and biosensing implications, Biomicrofluidics. 9 (2015) 1–19. https://doi.org/10.1063/1.4921039.

[22] H.Y.Y. Nyein, L.C. Tai, Q.P. Ngo, M. Chao, G.B. Zhang, W. Gao, M. Bariya, J. Bullock, H. Kim, H.M. Fahad, A. Javey, A Wearable Microfluidic Sensing

Patch for Dynamic Sweat Secretion Analysis, ACS Sensors. 3 (2018) 944–952. https://doi.org/10.1021/acssensors.7b00961.

[23] B. Zhong, K. Jiang, L. Wang, G. Shen, B. Zhong, L. Wang, G. Shen, K. Jiang, Wearable Sweat Loss Measuring Devices: From the Role of Sweat Loss to Advanced Mechanisms and Designs, Adv. Sci. 9 (2022) 2103257. https://doi.org/10.1002/ADVS.202103257.

[24] D. Vairo, L. Bruzzese, M. Marlinge, L. Fuster, N. Adjriou, N. Kipson, P. Brunet, J. Cautela, Y. Jammes, G. Mottola, S. Burtey, J. Ruf, R. Guieu, E. Fenouillet, Towards Addressing the Body Electrolyte Environment via Sweat Analysis:Pilocarpine Iontophoresis Supports Assessment of Plasma Potassium Concentration, Sci. Reports 2017 71. 7 (2017) 1–7. https://doi.org/10.1038/s41598-017-12211-y.

[25] M.A. Yokus, T. Songkakul, V.A. Pozdin, A. Bozkurt, M.A. Daniele, Wearable multiplexed biosensor system toward continuous monitoring of metabolites, Biosens. Bioelectron. 153 (2020) 112038. https://doi.org/10.1016/J.BIOS.2020.112038.

[26] L.B. Baker, C.T. Ungaro, K.A. Barnes, R.P. Nuccio, A.J. Reimel, J.R. Stofan, Validity and reliability of a field technique for sweat Na+ and K+ analysis during exercise in a hot-humid environment, Physiol. Rep. 2 (2014). https://doi.org/10.14814/phy2.12007.

[27] I. Rollo, R.K. Randell, L. Baker, J.Y. Leyes, D.M. Leal, A. Lizarraga, J. Mesalles, A.E. Jeukendrup, L.J. James, J.M. Carter, Fluid Balance, Sweat Na+ Losses, and Carbohydrate Intake of Elite Male Soccer Players in Response to Low and High Training Intensities in Cool and Hot Environments, Nutrients. 13 (2021) 401. https://doi.org/10.3390/NU13020401.

[28] L.B. Baker, P.J.D. De Chavez, R.P. Nuccio, S.D. Brown, M.A. King, B.C. Sopeña, K.A. Barnes, Explaining variation in sweat sodium concentration: Effect of individual characteristics and exercise,

environmental, and dietary factors, J. Appl. Physiol. 133 (2022) 1250–1259. https://doi.org/10.1152/japplphysiol.00391.2022.

[29] J. Zhang, M. Rupakula, F. Bellando, E. Garcia Cordero, J. Longo, F. Wildhaber, G. Herment, H. Guérin, A.M. Ionescu, Sweat Biomarker Sensor Incorporating Picowatt, Three-Dimensional Extended Metal Gate Ion Sensitive Field Effect Transistors, ACS Sensors. 4 (2019) 2039–2047. https://doi.org/10.1021/acssensors.9b00597.

[30] L.B. Baker, Sweating Rate and Sweat Sodium Concentration in Athletes: A Review of Methodology and Intra/Interindividual Variability, Sport. Med. 47 (2017) 111–128. https://doi.org/10.1007/s40279-017-0691-5.

[31] S. Wang, C. Lafaye, M. Saubade, C. Besson, J. M. Margarit-Taule, V. Gremeaux, S.C. Liu, Predicting hydration status using machine learning models from physiological and sweat biomarkers during endurance exercise: a single case study, IEEE J. Biomed. Heal. Informatics. 26 (2022) 4725. https://doi.org/10.1109/JBHI.2022.3186150.

[32] M.J. Buono, N.V.L. Lee, P.W. Miller, The relationship between exercise intensity and the sweat lactate excretion rate, J. Physiol. Sci. 60 (2010) 103–107. https://doi.org/10.1007/s12576-009-0073-3.

[33] Lens Scholarly Search: (a) Sweat Analysis and (b) Wearable Sweat Analysis., (n.d.). https://www.lens.org/lens/search/scholar/analysis?q=(sweat analysis)&p=0&n=10&s=_score&d=%2B&f=false&e=false&l=en&authorField=author&dateFilterField=publishedYear&orderBy=%2B_score&presentation=false&preview=true&stemmed=true&useAuthorId=false (accessed December 15, 2023).

[34] W.R. Thompson, Worldwide Survey of Fitness Trends for 2016: 10th Anniversary Edition, ACSM's Heal. Fit. J. 19 (2015) 9–16. https://doi.org/10.1249/FIT.0000000000000164.

[35] R. Ghaffari, J.A. Rogers, T.R. Ray, Recent progress, challenges, and opportunities for wearable biochemical sensors for sweat analysis, Sensors Actuators B Chem. B Chem. 332 (2021) 129447. https://doi.org/10.1016/j.snb.2021.129447.

[36] A. Golparvar, S. Tonello, A. Meimandi, S. Carrara, Inkjet-printed Soft Intelligent Medical Bracelet for Simultaneous Real-time Sweat Potassium (K+), Sodium (Na+), and Skin Temperature Analysis, IEEE Sensors Lett. (2023). https://doi.org/10.1109/LSENS.2023.3267180.

[37] G. Matzeu, C. O'Quigley, E. McNamara, C. Zuliani, C. Fay, T. Glennon, D. Diamond, An integrated sensing and wireless communications platform for sensing sodium in sweat, Anal. Methods. 8 (2015) 64–71. https://doi.org/10.1039/C5AY02254A.

[38] G. Xu, C. Cheng, Z. Liu, W. Yuan, X. Wu, Y. Lu, S.S. Low, J. Liu, L. Zhu, D. Ji, S. Li, Z. Chen, L. Wang, Q. Yang, Z. Cui, Q. Liu, Battery-Free and Wireless Epidermal Electrochemical System with All-Printed Stretchable Electrode Array for Multiplexed In Situ Sweat Analysis, Adv. Mater. Technol. 4 (2019) 1–13. https://doi.org/10.1002/admt.201800658.

[39] S. Nakata, T. Arie, S. Akita, K. Takei, Wearable, Flexible, and Multifunctional Healthcare Device with an ISFET Chemical Sensor for Simultaneous Sweat pH and Skin Temperature Monitoring, ACS Sensors. 2 (2017) 443–448. https://doi.org/10.1021/acssensors.7b00047.

[40] P. Bergveld, Thirty years of ISFETOLOGY: What happened in the past 30 years and what may happen in the next 30 years, Sensors Actuators B Chem. 88 (2003) 1–20. https://doi.org/10.1016/S0925-4005(02)00301-5.

[41] G. Eisenman, Glass Electrodes for Hydrogen and Other Cations, 1967.

[42] D.E. Yates, S. Levine, T.W. Healy, Site-binding model of the electrical double layer at the oxide/water interface, J. Chem. Soc. Faraday Trans. 1

Phys. Chem. Condens. Phases. 70 (1974) 1807–1818. https://doi.org/10.1039/F19747001807.

[43] R.S.C. Cobbold, Basic Properties of the Electrolyte-SiO2-Si System: Physical and Theoretical Aspects, IEEE Trans. Electron Devices. 26 (1979) 1805–1815. https://doi.org/10.1109/T-ED.1979.19690.

[44] J.H. Jeon, W.J. Cho, High-performance extended-gate ion-sensitive field-effect transistors with multi-gate structure for transparent, flexible, and wearable biosensors, Sci. Technol. Adv. Mater. 21 (2020) 371–378. https://doi.org/10.1080/14686996.2020.1775477.

[45] E.K. Hong, W.J. Cho, High sensitivity In-Ga-Zn-O nanofiber-based double gate field effect transistors for chemical sensing, Sensors Actuators B Chem. 326 (2021) 128827. https://doi.org/10.1016/J.SNB.2020.128827.

[46] S.C. Park, H.J. Jeong, M. Heo, J.H. Shin, J.H. Ahn, Carbon Nanotube-Based Ion-Sensitive Field-Effect Transistors with an On-Chip Reference Electrode Toward Wearable Sodium Sensing, ACS Appl. Electron. Mater. 3 (2021) 2580–2588. https://doi.org/10.1021/acsaelm.1c00152.

[47] S. Qiu, W. Tang, X. Xi, W. Sun, Y. Huang, R. Liu, Y. Su, L. Jiang, Q. Wei, Y. Yu, X. Guo, All-additive solution processed silversilver chloride reference electrode for handheld ion-sensitive field-effect transistor sensing system, IEEE Sensors Lett. 2 (2018). https://doi.org/10.1109/LSENS.2018.2880761.

[48] X. Li, J. Dunn, D. Salins, G. Zhou, W. Zhou, S.M. Schüssler-Fiorenza Rose, D. Perelman, E. Colbert, R. Runge, S. Rego, R. Sonecha, S. Datta, T. McLaughlin, M.P. Snyder, Digital Health: Tracking Physiomes and Activity Using Wearable Biosensors Reveals Useful Health-Related Information, PLOS Biol. 15 (2017) e2001402. https://doi.org/10.1371/JOURNAL.PBIO.2001402.

[49] S. Nakata, T. Arie, S. Akita, K. Takei, Wearable, Flexible, and Multifunctional Healthcare Device with an ISFET Chemical Sensor for Simultaneous Sweat pH and Skin Temperature Monitoring, ACS Sensors. 2 (2017) 443–448. https://doi.org/10.1021/acssensors.7b00047.

[50] E. Garcia-Cordero, F. Bellando, J. Zhang, F. Wildhaber, J. Longo, H. Guérin, A.M. Ionescu, Three-Dimensional Integrated Ultra-Low-Volume Passive Microfluidics with Ion-Sensitive Field-Effect Transistors for Multiparameter Wearable Sweat Analyzers, ACS Nano. 12 (2018) 12646–12656. https://doi.org/10.1021/acsnano.8b07413.

[51] A. Cazalé, W. Sant, F. Ginot, J.C. Launay, G. Savourey, F. Revol-Cavalier, J.M. Lagarde, D. Heinry, J. Launay, P. Temple-Boyer, Physiological stress monitoring using sodium ion potentiometric microsensors for sweat analysis, Sensors Actuators B Chem. 225 (2016) 1–9. https://doi.org/10.1016/J.SNB.2015.10.114.

[52] A. Cazalé, W. Sant, J. Launay, F. Ginot, P. Temple-Boyer, Study of field effect transistors for the sodium ion detection using fluoropolysiloxane-based sensitive layers, Sensors Actuators B Chem. 177 (2013) 515–521. https://doi.org/10.1016/J.SNB.2012.11.054.

[53] A. Bratov, J. Muñoz, C. Dominguez, J. Bartrolí, Photocurable polymers applied as encapsulating materials for ISFET production, Sensors Actuators B Chem. 25 (1995) 823–825. https://doi.org/10.1016/0925-4005(95)85183-6.

[54] C.J. Harvey, R.F. LeBouf, A.B. Stefaniak, Formulation and stability of a novel artificial human sweat under conditions of storage and use, Toxicol. Vitr. 24 (2010) 1790–1796. https://doi.org/10.1016/j.tiv.2010.06.016.

[55] J. Zhang, S.C.B. Gopinath, Quantification of cortisol for the medical diagnosis of multiple pregnancy-related diseases, 3 Biotech. 10 (2020) 35. https://doi.org/10.1007/s13205-019-2030-z.

[56] A. Ganguly, K.C. Lin, S. Muthukumar, S. Prasad, Autonomous, Real-Time Monitoring Electrochemical Aptasensor for Circadian Tracking of Cortisol Hormone in Sub-microliter Volumes of Passively Eluted Human Sweat, ACS Sensors. 6 (2021) 63–72. https://doi.org/10.1021/ACSSENSORS.0C01754/ASSET/IMAGES/LARGE/SE0C01754_0006.JPEG.

[57] E. Fernandez-Rosas, A. Baldi, E. Ibañez, L. Barrios, S. Novo, J. Esteve, J.A. Plaza, M. Duch, R.G. Omez, O. Castell, C. Nogu, C. Fernandez-Sanchez, Chemical Functionalization of Polysilicon Microparticles for Single-Cell Studies, Langmuir. 27 (2011) 8302–8308. https://doi.org/10.1021/la200857x.

[58] M. Tounsi, M. Ben Braiek, H. Barhoumi, A. Baraket, M. Lee, N. Zine, A. Maaref, A. Errachid, A novel EIS field effect structures coated with TESUD-PPy-PVC-dibromoaza[7]helicene matrix for potassium ions detection, Mater. Sci. Eng. C. 61 (2016) 608–615. https://doi.org/10.1016/j.msec.2015.12.069.

[59] A. Bratov, N. Abramova, S. Alegret, J. Bartroli, C. Dominguez, J. Muñoz, Photocurable Polymer Matrixes for Potassium-Sensitive Ion-Selective Electrode Membranes, Anal. Chem. 67 (1995) 3589–3595. https://doi.org/10.1021/ac00115a032.

[60] A. Bratov, N. Abramova, C. Domínguez, A. Baldi, Ion-selective field effect transistor (ISFET)-based calcium ion sensor with photocured polyurethane membrane suitable for ionised calcium determination in milk, Anal. Chim. Acta. 408 (2000) 57–64. https://doi.org/10.1016/S0003-2670(99)00871-5.

[61] A. Bratov, N. Abramova, C. Domínguez, Investigation of chloride sensitive ISFETs with different membrane compositions suitable for medical applications, Anal. Chim. Acta. 514 (2004) 99–106. https://doi.org/10.1016/J.ACA.2004.01.034.

[62] A. Beltran, J. Artigas, C. Jiménez, R. Mas, J. Bartrolí, J. Alonso, Development of Durable Nitrate-Selective Membranes for All-Solid State ISE and ISFET Sensors Based on Photocurable Compositions, Electroanalysis. 14 (2002) 213–220.

[63] A. Bratov, C. Dominguez, Chemical Multi-Sensor Arrays for Liquids Monolithic Integration Using Microelectronic Technology, in: Def. against Bioterror, Springer-Verlag, Berlin/Heidelberg, 2005: pp. 273–289. https://doi.org/10.1007/1-4020-3384-2_21.

[64] A. Bratov, A. Merlos, L. Moreno, A. Baldi, C. Dominguez, Chemical Multi-Sensor Array with Electrically Isolated Devices, Dig. Tech. Pap. Eurosensors XVIII, Rome, Italy. (2004) 12–15.

[65] C. Jiménez, A. Bratov, N. Abramova, A. Baldi, ISFET based sensors: fundamentals and applications, Encycl. Sensors. (2005).

[66] C. Jimenez-Jorquera, J. Orozco, A. Baldi, ISFET Based Microsensors for Environmental Monitoring, Sensors. 10 (2010) 61–83. https://doi.org/10.3390/s100100061.

[67] J. Muñoz, A. Bratov, R. Mas, N. Abramova, C. Domínguez, J. Bartrolí, Planar Compatible Polymer Technology for Packaging of Chemical Microsensors, J. Electrochem. Soc. 143 (1996) 2020–2025. https://doi.org/10.1149/1.1836942.

[68] J. Muñoz, C. Jimenez, A. Bratov, J. Bartrolí, S. Alegret, C. Dominguez, Photosensitive polyurethanes applied to the development of CHEMFET and ENFET devices for biomedical sensing, Biosens. Bioelectron. 12 (1997) 577–585. https://doi.org/10.1016/S0956-5663(96)00081-4.

[69] D.M. Knotter, The Chemistry of Wet Etching, Handb. Clean. Semicond. Manuf. Fundam. Appl. (2011) 95–141. https://doi.org/10.1002/9781118071748.CH3.

[70] A. Bratov, N. Abramova, J. Muñoz, C. Domínguez, S. Alegret, J. Bartrolí,

Ion Sensor with Photocurable Polyurethane Polymer Membrane, J. Electrochem. Soc. 141 (1994) L111–L112. https://doi.org/10.1149/1.2055170.

[71] J. Artigas, A. Beltran, C. Jiménez, A. Baldi, R. Mas, C. Domínguez, J. Alonso, Application of ion sensitive field effect transistor based sensors to soil analysis, Comput. Electron. Agric. 31 (2001) 281–293. https://doi.org/10.1016/S0168-1699(00)00187-3.

[72] N. Abramova, Y. Borisov, A. Bratov, P. Gavrilenko, C. Domínguez, V. Spiridonov, E. Suglobova, Application of an ion-selective field effect transistor with a photocured polymer membrane in nephrology for determination of potassium ions in dialysis solutions and in blood plasma, Talanta. 52 (2000) 533–538. https://doi.org/10.1016/S0039-9140(00)00408-2.

[73] L. Moreno I Codinachs, A. Baldi, A. Merlos, N. Abramova, A. Ipatov, C. Jiménez-Jorquera, A. Bratov, Integrated multisensor for FIA-based electronic tongue applications, IEEE Sens. J. 8 (2008) 608–615. https://doi.org/10.1109/JSEN.2008.918965.

[74] M. Gutiérrez-Capitán, M. Brull-Fontserè, C. Jiménez-Jorquera, Organoleptic Analysis of Drinking Water Using an Electronic Tongue Based on Electrochemical Microsensors, Sensors. 19 (2019) 1435. https://doi.org/10.3390/S19061435.

[75] N. Abramova, A. Ipatov, S. Levichev, A. Bratov, Integrated multi-sensor chip with photocured polymer membranes containing copolymerised plasticizer for direct pH, potassium, sodium and chloride ions determination in blood serum, Talanta. 79 (2009) 984–989. https://doi.org/10.1016/J.TALANTA.2009.03.023.

[76] J. Orozco, G. Suárez, C. Fernández-Sánchez, C. McNeil, C. Jiménez-Jorquera, Characterization of ultramicroelectrode arrays combining electrochemical techniques and optical microscopy imaging,

Electrochim. Acta. 53 (2007) 729–736. https://doi.org/10.1016/J.ELECTACTA.2007.07.049.

[77] P. Gimenez-Gomez, R. Escude-Pujol, C. Jimenez-Jorquera, M. Gutierrez-Capitan, Multisensor Portable Meter for Environmental Applications, IEEE Sens. J. 15 (2015) 6517–6523. https://doi.org/10.1109/JSEN.2015.2460011.

[78] C. Lafaye, M. Rovira, S. Demuru, S. Wang, J. Kim, B.P. Kunnel, C. Besson, C. Fernandez-Sanchez, F. Serra-Graells, J.M. Margarit-Taule, J. Aymerich, J. Cuenca, I. Kiselev, V. Gremeaux, M. Saubade, C. Jimenez-Jorquera, D. Briand, S.C. Liu, Real-time smart multisensing wearable platform for monitoring sweat biomarkers during exercise, BioCAS 2022 - IEEE Biomed. Circuits Syst. Conf. Intell. Biomed. Syst. a Better Futur. Proc. (2022) 173–177. https://doi.org/10.1109/BIOCAS54905.2022.9948565.

[79] N. Abramova, A. Bratov, Photocurable Polymers for Ion Selective Field Effect Transistors. 20 Years of Applications, Sensors 2009, Vol. 9, Pages 7097-7110. 9 (2009) 7097–7110. https://doi.org/10.3390/S90907097.

[80] A. Bratov, N. Abrmova, J. Muiloz', Cdominguez', S. Alegret, J. Bartroli, Y. Vlasov, Acrylated Polyurethane As An Alternative Ion-selective Membrane Matrix For Chemical Sensors, (1995). https://doi.org/10.1109/SENSOR.1995.717372.

[81] Li-Te Yin, Jung-Chuan Chou, Wen-Yaw Chung, Tai-Ping Sun, Shen-Ken Hsiung, Characteristics of silicon nitride after O2 plasma surface treatment for pH-ISFET applications, IEEE Trans. Biomed. Eng. 48 (2001) 340–344. https://doi.org/10.1109/10.914797.

[82] M. Dawgul, D.G. Pijanowska, A. Krzyskow, J. Kruk, W. Torbicz, An influence of polyHEMA gate layer on properties of ChemFETs, Sensors 2003, Vol. 3, Pages 146-159. 3 (2003) 146–159. https://doi.org/10.3390/S30600146.

[83] A.C. Miller, J.C. Berg, Effect of silane coupling agent adsorbate structure on adhesion performance with a polymeric matrix, Compos. Part A Appl. Sci. Manuf. 34 (2003) 327–332. https://doi.org/10.1016/S1359-835X(03)00051-4.

[84] E.P. Plueddemann, Nature of Adhesion Through Silane Coupling Agents, Silane Coupling Agents. (1991) 115–152. https://doi.org/10.1007/978-1-4899-2070-6_5.

[85] N.S. Allen, Photoinitiators for UV and visible curing of coatings: Mechanisms and properties, J. Photochem. Photobiol. A Chem. 100 (1996) 101–107. https://doi.org/10.1016/S1010-6030(96)04426-7.

[86] S. Alegret, J. Bartrolí, C. Jiménez, M. del Valle, C. Domínguez, E. Cabruja, A. Merlos, pH-ISFET with NMOS technology, Electroanalysis. 3 (1991) 355–360. https://doi.org/10.1002/elan.1140030418.

[87] A.M. Ali, N. Yahya, A. Mijinyawa, M.Y. Kwaya, S. Sikiru, Molecular simulation and microtextural characterization of quartz dissolution in sodium hydroxide, J. Pet. Explor. Prod. Technol. 10 (2020) 2669–2684. https://doi.org/10.1007/s13202-020-00940-2.

[88] M. Gutierrez, A. Llobera, J. Vila-Planas, F. Capdevila, S. Demming, S. Büttgenbach, S. Mínguez, C. Jimenez-Jorquera, Hybrid electronic tongue based on optical and electrochemical microsensors for quality control of wine, Analyst. 135 (2010) 1718–1725. https://doi.org/10.1039/c0an00004c.

[89] S.S. Sandhu, A.Y. Chang, P.U.A.I. Fernando, J.F. Morales, N. Tostado, J. Jernberg, L.C. Moores, J. Wang, MIP-202 catalyst-integrated solid-contact potentiometric chloride sensor for versatile multiphasic detection of a sulfur mustard simulant, Sensors Actuators B Chem. 375 (2023) 132818. https://doi.org/10.1016/J.SNB.2022.132818.

[90] P. Giménez-Gómez, R. Escudé-Pujol, F. Capdevila, A. Puig-Pujol, C.

Jiménez-Jorquera, M. Gutiérrez-Capitán, Portable Electronic Tongue Based on Microsensors for the Analysis of Cava Wines, Sensors. 16 (2016). https://doi.org/10.3390/s16111796.

[91] A.R.L. Fraga, J.C. Quintana, G.L. Destri, N. Giamblanco, R.G. Toro, F. Punzo, Polymeric membranes conditioning for sensors applications: Mechanism and influence on analytes detection, J. Solid State Electrochem. 16 (2012) 901–909. https://doi.org/https://doi.org/10.1007/s10008-011-1456-y.

[92] M. Guzinski, J.M. Jarvis, B.D. Pendley, E. Lindner, Equilibration Time of Solid Contact Ion-Selective Electrodes, Anal. Chem. 87 (2015) 6654–6659. https://doi.org//10.1021/acs.analchem.5b00775.

[93] J.M. Margarit-Taulé, M. Martín-Ezquerra, R. Escudé-Pujol, C. Jiménez-Jorquera, S.-C. Liu, Cross-compensation of FET sensor drift and matrix effects in the industrial continuous monitoring of ion concentrations, Sensors Actuators B Chem. 353 (2022) 131123. https://doi.org/10.1016/J.SNB.2021.131123.

[94] S. Wang, M. Rovira, Y. Hu, C. Jiménez-Jorquera, S.-C. Liu, End-to-End Prediction of Sodium Concentration from Uncalibrated Sodium ISFETs, 2023 IEEE Int. Symp. Circuits Syst. (2023) 1–5. https://doi.org/10.1109/ISCAS46773.2023.10181566.

[95] H. Liu, Z. Gu, Y. Liu, X. Xiao, G. Xiu, Validation of the Application of Solid Contact Ion-Selective Electrode for Off-Body Sweat Ion Monitoring, Biosensors. 12 (2022) 229. https://doi.org/10.3390/BIOS12040229/S1.

[96] L.B. Baker, K.A. Barnes, M.L. Anderson, D.H. Passe, J.R. Stofan, Normative data for regional sweat sodium concentration and whole-body sweating rate in athletes, J. Sports Sci. 34 (2016) 358–368. https://doi.org/10.1080/02640414.2015.1055291.

[97] J.M. Bland, D.G. Altman, Statistical methods for assessing agreement between two methods of clinical measurement, Lancet. 327 (1986) 307–310. https://doi.org/10.1016/j.ijnurstu.2010.03.004.

[98] H.-M. Sheu, S.-C. Chao, T.-W. Wong, J. Yu-Yun, J.-C. Tsai, Human skin surface lipid film: an ultrastructural study and interaction with corneocytes and intercellular lipid lamellae of the stratum corneum, Br. J. Dermatol. 140 (1999) 385–391. https://doi.org/10.1046/j.1365-2133.1999.02697.x.

[99] G. Dimeski, P. Mollee, A. Carter, Effects of Hyperlipidemia on Plasma Sodium, Potassium, and Chloride Measurements by an Indirect Ion-Selective Electrode Measuring System, Clin. Chem. 52 (2006) 155–156. https://doi.org/10.1373/CLINCHEM.2005.054981.

[100] S.K. Datta, P. Chopra, Interference in Ion-Selective Electrodes Due to Proteins and Lipids, J. Appl. Lab. Med. 7 (2022) 589–595. https://doi.org/10.1093/JALM/JFAB125.

[101] A. Kisiel, H. Marcisz, A. Michalska, K. Maksymiuk, All-solid-state reference electrodes based on conducting polymers, Analyst. 130 (2005) 1655–1662. https://doi.org/10.1039/B510868C.

[102] R. Mamińska, A. Dybko, W. Wróblewski, All-solid-state miniaturised planar reference electrodes based on ionic liquids, Sensors Actuators B Chem. 115 (2006) 552–557. https://doi.org/10.1016/J.SNB.2005.10.018.

[103] T. Matsuo, M. Esashi, No Title, in: Proc. 153rd Meet. Electrochem. Soc. - Ext. Abstr., 1978: pp. 202–203.

[104] H. Nakajima, M. Esashi, T. Matsuo, The cation concentration response of polymer gate ISFET, J. Electrochem. Soc. 129 (1982) 141–143.

[105] D.N. Reinhoudt, Application of supramolecular chemistry in the development of ion-selective CHEMFETs, Sensors Actuators B Chem. 6

(1992) 179–185. https://doi.org/10.1016/0925-4005(92)80052-Y.

[106] D.P. Brezinski, Kinetic, static and stirring errors of liquid junction reference electrodes, Analyst. 108 (1983) 425–442. https://doi.org/10.1039/AN9830800425.

[107] M. Waleed Shinwari, D. Zhitomirsky, I.A. Deen, P.R. Selvaganapathy, M. Jamal Deen, D. Landheer, Microfabricated Reference Electrodes and their Biosensing Applications, Sensors 2010, Vol. 10, Pages 1679-1715. 10 (2010) 1679–1715. https://doi.org/10.3390/S100301679.

[108] F. Criscuolo, M. Galfione, S. Carrara, G. De Micheli, All-solid-state Reference Electrodes for analytical applications, (n.d.).

[109] Q. Li, W. Tang, Y. Su, Y. Huang, S. Peng, B. Zhuo, S. Qiu, L. Ding, Y. Li, X. Guo, Stable thin-film reference electrode on plastic substrate for all-solid-state ion-sensitive field-effect transistor sensing system, IEEE Electron Device Lett. 38 (2017) 1469–1472. https://doi.org/10.1109/LED.2017.2732352.

[110] S. Sopstad, K. Imenes, E.A. Johannessen, Chloride and pH Determination on a Wireless, Flexible Electrochemical Sensor Platform, IEEE Sens. J. 20 (2020) 599–609. https://doi.org/10.1109/JSEN.2019.2944407.

[111] M. Bariya, L. Li, R. Ghattamaneni, C.H. Ahn, H.Y.Y. Nyein, L.C. Tai, A. Javey, Glove-based sensors for multimodal monitoring of natural sweat, Sci. Adv. 6 (2020) 8308–8336. https://doi.org/10.1126/sciadv.abb8308.

[112] M. Rovira, C. Fernández-Sánchez, C. Jiménez-Jorquera, Hybrid Technologies Combining Solid-State Sensors and Paper/Fabric Fluidics for Wearable Analytical Devices, Biosensors. 11 (2021) 303. https://doi.org/10.3390/BIOS11090303.

[113] E.J.R. Sudhölter, P.D. van der Wal, M. Skowronska-Ptasinska, A. van den Berg, P. Bergveld, D.N. Reinhoudt, Modification of ISFETs by covalent anchoring of poly(hyroxyethyl methacrylate) hydrogel. Introduction of

a thermodynamically defined semiconductor-sensing membrane interface, Anal. Chim. Acta. 230 (1990) 59–65. https://doi.org/10.1016/S0003-2670(00)82761-0.

[114] A. van den Berg, A. Grisel, E. Verney-Norberg, An ISFET-based calcium sensor using a photopolymerized polysiloxane membrane, Sensors Actuators B Chem. 4 (1991) 235–238. https://doi.org/10.1016/0925-4005(91)80115-Z.

[115] H. Ayhan, F. Ayhan, Water based PHEMA hydrogels for controlled drug delivery, Turkish J. Biochem. 43 (2018) 228–239. https://doi.org/10.1515/TJB-2017-0250/MACHINEREADABLECITATION/RIS.

[116] S.K. Siddhanta, R. Gangopadhyay, Conducting polymer gel: formation of a novel semi-IPN from polyaniline and crosslinked poly(2-acrylamido-2-methyl propanesulphonicacid), Polymer (Guildf). 46 (2005) 2993–3000. https://doi.org/10.1016/J.POLYMER.2005.01.084.

[117] T. Shiga, H. Mori, K. Uemura, R. Moriuchi, H. Dohra, A. Yamawaki-Ogata, Y. Narita, A. Saito, Y. Kotsuchibashi, Evaluation of the Bactericidal and Fungicidal Activities of Poly([2-(methacryloyloxy)ethyl]trimethyl Ammonium Chloride)(Poly (METAC))-Based Materials, Polym. 2018, Vol. 10, Page 947. 10 (2018) 947. https://doi.org/10.3390/POLYM10090947.

[118] M. Gutiérrez-Capitán, A. Baldi, R. Gómez, V. García, C. Jiménez-Jorquera, C. Fernández-Sánchez, Electrochemical nanocomposite-derived sensor for the analysis of chemical oxygen demand in urban wastewaters, Anal. Chem. 87 (2015) 2152–2160. https://doi.org/10.1021/ac503329a.

[119] S.T. Hemp, A.E. Smith, W.C. Bunyard, M.H. Rubinstein, T.E. Long, RAFT polymerization of temperature- and salt-responsive block copolymers as reversible hydrogels, Polymer (Guildf). 55 (2014) 2325–2331. https://doi.org/10.1016/J.POLYMER.2014.03.062.

[120] T. Ye, Y. Song, Q. Zheng, Salt response and rheological behavior of acrylamide-sulfobetaine copolymer, Colloid Polym. Sci. 294 (2016) 389–397. https://doi.org/10.1007/s00396-015-3790-6.

[121] W. Yuan, J. Wang, Oligo(ethylene glycol) and quaternary ammonium-based block copolymer micelles: from tunable thermoresponse to dual salt response, RSC Adv. 4 (2014) 38855–38858. https://doi.org/10.1039/C4RA05096G.

[122] D.E. Watson, D.M. Yee, Behaviour of Ag/AgCl electrodes in solutions containing both Cl− and I−, Electrochim. Acta. 14 (1969) 1143–1153. https://doi.org/10.1016/0013-4686(69)80040-X.

[123] E. Cho, M. Mohammadifar, S. Choi, A single-use, self-powered, paper-based sensor patch for detection of exercise-induced hypoglycemia, Micromachines. 8 (2017). https://doi.org/10.3390/mi8090265.

[124] E. Elizalde, R. Urteaga, C.L.A. Berli, Rational design of capillary-driven flows for paper-based microfluidics, Lab Chip. 15 (2015) 2173–2180. https://doi.org/10.1039/c4lc01487a.

[125] S. Kim, B. Lee, J.T. Reeder, S.H. Seo, S.U. Lee, A. Hourlier-Fargette, J. Shin, Y. Sekine, H. Jeong, Y.S. Oh, A.J. Aranyosi, S.P. Lee, J.B. Model, G. Lee, M.H. Seo, S.S. Kwak, S. Jo, G. Park, S. Han, I. Park, H. Il Jung, R. Ghaffari, J. Koo, P. V. Braun, J.A. Rogers, Soft, skin-interfaced microfluidic systems with integrated immunoassays, fluorometric sensors, and impedance measurement capabilities, Proc. Natl. Acad. Sci. U. S. A. 117 (2020) 27906–27915. https://doi.org/10.1073/pnas.2012700117.

[126] Q. An, S. Gan, J. Xu, Y. Bao, T. Wu, H. Kong, L. Zhong, Y. Ma, Z. Song, L. Niu, A multichannel electrochemical all-solid-state wearable potentiometric sensor for real-time sweat ion monitoring, Electrochem. Commun. 107 (2019) 106553. https://doi.org/10.1016/J.ELECOM.2019.106553.

[127] M. Li, L. Wang, R. Liu, J. Li, Q. Zhang, G. Shi, Y. Li, C. Hou, H. Wang, A

highly integrated sensing paper for wearable electrochemical sweat analysis, Biosens. Bioelectron. 174 (2021) 112828. https://doi.org/10.1016/j.bios.2020.112828.

[128] E.A. Algadiem, A.A. Aleisa, H.I. Alsubaie, N.R. Buhlaiqah, J.B. Algadeeb, H.A. Alsneini, Blood Loss Estimation Using Gauze Visual Analogue, Trauma Mon. 21 (2016) 34131. https://doi.org/10.5812/TRAUMAMON.34131.

[129] R.M. Morgan, M.J. Patterson, M.A. Nimmo, Acute effects of dehydration on sweat composition in men during prolonged exercise in the heat, Acta Physiol. Scand. 182 (2004) 37–43. https://doi.org/10.1111/j.1365-201X.2004.01305.x.

[130] M. Ring, C. Lohmueller, M. Rauh, B.M. Eskofier, On sweat analysis for quantitative estimation of dehydration during physical exercise, Proc. Annu. Int. Conf. IEEE Eng. Med. Biol. Soc. EMBS. 2015-November (2015) 7011–7014. https://doi.org/10.1109/EMBC.2015.7320006.

[131] L.B. Baker, P.J.D. De Chavez, C.T. Ungaro, B.C. Sopeña, R.P. Nuccio, A.J. Reimel, K.A. Barnes, Exercise intensity effects on total sweat electrolyte losses and regional vs. whole-body sweat [Na+], [Cl−], and [K+], Eur. J. Appl. Physiol. 119 (2019) 361–375. https://doi.org/10.1007/S00421-018-4048-Z.

[132] R. Chin, B.Y. Lee, Analysis of Data, Princ. Pract. Clin. Trial Med. (2008) 325–359. https://doi.org/10.1016/B978-0-12-373695-6.00015-6.

[133] H. Abdi, W. Lynne J., Tukey's honestly significant difference (HSD) test, Encycl. Res. Des. 3.1. (2010) 1–5.

[134] V. Rodríguez-Rielves, J.R. Lillo-Beviá, Á. Buendía-Romero, A. Martínez-Cava, A. Hernández-Belmonte, J. Courel-Ibáñez, J.G. Pallarés, Are the assioma favero power meter pedals a reliable tool for monitoring cycling power output?, Sensors. 21 (2021) 1–9.

https://doi.org/10.3390/s21082789.

[135] L.B. Weschler, Sweat electrolyte concentrations obtained from within occlusive coverings are falsely high because sweat itself leaches skin electrolytes, J. Appl. Physiol. 105 (2008) 1376–1377. https://doi.org/10.1152/JAPPLPHYSIOL.00924.2007.

[136] L.B. Baker, A.S. Wolfe, Physiological mechanisms determining eccrine sweat composition, Eur. J. Appl. Physiol. 2020 1204. 120 (2020) 719–752. https://doi.org/10.1007/S00421-020-04323-7.

[137] I.L. Schwartz, J.H. Thaysen, Excretion of sodium and potassium in human sweat., J. Clin. Invest. 35 (1956) 114–120. https://doi.org/10.1172/JCI103245.

[138] K. Sato, W.H. Kang, K. Saga, K.T. Sato, Biology of sweat glands and their disorders. I. Normal sweat gland function, J. Am. Acad. Dermatol. 20 (1989) 537–563. https://doi.org/10.1016/S0190-9622(89)70063-3.

[139] D.R. Seshadri, R.T. Li, J.E. Voos, J.R. Rowbottom, C.M. Alfes, C.A. Zorman, C.K. Drummond, Wearable sensors for monitoring the physiological and biochemical profile of the athlete, Npj Digit. Med. 2019 21. 2 (2019) 1–16. https://doi.org/10.1038/s41746-019-0150-9.

[140] J. Jeon, S. Uthaman, J. Lee, H. Hwang, G. Kim, P.J. Yoo, B.D. Hammock, C.S. Kim, Y.S. Park, I.K. Park, In-direct localized surface plasmon resonance (LSPR)-based nanosensors for highly sensitive and rapid detection of cortisol, Sensors Actuators B Chem. 266 (2018) 710–716. https://doi.org/10.1016/J.SNB.2018.03.167.

[141] B.J. Sanghavi, J.A. Moore, J.L. Chávez, J.A. Hagen, N. Kelley-Loughnane, C.F. Chou, N.S. Swami, Aptamer-functionalized nanoparticles for surface immobilization-free electrochemical detection of cortisol in a microfluidic device, Biosens. Bioelectron. 78 (2016) 244–252. https://doi.org/10.1016/J.BIOS.2015.11.044.

[142] M. Jia, W.M. Chew, Y. Feinstein, P. Skeath, E.M. Sternberg, Quantification of cortisol in human eccrine sweat by liquid chromatography-tandem mass spectrometry, Analyst. 141 (2016) 2053–2060. https://doi.org/10.1039/c5an02387d.

[143] D.H. Hellhammer, S. Wüst, B.M. Kudielka, Salivary cortisol as a biomarker in stress research, Psychoneuroendocrinology. 34 (2009) 163–171. https://doi.org/10.1016/J.PSYNEUEN.2008.10.026.

[144] C. Li, Z. Zhang, X. Liu, K. Shen, P. Gu, X. Kang, Simultaneous quantification of cortisol and cortisone in urines from infants with packed-fiber solid-phase extraction coupled to HPLC–MS/MS, J. Chromatogr. B. 1061–1062 (2017) 163–168. https://doi.org/10.1016/J.JCHROMB.2017.07.012.

[145] S. Dalirirad, A.J. Steckl, Aptamer-based lateral flow assay for point of care cortisol detection in sweat, Sensors Actuators, B Chem. 283 (2019) 79–86. https://doi.org/10.1016/J.SNB.2018.11.161.

[146] N. Kobayashi, P. Sun, Y. Fujimaki, T. Niwa, T. Nishio, J. Goto, H. Hosoda, Generation of a novel monoclonal antibody against cortisol-[C-4]-bovine serum albumin conjugate: Application to enzyme-linked immunosorbent assay for urinary and serum cortisol, Anal. Sci. 18 (2002) 1309–1314. https://doi.org/10.2116/ANALSCI.18.1309/METRICS.

[147] H.J. Fu, L.P. Yuan, Y.D. Shen, Y.X. Liu, B. Liu, S.W. Zhang, Z.X. Xie, H.T. Lei, Y.M. Sun, Z.L. Xu, A full-automated magnetic particle-based chemiluminescence immunoassay for rapid detection of cortisol in milk, Anal. Chim. Acta. 1035 (2018) 129–135. https://doi.org/10.1016/J.ACA.2018.06.015.

[148] J. Jeon, S. Uthaman, J. Lee, H. Hwang, G. Kim, P.J. Yoo, B.D. Hammock, C.S. Kim, Y.S. Park, I.K. Park, In-direct localized surface plasmon resonance (LSPR)-based nanosensors for highly sensitive and rapid detection of cortisol, Sensors Actuators B Chem. 266 (2018) 710–716.

https://doi.org/10.1016/J.SNB.2018.03.167.

[149] T. Ito, N. Aoki, W. Shinobu, K. Suzuki, Duplicate Analysis of Cortisol for Stress Check Using QCM with a Self–suction Flow System, Procedia Eng. 87 (2014) 296–299. https://doi.org/10.1016/J.PROENG.2014.11.666.

[150] S. Kämäräinen, M. Mäki, T. Tolonen, G. Palleschi, V. Virtanen, L. Micheli, A.M. Sesay, Disposable electrochemical immunosensor for cortisol determination in human saliva, Talanta. 188 (2018) 50–57. https://doi.org/10.1016/J.TALANTA.2018.05.039.

[151] B.J. Sanghavi, J.A. Moore, J.L. Chávez, J.A. Hagen, N. Kelley-Loughnane, C.F. Chou, N.S. Swami, Aptamer-functionalized nanoparticles for surface immobilization-free electrochemical detection of cortisol in a microfluidic device, Biosens. Bioelectron. 78 (2016) 244–252. https://doi.org/10.1016/J.BIOS.2015.11.044.

[152] W. Huang, K. Besar, R. Lecover, P. Dulloor, J. Sinha, J.F. Martínez Hardigree, C. Pick, J. Swavola, A.D. Everett, J. Frechette, M. Bevan, H.E. Katz, Label-free brain injury biomarker detection based on highly sensitive large area organic thin film transistor with hybrid coupling layer, Chem. Sci. 5 (2013) 416–426. https://doi.org/10.1039/C3SC52638K.

[153] N. Dhull, G. Kaur, V. Gupta, M. Tomar, Highly sensitive and non-invasive electrochemical immunosensor for salivary cortisol detection, Sensors Actuators B Chem. 293 (2019) 281–288. https://doi.org/10.1016/J.SNB.2019.05.020.

[154] Y. Yao, C. Jiang, J. Ping, Flexible freestanding graphene paper-based potentiometric enzymatic aptasensor for ultrasensitive wireless detection of kanamycin, Biosens. Bioelectron. 123 (2019) 178–184. https://doi.org/10.1016/J.BIOS.2018.08.048.

[155] E. Makhneva, Z. Farka, P. Skládal, L. Zajíčková, Cyclopropylamine plasma

polymer surfaces for label-free SPR and QCM immunosensing of Salmonella, Sensors Actuators B Chem. 276 (2018) 447–455. https://doi.org/10.1016/J.SNB.2018.08.055.

[156] R.E. Fernandez, Y. Umasankar, P. Manickam, J.C. Nickel, L.R. Iwasaki, B.K. Kawamoto, K.C. Todoki, J.A.M. Scott, S. Bhansali, Disposable aptamer-sensor aided by magnetic nanoparticle enrichment for detection of salivary cortisol variations in obstructive sleep apnea patients, Sci. Reports 2017 71. 7 (2017) 1–9. https://doi.org/10.1038/s41598-017-17835-8.

[157] S. Gao, W. Hu, X. Zheng, S. Cai, J. Wu, Functionalized aptamer with an antiparallel G-quadruplex: Structural remodeling, recognition mechanism, and diagnostic applications targeting CTGF, Biosens. Bioelectron. 142 (2019) 111475. https://doi.org/10.1016/J.BIOS.2019.111475.

[158] X. Weng, S. Neethirajan, Aptamer-based fluorometric determination of norovirus using a paper-based microfluidic device, Microchim. Acta. 184 (2017) 4545–4552. https://doi.org/10.1007/S00604-017-2467-X/TABLES/1.

[159] K. Abnous, N.M. Danesh, M. Ramezani, M. Alibolandi, S.M. Taghdisi, A novel electrochemical sensor for bisphenol A detection based on nontarget-induced extension of aptamer length and formation of a physical barrier, Biosens. Bioelectron. 119 (2018) 204–208. https://doi.org/10.1016/J.BIOS.2018.08.024.

[160] S. Feng, C. Chen, W. Wang, L. Que, An aptamer nanopore-enabled microsensor for detection of theophylline, Biosens. Bioelectron. 105 (2018) 36–41. https://doi.org/10.1016/J.BIOS.2018.01.016.

[161] N. Nakatsuka, Aptamer–Field-Effect Transistors for Small-Molecule Sensing in Complex Environments, Methods Mol. Biol. 2570 (2023) 187–196. https://doi.org/10.1007/978-1-0716-2695-5_14.

[162] T. Rodrigues, V. Mishyn, Y.R. Leroux, L. Butruille, E. Woitrain, A. Barras, P. Aspermair, H. Happy, C. Kleber, R. Boukherroub, D. Montaigne, W. Knoll, S. Szunerits, Highly performing graphene-based field effect transistor for the differentiation between mild-moderate-severe myocardial injury, Nano Today. 43 (2022) 101391. https://doi.org/10.1016/J.NANTOD.2022.101391.

[163] T. Sakata, Technical Perspectives on Applications of Biologically Coupled Gate Field-Effect Transistors, Sensors. 22 (2022) 4991. https://doi.org/10.3390/S22134991.

[164] E. Stern, R. Wagner, F.J. Sigworth, R. Breaker, T.M. Fahmy, M.A. Reed, Importance of the debye screening length on nanowire field effect transistor sensors, Nano Lett. 7 (2007) 3405–3409. https://doi.org/10.1021/NL071792Z/SUPPL_FILE/NL071792ZSI20070910_015801.PDF.

[165] A. Poghossian, A. Cherstvy, S. Ingebrandt, A. Offenhäusser, M.J. Schöning, Possibilities and limitations of label-free detection of DNA hybridization with field-effect-based devices, Sensors Actuators, B Chem. 111–112 (2005) 470–480. https://doi.org/10.1016/j.snb.2005.03.083.

[166] D. Caballero, E. Martinez, J. Bausells, A. Errachid, J. Samitier, Impedimetric immunosensor for human serum albumin detection on a direct aldehyde-functionalized silicon nitride surface, Anal. Chim. Acta. 720 (2012) 43–48. https://doi.org/10.1016/J.ACA.2012.01.031.

[167] A. Kim, C.S. Ah, C.W. Park, J.H. Yang, T. Kim, C.G. Ahn, S.H. Park, G.Y. Sung, Direct label-free electrical immunodetection in human serum using a flow-through-apparatus approach with integrated field-effect transistors, Biosens. Bioelectron. 25 (2010) 1767–1773. https://doi.org/10.1016/J.BIOS.2009.12.026.

[168] N. Formisano, P. Jolly, N. Bhalla, M. Cromhout, S.P. Flanagan, R. Fogel, J.L. Limson, P. Estrela, Optimisation of an electrochemical impedance

spectroscopy aptasensor by exploiting quartz crystal microbalance with dissipation signals, Sensors Actuators B. 220 (2015) 369–375. https://doi.org/10.1016/j.snb.2015.05.049.

[169] C.S. Lee, S. Kyu Kim, M. Kim, Ion-Sensitive Field-Effect Transistor for Biological Sensing, Sensors 2009, Vol. 9, Pages 7111-7131. 9 (2009) 7111–7131. https://doi.org/10.3390/S90907111.

[170] N. Nakatsuka, J.M. Abendroth, K.A. Yang, A.M. Andrews, Divalent Cation Dependence Enhances Dopamine Aptamer Biosensing, ACS Appl. Mater. Interfaces. 13 (2021) 9425–9435. https://doi.org/10.1021/ACSAMI.0C17535.

[171] S. Sheibani, L. Capua, S. Kamaei, S.S.A. Akbari, J. Zhang, H. Guerin, A.M. Ionescu, Extended gate field-effect-transistor for sensing cortisol stress hormone, Commun. Mater. 2021 21. 2 (2021) 1–10. https://doi.org/10.1038/s43246-020-00114-x.

THESIS CONTRIBUTIONS

Publication 1: Rovira M.; Fernández-Sánchez C.; Demuru S.; Brince P.K.; Briand D.; Jimenez-Jorquera C. Multisensing Wearable Technology for Sweat Biomonitoring (Conference Paper). *Engineering Proceedings* **2021**, 6, 78. **https://doi.org/10.3390/I3S2021Dresden-10113**

Publication 2: Rovira, M.; Fernández-Sánchez, C.; Jiménez-Jorquera, C. Hybrid Technologies Combining Solid-State Sensors and Paper/Fabric Fluidics for Wearable Analytical Devices. *Biosensors* **2021**, 11, 9, 303. **https://doi.org/10.3390/bios11090303**

Publication 3: LeBow N.; Rueckauer B.; Sun P.; Rovira M.; Jiménez-Jorquera C.; Liu S.-C.; Margarit-Taulé J.M. Real-Time Edge Neuromorphic Tasting From Chemical Microsensor Arrays. *Frontiers in Neuroscience* **2021**, 15:771480. https://doi.org/10.3389/fnins.2021.771480

Publication 4: Lafaye C.; Rovira M.; Demuru S.; Wang S.; et al.; Real-time smart multisensing wearable platform for monitoring sweat biomarkers during exercise (Conference Paper). 2022 IEEE Biomedical Circuits and Systems Conference (BioCAS), Taipei, Taiwan, 2022, 173-177. https://doi.org/10.1109/BioCAS54905.2022.9948565

Publication 5: Rovira, M.; Lafaye, C.; Wang, S.; Fernández-Sánchez, C.; Saubade, M.; Liu S.-C.; Jiménez-Jorquera, C. Analytical assessment of sodium ISFET based sensors for sweat analysis. *Sensors and Actuators B: Chemical* **2023**, 393, 134135. https://doi.org/10.1016/j.snb.2023.134135

Publication 6: Wang, S.; Rovira, M.; Demuru, S.; Lafaye, C.; Kim J.; Kunnel, B. P.; Besson, C.; Fernández-Sánchez, C.; Serra-Graells, F.; Margarit-Taulé, J. M.; Aymerich, J.; Cuenca, J.; Kiselev, I.; Gremeaux, V., Saubade, M.; Jiménez-Jorquera, C.; Briand, D.; Liu S.-C. Multisensing Wearables for Real-Time Monitoring of Sweat Electrolyte Biomarkers During Exercise and Analysis on Their Correlation With Core Body Temperature. *IEEE Transactions on Biomedical Circuits and Systems* **2023**, 17, 4, 808-817. https://doi.org/10.1109/TBCAS.2023.3286528

Publication 7: Wang, S.; Rovira, M.; Hu, Y.; Jiménez-Jorquera, C.; Liu, S.-C., "End-to-End Prediction of Sodium Concentration from Uncalibrated Sodium ISFETs," **2023** *IEEE International Symposium on Circuits and Systems (ISCAS)*, Monterey, CA, USA, 2023, pp. 1-5. https://doi.org/10.1109/ISCAS46773.2023.10181566

CONFERENCES

Oral presentation:

17-18/09/20 – 5th Scientific Meeting of PhD Students at UAB Campus (JPhD2020)

20-26/05/21 – 8th International Symposium on Sensor Science (I3S2021)

26-28/05/21 – X Doctoral workshop of the PhD program in chemistry

30/09/21 – XXV Transfrontier Meeting on Sensors and Biosensors - Also, participation as session moderator

05-08/09/22 – Ibero-American Congress on Sensors (Ibersensor)

15/10/22 – Biomedical Circuits and Systems Conference (BioCAS)

20/04/23 – Young Researchers Day (internal congress in IMB-CNM)

Poster presentation:

04-09/10/20 – 24th International Conference on Miniaturized Systems for Chemistry and Life Sciences (μTAS 2020)

07-08/06/22 – Swiss Sweat Science & Technology Symposium (3STS)

29-30/09/22 – XXVI Transfrontier Meeting on Sensors and Biosensors (TMSB)

ANNEX 1

Table A.1. Na^+ and K^+ concentration values determined with LAQUAtwin ISEs in sweat samples collected to assess the influence of the position of the patch in the body, the day of session, the intensity of the exercise and the hydration status.

			E1		E2		E3	
NH/H	Session	Position	Na^+ conc [mM]	K^+ conc [mM]	Na^+ conc [mM]	K^+ conc [mM]	Na^+ conc [mM]	K^+ conc [mM]
NH	1	P1	52	5.6	52	7.2	48	5.1
NH	1	P2	48	7.2	61	7.9	48	6.4
NH	1	P3	61	8.7	70	9.2	65	8.4
NH	1	P4	36	7.7	44	5.1	44	8.7
NH	1	P5	36	7.2	31	6.4	39	8.2
NH	1	P6	44	4.9	42	8.7	48	4.9
NH	1	P7	43	5.1	40	5.6	48	5.1
NH	1	P8	38	5.1	34	5.9	43	4.6
NH	1	P9	32	4.9	35	5.6	39	4.9
NH	1	P10	34	5.6	38	4.9	36	4.6
NH	1	P11	39	4.6	44	5.6	37	4.6
H	2	P1	52	5.6	48	4.9	44	4.1
H	2	P2	61	6.4	83	7.4	48	3.8
H	2	P3	70	5.9	61	4.6	78	5.9
H	2	P4	61	11.3	34	4.9	37	5.1
H	2	P5	34	6.4	37	6.1	32	4.9
H	2	P6	52	6.6	65	4.3	65	4.6
H	2	P7	70	5.6	61	4.6	70	4.1
H	2	P8	52	6.6	57	4.3	52	4.1
H	2	P9	61	5.6	65	4.9	61	4.1
H	2	P10	39	6.4	48	3.8	44	4.1
H	2	P11	52	4.6	48	4.6	61	4.3

NH	3	P1	52	5.6	57	4.6	52	4.6
NH	3	P2	65	5.4	70	5.9	70	5.1
NH	3	P3	87	8.2	61	5.1	74	6.1
NH	3	P4	37	5.9	44	6.1	65	8.2
NH	3	P5	43	8.2	48	7.4	44	7.2
NH	3	P6	65	4.6	61	4.3	57	3.6
NH	3	P7	52	3.8	61	4.6	61	3.8
NH	3	P8	57	4.6	57	4.3	57	3.8
NH	3	P9	52	4.6	61	4.1	61	3.6
NH	3	P10	48	3.8	52	4.3	44	3.6
NH	3	P11	57	4.3	44	4.1	23	2.5
H	4	P1	57	4.6	52	4.1	52	4.3
H	4	P2	42	4.3	70	7.4	83	8.2
H	4	P3	37	3.3	70	6.1	61	5.4
H	4	P4	23	4.1	41	6.6	44	6.1
H	4	P5	28	5.4	30	4.6	36	5.6
H	4	P6	52	4.9	34	2.8	35	2.8
H	4	P7	37	4.1	42	2.8	36	3.8
H	4	P8	44	4.1	44	4.3	34	3.3
H	4	P9	28	3.3	40	3.8	37	3.8
H	4	P10	40	4.3	37	3.8	31	3.1
H	4	P11	40	4.3	34	3.1	25	3.1
NH	5	P1	70	5.1	61	5.1	57	5.1
NH	5	P2	65	5.9	87	7.4	83	7.9
NH	5	P3	52	4.1	57	4.9	87	8.2
NH	5	P4	43	6.6	48	6.6	43	6.9
NH	5	P5	44	8.2	52	7.4	40	6.1
NH	5	P6	52	4.3	52	4.3	52	4.1
NH	5	P7	57	4.1	52	4.6	52	3.8
NH	5	P8	48	4.1	48	4.3	48	4.1
NH	5	P9	48	4.6	48	4.3	52	3.8
NH	5	P10	48	3.8	48	4.1	43	4.1
NH	5	P11	38	4.9	40	4.3	44	3.8
H	6	P1	38	5.6	48	5.6	48	5.9
H	6	P2	52	7.2	61	6.1	83	9.5
H	6	P3	52	5.9	65	6.9	57	5.6
H	6	P4	26	5.6	36	5.9	38	6.4
H	6	P5	30	6.9	39	7.7	41	7.2
H	6	P6	42	5.4	42	4.3	52	4.3

H	6	P7	41	6.1	57	4.3	39	4.9
H	6	P8	42	5.9	48	4.3	48	4.1
H	6	P9	44	5.9	48	4.9	48	4.6
H	6	P10	40	4.9	40	4.3	43	4.1
H	6	P11	36	4.9	52	4.3	52	4.6
NH	7	P1	48	5.6	37	4.6	40	4.3
NH	7	P2	61	9.2	57	7.2	83	10.0
NH	7	P3	48	5.6	61	5.9	65	6.9
NH	7	P4	35	9.2	33	5.6	39	6.6
NH	7	P5	31	7.7	33	6.1	33	5.1
NH	7	P6	52	7.2	48	4.6	44	4.3
NH	7	P7	52	5.4	52	4.6	48	4.6
NH	7	P8	43	6.1	41	4.9	40	4.6
NH	7	P9	52	5.6	44	4.9	41	4.9
NH	7	P10	39	6.9	40	4.3	39	4.1
NH	7	P11	52	6.6	41	4.6	37	4.1
H	8	P1	48	4.3	48	4.3	48	4.3
H	8	P2	38	4.3	83	11.5	70	7.9
H	8	P3	43	4.1	61	7.7	78	9.2
H	8	P4	22	4.9	27	5.1	27	5.1
H	8	P5	19	5.1	39	9.7	26	5.4
H	8	P6	44	4.6	48	4.3	52	4.1
H	8	P7	40	4.3	41	4.3	44	4.6
H	8	P8	38	4.6	48	4.3	48	4.3
H	8	P9	37	4.3	39	4.6	43	4.6
H	8	P10	35	4.6	44	4.3	42	4.3
H	8	P11	37	4.3	35	4.1	44	4.1
NH	9	P1	61	4.6	52	4.3	61	5.1
NH	9	P2	70	7.9	70	6.4	74	7.4
NH	9	P3	48	5.4	91	8.4	65	5.9
NH	9	P4	32	5.4	35	4.9	44	6.4
NH	9	P5	29	4.6	30	4.6	36	5.6
NH	9	P6	65	4.3	52	3.6	65	4.3
NH	9	P7	70	3.8	74	4.1	65	4.1
NH	9	P8	48	4.1	52	4.1	48	3.8
NH	9	P9	61	3.8	52	4.3	65	3.8
NH	9	P10	48	3.8	52	4.1	57	3.8
NH	9	P11	48	3.6	48	3.6	61	4.1
H	10	P1	44	5.1	44	4.6	52	4.6

H	10	P2	65	9.5	65	6.6	65	6.9
H	10	P3	52	7.4	57	6.1	70	6.4
H	10	P4	30	7.4	32	5.9	24	4.6
H	10	P5	29	8.2	34	6.6	31	5.4
H	10	P6	48	4.9	48	3.8	65	4.1
H	10	P7	32	6.1	48	3.8	52	4.1
H	10	P8	44	4.9	48	4.1	57	4.3
H	10	P9	48	4.6	48	4.1	40	4.3
H	10	P10	43	4.1	52	3.8	57	4.1
H	10	P11	52	4.6	43	4.1	52	3.8